Site U1379[1]

Expedition 334 Scientists[2]

Chapter contents

Background and objectives

Integrated Ocean Drilling Program (IODP) Site U1379 (proposed Site CRIS-4A) was drilled into the upper slope of the Costa Rica margin, 34 km offshore Osa Peninsula and 16 km from Caño Island along seismic BGR99 Line 7 (Fig. F1). Site U1379 overlies the seismogenic zone as defined by the aftershock sequence of the 2002 M 6.4 Osa earthquake (S.L. Bilek, pers. comm., 2003; I.G. Arroyo, pers. comm., 2008) in an area where the plate boundary is 4.5 km below seafloor. Geodetic measurements indicate this area to be located above the locked portion of the plate boundary (LaFemina et al., 2009). At Site U1379, the temperature at the plate boundary was interpreted to be >150°C (Grevemeyer et al., 2004). More recent modeling implies much cooler intraplate temperature with values of ~90°C (Harris et al., 2010). Site U1379 was designed as a "pilot hole" in preparation for proposed deeper Costa Rica Seismogenesis Project Program B drilling at this location.

The primary purpose of drilling Site U1379 was to determine the nature, composition, and physical properties of the upper plate basement. According to present geological and geophysical data interpretation of the Costa Rica margin, the upper plate basement provides the input material to the seismogenic zone. Interpretation of the on-land geology of Osa Peninsula suggests that the upper plate basement could be very heterogeneous in lithology and age. In fact, the outcropping unit is a mélange, the origin of which seems to be related to seamounts accreted between the early Eocene and the middle-late Miocene (Vannucchi, et al., 2006). Because of this heterogeneity Expedition 334 planned a double penetration of the forearc basement at Sites U1378 and U1379.

Tectonic erosion is the process characterizing the Costa Rica subduction zone, and documentation of the margin subsidence/uplift is a key objective to infer the volume of material removed from the upper plate and transported along the plate boundary. Our strategy was to drill the slope sequence in two locations, the middle and the upper slope, and compare results to reconstruct the stratigraphy of the sediments and to infer its variations and subsidence/uplift histories along the transect. At Site U1379, a ~890 m thick slope sediments overlie the upper plate basement as shown in the seismic lines by the prominent reflectors and increasing *P*-wave velocity (Figs. F1, F2). Because of the shallow water depth at this site, high-resolution benthic paleontology is ex-

[1] Expedition 334 Scientists, 2012. Site U1379. *In* Vannucchi, P., Ujiie, K., Stroncik, N., Malinverno, A., and the Expedition 334 Scientists, *Proc. IODP,* 334: Tokyo (Integrated Ocean Drilling Program Management International, Inc.). doi:10.2204/iodp.proc.334.104.2012
[2] Expedition 334 Scientists' addresses.

doi:10.2204/iodp.proc.334.104.2012

pected to provide an excellent record of vertical tectonism related to estimation of the thickness of the subduction channel.

Additional objectives included

- Determining the stress and strain regime of the locked portion of the margin,
- Constraining the fluid-flow regime and role of slope sediments in fluid transport, and
- Calibrating the bottom-simulating reflector–derived temperature.

Stress measurements at this site and onshore strain measurements may show stress transients in the currently locked plate boundary offshore and beneath the Osa Peninsula, respectively.

The seismic interpretation of Site U1379 is based on the prestack depth-migrated seismic BGR99 Line 7 processed by C.R. Ranero (Fig. F1). The site is located at common midpoint 750 (8°40.8496′N, 84°2.0169′W) at 125 meters below sea level (mbsl). Stratification in slope sediment is coherent, and the section is therefore likely to yield a complete sedimentation history. The seismic reflectors within the uppermost 800 m of the section show good continuity. An angular unconformity is inferred to occur at ~550 meters below seafloor (mbsf). The uppermost 550 m of the slope sediment sequence shows clear horizontal reflections. The underlying sequence shows reflectors that gently dip seaward (toward the southwest). The lowermost part of the sedimentary sequence is sharply marked by a high-amplitude reflector interpreted as the top of the upper plate basement. The bottom reflectors of the slope sediments gently dip landward and, moving northeast, abruptly terminate against the basement in correspondence with one of the high-amplitude reflectors cutting through the upper plate. This is clear evidence of normal displacement along these latter structures. The velocity increases from <2.3 m/s in sediment to >3.6 m/s in the basement. The surface of the basement top at Site U1379 is smooth and subhorizontal.

Operations

Transit to Site U1379

After a 1.25 h transit from Site U1378 covering 6 nmi and averaging 4.8 kt, speed was reduced and thrusters and hydrophones were lowered. Dynamic positioning was initiated over Site U1379 at 0345 h (Universal Time Coordinated [UTC] – 6 h) on 20 March 2011. The position reference was a combination of GPS signals and a single acoustic beacon. The positioning beacon was deployed at 1109 h on 17 March and recovered at 0940 h on 2 April.

Site U1379

Three holes were drilled or cored at this site (Table T1). The first hole was drilled with a 8½ inch drill bit with logging-while-drilling (LWD) tools in the bottom-hole assembly (BHA). The next hole was drilled with the advanced piston corer (APC) system to recover a mudline core and one additional core. The third hole was drilled with the APC coring system to refusal at 91.2 mbsf followed by extended core barrel (XCB) coring to refusal at 949.0 mbsf (1087.8 meters below rig floor [mbrf]). The advanced piston corer temperature tool (APCT-3) was deployed six times, and usable data were recovered five times. The Flexit orientation tool was deployed on all APC cores in Hole U1379C, but data were lost from the first 10 cores when a critical computer was turned off during the first tool's deployment, causing the tool to lose synchronization with the computer. All APC holes were cored with nonmagnetic core barrels. Recovery for Site U1379 was 100.3% with the APC system and 84.4% with the XCB system. Overall core recovery for Site U1379 was 85.9%. A total of 120 cores were recovered after coring 959.5 m. Total length of core recovered at this site was 824.17 m.

Hole U1379A

Rig floor operations commenced at 0345 h on 20 March 2011. The trip to the seafloor was uneventful in the very shallow water. The top drive was picked up, the drill string was spaced out, and the LWD hole was spudded at 0955 h on 20 March. After 73 h of drilling, Hole U1379A was terminated at 962.8 mbsf. After picking up off bottom, the hole was displaced with heavy drilling mud (10.5 ppg) and the drill string was tripped out of the hole to ~500 mbrf while experiencing high torque and significant overpull. The top drive was set back and the drill string was tripped the rest of the way to surface. The 6½ inch drill collars were laid out for offloading in Puntarenas, Costa Rica. Data were downloaded from the LWD tools as they were broken down at the rig floor. The LWD tools were then stored for transit and the rig floor was secured. Thrusters and hydrophones were pulled and the vessel was put into cruise mode, ending Hole U1379A at 2254 h on 23 March. The vessel transited to Puntarenas to offload the LWD tools and equipment.

Hole U1379B

After offloading the LWD tools in Puntarenas, the vessel made the 9 h transit back from Puntarenas, covering 97.2 nmi and averaging 11.8 kt. Speed was reduced and thrusters and hydrophones were lowered. Dynamic positioning was initiated over Site U1379 at 0530 h (UTC – 6 h) on 25 March. After off-

setting the vessel 20 m west of Hole U1379A, Hole U1379B was spudded at 1030 h. The mudline core established seafloor depth at 138.5 mbrf. APC coring continued until 10.5 mbsf. Two cores were taken with a total recovery of 8.72 m for an overall recovery in Hole U1379B of 83.0%. The drill string was tripped to just above the mud line, clearing the seafloor at 1030 h on 25 March, ending Hole U1379B.

Hole U1379C

After offsetting the vessel 20 m north, Hole U1379C was spudded at 1255 h on 25 March and advanced with the APC coring system to 91.2 mbsf before refusal. All cores after the second core were partial strokes and the hole was advanced by recovery. The coring system was switched to the XCB coring system and coring continued from Core 334-U1379C-18X through Core 118X. Temperature measurements were taken with the APCT-3 on Cores 4H, 7H, 10H, 12H, 13H, and 16H. Microspheres were run on Cores 20X, 30X, 40X, 50X, 60X, 75X, 92X, 105X, and 107X. A total of 17 APC cores were taken with a total recovery of 91.92 m (100.8%). A total of 101 XCB cores were taken over a 857.8 m interval, recovering 723.64 m of core (84.4%).

After reviewing the LWD penetration rates, which remained high into the basement section of Hole U1379A, and given the high recovery rates of the XCB system, a decision was made to push the XCB system into the basement section of Hole U1379C. XCB core recovery continued to be excellent until basement was reached. After Core 334-U1379C-104X, the recovery dropped off as we experienced soft to hard to soft formation changes. Average recovery after Core 103X through 118X at 949 mbsf was 19.8%. Average XCB recovery prior to Core 104X was 89.2%.

The total cored interval in Hole U1379C was 949.0 m with 815.56 m of core recovered for an APC/XCB combined recovery of 85.9%. Last core on deck for Hole U1379C was at 0130 h on 2 April. The hole was displaced with 10.5 ppg mud, and the drill string was pulled back to 565 mbrf with the top drive in place. High torque (>500 A) and overpull were observed all the way to 565 mbrf. At 565 mbrf, the top drive was set back and the remainder of the drill pipe and BHA were tripped back to the surface. The seafloor was cleared at 0755 h, and the bit cleared the rotary table at 0910 h. The rig was secured for transit and the beacon was recovered at 0941 h, ending Hole U1379C at 0945 h on 2 April.

Lithostratigraphy and petrology

Site U1379 was drilled to investigate the lithostratigraphy of the upper slope sequence and the uppermost portions of the basement imaged with multichannel seismic reflection data. A primary goal was to determine the composition of the basement material. Coring two holes from the seafloor to 949 mbsf recovered sediment and sedimentary and igneous rocks.

Hole U1379C is predominantly composed of a monotonous sequence of silty clay to clay that alternates with widely interspersed decimeter-scale sandy layers. Hardened concretions of carbonate mud are present in the interval between Cores 334-U1379C-16H and 40X (~79–305 mbsf). Shell fragments are widely dispersed throughout the monotonous clay. A sequence of 53 tephra horizons is observed below 177.75 mbsf. This predominantly clayey unit is interrupted by sand between 334 and 651 mbsf. The sand changes character in Core 71X (~622 mbsf), gradually becoming progressively coarser with increasing depth beneath the seafloor. The interval between Cores 78X and 102X is composed of fine- to medium olive-green sand with graded beds and disseminated volcanic glass shards.

The contact of the basement (as defined in the seismic profiles) with the overlying sandstone in Core 334-U1379C-103X at 881.75 mbsf is not exposed but marked by the first appearance of aphyric to phyric basalt clasts. The lithostratigraphic record of the basement cores and especially of the igneous units is incomplete because of lower recovery rates in Cores 103X through 118X. The basalt contains sparsely distributed plagioclase, pyroxene, or olivine phenocrysts. The phenocrysts are intercalated with dominantly fine-grained sandstones and mafic breccia (i.e., mainly basalt clasts). Below 906.72 mbsf until total depth of the hole at 949 mbsf, no additional igneous rocks were recovered other than mafic clasts occurring within sandstones, breccia, and conglomerates. Other clasts are composed of limestone and mudstone. The remaining part of the core is dominated by sandy and clayey silt.

Description of units

Cores recovered at Site U1379 are assigned to five lithostratigraphic units (Fig. **F3;** Table **T2**). The 881.75 m sequence above the contact with the basal unit is divided into four units on the basis of lithologic attributes. Intervals cored at Site U1379 include

0–9.5 mbsf in Hole U1379B (Cores 334-U1379B-1H through 2H) and 0–947.52 mbsf in Hole U1379C (Cores 334-U1379C-1H through 118X). Core recovery was excellent (86%). Core from Hole U1379B was collected exclusively for microbiological and geochemical analyses. Lithostratigraphic definitions for Site U1379 are based exclusively on core recovered from Hole U1379C.

Unit I

Interval: 334-U1379C-1H-1, 0–93 cm
Thickness: 0.93 m
Depth: 0–0.93 mbsf
Age: Pleistocene?–recent
Lithology: coarse sand

Unit I consists mainly of a medium- to coarse-grained buff sand with disarticulated shell fragments (Fig. F4). The sediment is loose. The unit is generally massive with few centimeter-scale bedding surfaces.

Unit II

Interval: 334-U1379C-1H-1, 93 cm, through 77X
Thickness: 650.07 m
Depth: 0.93–651 mbsf
Age: early Pleistocene
Lithology: clay(stone), silt(stone), and sand(stone)

Unit II consists mainly of olive-green clayey silt(stone) and silty clay(stone) with minor layers of sand(stone), sandy silty clay(stone), clay, clayey silt(stone), and tephra. The sediment is firm and well consolidated from 0.93 mbsf (Section 334-U1379C-1H-1) and contains tephra layers that remain unlithified to 650 mbsf (Section 70X-1). In general, Unit II is massive with minor changes in the proportions of clay, silt, and sand grain sizes occurring gradually over <1 m intervals. Few original sedimentary contacts or primary structures were observed because of bioturbation. Clayey silt(stone), sandy silt(stone), carbonate mud sediment, and light gray calcareous clasts and interbeds are more common in the following intervals:

- Cores 14H through 21X (83.8–126.14 mbsf),
- Cores 29X through 30X (198.9–218.57 mbsf),
- Core 34X (245.9–255.79), and
- Cores 37X through 40X (275.3–314.44 mbsf).

Trace abundances of framboidal pyrite were observed in many of the smear slides throughout Unit II, although locally greater abundances are common.

Subunit IIA

Subunit IIA is a clay-rich sequence that varies from dark greenish black silty clay(stone) to greenish black clayey silt(stone). None of the cored material is truly soft sediment; Cores 334-U1379C-1H through 78X are firm to very firm. This subunit is homogeneous with thick intervals of silt(stone) and clay(stone) (Fig. F5). Small burrows are the most commonly observed sedimentary structure. At the top of Subunit IIA, evidence of slumping is present.

The main components of Subunit IIA are terrigenous, dominantly clay. Smear slides indicate that the most common accessory grains in the silt(stone) and clay(stone) include feldspar and lithic (sedimentary and magmatic) fragments. Components present in trace abundances include amphibole, calcite, biotite, chlorite, glass shards, and opaque minerals. Trace abundances of pyrite framboids are widespread. Biogenic components that are sparse but ubiquitous throughout the subunit include nannofossils, diatoms, and foraminifers. Rare radiolarians and phosphatic fish remains were observed throughout the subunit. Wood or plant material is found throughout the subunit, although abundances decrease with depth below the seafloor.

Subunit IIB

The top of this subunit is placed at the first occurrence of carbonate concretions. Subunit IIB consists of a clay-rich sequence that varies from dark greenish black silty clay(stone) to greenish black clayey silt(stone) that is distinguished from Subunit IIA by the presence of carbonate (both calcareous and dolomitic) concretions, carbonate mud sediment, and reduced abundances of shell fragments (Fig. F6). Little to no bioturbation is observed in Subunit IIB. Nannofossil abundance is variable in Subunit IIB, ranging from abundant to barren. Subunit IIB has upper (84–126 mbsf) and lower (190–305 mbsf) sequences that are characterized by enriched intervals of hardened carbonate. The subunits are separated by a more monotonous sedimentation of silty clay(stone)–clay(stone) and clayey silt(stone)–sand(stone) that also contain two tephra layers at 161 and 177 mbsf.

Smear slides indicate that after the calcareous matrix, the most common accessory grains in the matrix of the carbonate mud are chert fragments, feldspar, chlorite, and volcanic glass and some rare amphiboles, pyroxenes, glauconites, and opaque minerals. Trace abundances of pyrite framboids are common throughout the subunit. Biogenic components that are sparse, but ubiquitous, throughout the subunit include nannofossils, diatoms, and foraminifers.

Subunit IIC

Subunit IIC consists of olive-green silty sand and sandstone (Fig. F7). The sands are fining- and coarsening-upward decimeter-scale sequences. Three in-

tervals with accumulated tephra layers are observed in this subunit. Bioturbation is variable throughout Subunit IIC but generally decreases with depth. Framboidal pyrite was observed in trace abundances in many smear slides throughout Subunit IIC, although locally greater abundances are common. Small disseminated woody debris and plant detritus is recognized within the subunit. Nannofossil abundances in Subunit IIC are variable, ranging from barren to rare. Subunit IIC is interspersed throughout Unit II in the following intervals:

- Cores 334-U1379C-44X through 47X,
- Cores 49X through 51X,
- Cores 55X through 60X,
- Cores 68X through 70X, and
- Cores 73X through 74X.

The main components in the sandstone of Subunit IIC are lithic (sediment > magmatic) clasts and feldspar crystals. Smear slides suggest that the abundance of magmatic grains increases toward the base of Subunit IIC, whereas the abundance of lithic fragments decreases with depth. The accessory grains in the sandstone vary as a function of depth; chlorite decreases with depth, whereas amphibole increases with depth. Interestingly, the abundance of volcanic glass is greatest in the middle of Subunit IIC. Additionally, calcite, biotite, pyroxene, and opaque minerals are present without any significant change throughout the subunit. Biogenic components are rare but include nannofossils, diatoms, and foraminifers.

Unit III

Interval: 334-U1379C-78X-1 through 102X
Thickness: 228.9 m
Depth: 651–880.07 mbsf
Age: early Pleistocene
Lithology: fine to medium sandstone

Unit III consists mainly of olive-green silty sands and sandstone and shows fining- and coarsening-upward decimeter-scale sequences of sand with erosive bases (Fig. **F8**). Three phases of predominantly sandy deposits alternate with finer hemipelagic sediments and accumulate to a total thickness of 146 m. The coarse sandy deposits are 64% of the total unit thickness. The three sandy intervals are between

- 651 and 660.69 mbsf (interval 334-U1379C-78X-1, 93 cm, through Section 78X-CC),
- 699 and 766 mbsf (interval 83X-1, 15 cm, through 91X-1, 2 cm), and
- 804 and 880 mbsf (interval 95X-1, 31 cm, through Section 102X-CC).

Larger (millimeter scale), well-rounded to subrounded sedimentary lithic clasts and shell fragments compose the coarser portions of the sandstones. Rip-up clasts, millimeter-scale laminations, convolute bedding, and chaotic mixing is observed throughout the coarser sequences but is restricted to the partly eroded basal parts of the fining-upward sequences.

Tephra layers are less common in Unit III and are concentrated in one interval within the upper part of the unit. Bioturbation is variable throughout the unit but generally decreases with depth. Framboidal pyrite in trace abundance was observed in many smear slides, although locally greater abundances are common. Small, disseminated wood and plant debris are recognized throughout coarser horizons in Unit III.

Smear slides indicate that the sandstones are dominated by lithic clasts that are primarily composed of magmatic rock fragments and feldspar minerals, indicating that the main components of Unit III are terrigenous. Chlorite is the most abundant accessory mineral and is followed, in order of abundance, by volcanic glass, opaque minerals, and amphibole. Trace abundances of calcite, pyroxene, quartz, and opaque minerals are present. Biogenic components are rare but include nannofossils and foraminifers.

Unit IV

Interval: 334-U1379C-102X through 103X
Thickness: 1.85 m
Depth: 879.90–881.75 mbsf
Age: late? Pliocene
Lithology: carbonate-cemented shell-bearing sand

Unit IV consists of carbonate-cemented medium- to coarse-grained sand with well-rounded, lithic pebble-sized clasts and thick-walled shell shards. Interbeds of centimeter-thick shell layers and localized well-rounded pebble conglomerate are present in the basal meter of the unit (Fig. **F9**).

Unit V

Interval: 334-U1379C-103X through 118X (end of hole)
Thickness: 67.25 m
Depth: 881.75–947.52 mbsf (total depth)
Age: late Pliocene
Lithology: poorly sorted matrix-supported breccia

Unit V is composed of matrix-supported breccia with clasts of limestone, basalt, and mudstone in a fine sandy matrix intercalated with basalt in the upper part (881.75–906.72 mbsf; Fig. **F10**) and a sequence of variably sandy and clayey silt matrix in the lower portion (916.40–947.52 mbsf). After shipboard anal-

ysis, the nature of Unit V remains enigmatic. Competing hypotheses suggest that this material is either a weathered veneer overlying pristine backstop material or material similar to the subaerially exposed Osa mélange that is younger and less deformed.

Basalt

The basalt in Unit V ranges from aphyric to moderately phyric composition containing plagioclase, pyroxene, and olivine phenocrysts (Fig. F11). These phenocrysts are euhedral to subhedral and ≤5 mm. The groundmass of the basalt is fine grained and varies from light to dark gray. Mineral compositions are summarized in thin sections in "Core descriptions." Plagioclase and pyroxene-phyric basalts are overprinted by a crosscutting vein network. The veins are preferentially straight with some irregularities. Offsets along the vein boundaries indicate that they were emplaced along faults (shear veins). Some of the veins do not show any displacement parallel to the vein boundaries, indicating that some of them were emplaced in Mode I fractures. In the recovered core fragments, subvertical green veins of unknown mineralogy represent the oldest generation, followed by subhorizontal white veins and subvertical white veins.

Some alteration is evident within the basalts, although this alteration is localized to the margins of the veins, open fractures, surfaces of single rock pieces, and phenocrysts. Along the margins of the green veins, host rock alteration is recognized as narrow (0.5 mm) margins of dark green mantles extending into the basalt. Along the subhorizontal and subvertical white veins, the surrounding groundmass is partly altered to light green. Alterations adjacent to the open fractures are characterized by a brownish green color.

Tephra layers

Cores collected in Hole U1379C contain 53 tephra layers intercalated with background sediment of the different units. Individual tephra layers range from 2 to 45 cm thick. Only two tephra layers are recognized in the uppermost 324 m of sediment, at 161 and 176 mbsf. Both are intercalated in the carbonate mud–rich Subunit IIB within the phase dominated by fine background sedimentation.

In the subjacent Subunit IIC, an upper sequence of 19 tephra layers is recognized within the uppermost 60 m of sediment (309–381 mbsf; Sections 334-U1379C-42X-3 to 48X-2). The upper tephra sequence is separated from second tephra-rich sequence by a 70 m sequence devoid of tephra. The second tephra-rich sequence that is composed of 10 tephra layers extends from 448 to 500 mbsf (Section 58X-3 to 60X-7). A third, 85 m thick tephra-rich sequence consisting of 14 discrete tephra horizons extends from 562 to 647 mbsf (Section 67X-4 to 70X-6). Between 647 mbsf and the next following sequence of more frequent tephra layers at 751 mbsf, two tephra layers at 682 and 683 mbsf (Sections 81X-2 and 81X-3) are recognized. A fourth interval of five tephra layers occurs between 751 and 773 mbsf (Sections 89X-1 and 91X-CC). The lowermost tephra layer was recognized at 875 mbsf (Section 102X-5). In general, tephra is most common in Unit II, more specifically within Subunit IIB, and is less abundant within Unit III.

The composition of the 53 identified tephra layers is variable. Twenty three are light gray to pinkish/brownish white felsic ash, 19 are pinkish gray/brown layers, and 11 are pinkish/greenish black layers. Dark black tephra beds account for ~20% of the tephra bed assemblage in Hole U1379C. Tephra layers are generally soft, but the tephra layers in Core 334-U1379C-60X are indurated and are consequently classified as tuff. Unconformable and/or inclined bedding of tephra beds is rare in the uppermost units (0–651 mbsf). Inclined tephra horizons are first recognized in lithostratigraphic Unit III. In some cores, bioturbation occurred at the top of the tephra layers. In general, tephra layers have a sharp basal contact to underlying terrigenous sediment but a gradual transition contact with overlying ash-bearing pelagic sediment and many are normally graded in grain size and well sorted (Fig. F12). The felsic white ash is mainly (>90 vol%) composed of clear, colorless glass shards varying from angular blocky, cuspate, flat, and Y-shaped shards with nearly no bubbles to highly vesicular pumiceous textures with many elongated bubbles.

The transparent glass shards of the felsic tephras have no visible signs of alteration until 500 mbsf (Core 334-U1379C-60X). Below this depth, devitrification structures increase with depth within the glass shards, reflecting differing levels of alteration. Grain size ranges from very fine to coarse ash (up to millimeter size). The mineral assemblages consist of plagioclase, pyroxene, hornblende, and biotite. Although plagioclase is the dominant phenocryst phase in this core, some of the individual tephras are dominated by amphibole and biotite. An increase in the abundance of amphibole and biotite phenocrysts is commonly interpreted to reflecting increasingly evolved felsic magma. Dark gray mafic ash layers consist predominantly of dark to light brown glass shards. Most of the glass shards have blocky shapes

and are medium to poorly vesicular and show strong signs of alteration, especially with increasing depth within the hole. The mineral assemblages of the mafic tephras include plagioclase, pyroxene, and spinel. In contrast to felsic tephras, mafic tephras contain more crystals.

Carbonate fragments and concretions

Hard fragments of limestone and dolomitic limestone were recovered beginning at ~84 mbsf (Core 334-U1379C-14H) and continue intermittently to 748 mbsf. Because most of these fragments were found in the rubble at the tops of cores, their stratigraphic position is uncertain. Most of the in situ calcareous concretions are concentrated within Subunit IIB. Intact limestone concretions and calcareous claystone/mudclasts were observed embedded in clayey siltstone in some cores. Most of the calcareous rocks consist of micrite plus nannofossils. Many contain benthic foraminifers and sand or silt grains (e.g., quartz and feldspar). Dolomite is more abundant than calcite with increasing depth. Calcareous clasts are present within the brecciated horizons of Unit IV.

X-ray diffraction analysis

Preliminary X-ray diffraction analysis of the sediment suggests that there is little variation in composition among lithostratigraphic Units I–IV. X-ray diffractograms indicate that the major mineral components are clay minerals including illite, smectite, kaolinite, and attapulgite, as well as primary minerals including calcite, anorthite, and quartz. Amphibole (hornblende and richterite), chlorite, pyroxene (augite and hypersthene), olivine, and pyrite peaks are also recognized. (Fig. **F13A**).

Mineral composition variability is greatest in sandy sediments that were collected from Unit I and the uppermost section of Unit II, where shell fragments are more common. Samples from these intervals produce spectra dominated by calcite, Mg-rich calcite, and aragonite (Fig. **F13B**).

Depositional environment

The cover sequence recovered from Hole U1379C is a terrestrially sourced shelf and upper slope sequence that is consistent with high sediment accumulation rates and increasing water depth through the depositional interval (see also **"Paleontology and biostratigraphy"**). The basal portions of the sequence are consistent with an interval of erosion separating well-indurated sands from calcareous cemented breccia. Clast compositions in the breccia include limestone, basalt, and sandstone. This sequence is capped by a <1 m thick accumulation of medium- to coarse-grained well-rounded Holocene sand.

Paleontology and biostratigraphy

At Site U1379, Pleistocene calcareous nannofossils and foraminifers were observed in the thick sediments deposited on the upper slope/continental shelf of Costa Rica. Calcareous nannofossils provide excellent biostratigraphic control for most of the investigated section (Fig. **F14**). The deepest drilled basal core was tentatively estimated to be lowermost Pleistocene. Thus, the sediments throughout the core would be younger than 1.8 Ma. Based on the nannofossil record, the estimated average sedimentation rates are ~1035 m/m.y. for the uppermost ~566 m of the drilled sedimentary section and ~160 m/m.y. between ~566 and ~722 mbsf of the section. An accumulation rate for the lowermost part of the drilled sedimentary section could not be estimated because of missing zones (Fig. **F15**). Although, the boundaries of planktonic foraminiferal zones were not recognized because of the limited numbers of samples examined, a few datum events based on the present index species are consistent with the nannofossil zonation. Benthic foraminifers provide significant insights to paleobathymetric changes on the Costa Rica subduction margin. The faunal changes reflect continuous, alternating environmental changes from continental shelf to upper slope (middle bathyal, 500–1000 mbsl).

Calcareous nannofossils

A particularly thick Pleistocene section is observed in the calcareous nannofossil record recovered from Site U1379. Presence, relative abundance, and preservation of nannofossils are documented in Table **T3.** Sample abundances range from barren to abundant and, in general, show poor to moderate preservation. For the most part, the assemblage abundances were sufficient to delineate biozonal boundaries. However, in several intervals the recognition of key marker species has been restricted because of poor preservation caused by dissolution and dilution of the nannofossil signal caused by a large amount of terrigenous sediments. In this context, the boundaries established during the shipboard examination are tentative.

Samples 334-U1379C-1H-CC through 56X-CC (6.68–466.37 mbsf) are assigned to the undifferentiated *Emiliania huxleyi–Gephryocapsa oceania* Zone NN21-NN20 of the lower to middle Pleistocene. Dominant species include *Helicosphaera carterii, G. oceanica, Gephryocapsa caribbeanica, Gephryocapsa* small, and *Calcidiscus leptoporus*.

Sample 334-U1379C-57X-CC (476.20 mbsf) is very tentatively assigned as the top of the lower Pleisto-

cene Zone NN19 based on the presence of *Pseudoemiliania lacunosa* and the absence of *Discoaster brouweri*. This consideration is due to the rare representation of *Pseudoemiliania lacunosa* in the nannofossil record at this site. Two additional biostratigraphic events that support this zonal assignment include the appearances of *H. sellii* in Sample 334-U1379C-73X-CC (622.28 mbsf) and *Calcidiscus macintyrei* in Sample 80X-CC. (679.99 mbsf). Samples 57X-CC through 85X-CC (476.20–722.48 mbsf) are tentatively assigned to the *P. lacunosa* Zone NN19 of the lower Pleistocene.

The presence of *D. brouweri,* which establishes the base of Zone NN19 and the top of Zone NN18, is not detected in the sample record. Based on the stratigraphic position, this event probably occurs in the interval between Samples 334-U1379C-86X-CC and 105X-CC (735.99–889.57 mbsf). The sediment in this sequence is either barren or shows low nannofossil abundances and contains no biostratigraphic zonal markers. Therefore, the placement of the Pleistocene/Pliocene boundary is undetermined.

The section between Sample 334-U1379C-106X-CC and Sample 118X-CC (907.14–947.25 mbsf), which contains the zonal marker *Discoaster pentaradiatus,* is assigned to the upper Pliocene Zone NN17 (Berggren 1995a, 1995b).

Foraminifers

The Pleistocene sediments cored at Site U1379 were deposited in shallow-water shelf environments (shallower than 200 mbsl). Hence, diverse benthic foraminifers abundantly occur, especially in the uppermost part of the drilled sedimentary section, and are well preserved. Conversely, the number of planktonic foraminifers is less than that of benthic foraminifers, as shown by a general trend in modern shallow-marine sediments (Ingle et al., 1980).

Planktonic foraminifers

Because of the time-consuming work required for a foraminiferal study, planktonic foraminifers were analyzed in limited horizons of 18 core catcher samples (Table **T4**). Planktonic foraminifers are common or rare in the uppermost part of Hole U1379C. The sediment investigated from Hole U1379C is mainly dominated by tropical fauna such as *Globigerinoides quadrilobatus* (*Globigerinoides sacculifer*), *Globigerinoides ruber, Orbulina universa, Globorotalia menardii, Globorotalia tumida,* and *Neogloboquadrina dutertrei*. However, because of the scarcity or absence of many of the species commonly used as makers for planktonic foraminiferal biostratigraphy, the zone boundaries of Wade et al. (2011) could not be established (Fig. **F14**). Only three index marker species of planktonic foraminifers were identified in limited horizons. Sample 334-U1379C-16H-CC (90.17 mbsf) contains *Globorotalia truncatulinoides* (first appearance at 1.93 Ma) and is assigned to foraminiferal Zone PT1. Coiling change of *Pulleniatina* from sinistral to dextral was observed in Samples 334-U1379C-53X-CC through 64X-CC (436.08–537.13 mbsf). Thus, this horizon would be older than 0.8 Ma. Sample 80X-CC (679.94 mbsf) contains *Globigerinoides extremus* and would be assigned to be older than 1.93 Ma, the last appearance age. Planktonic foraminiferal abundances are very rare to barren in the interval from Sample 90X-CC to 103X-CC (757.43–882.3 mbsf). Thus, the foraminiferal zones in the lower part of the hole are unclear. The preservation in basement Sample 112X-CC (937.16 mbsf) is poor.

Benthic foraminifers

Benthic foraminifers were analyzed in limited horizons of 16 core catcher samples (Table **T5**). Benthic foraminifers abundantly occur in the uppermost part of Hole U1379C, whereas their abundances in the lower parts decrease to common or rare. In general, many of the species of benthic foraminifers observed in the sediments of Hole U1379C are similar to modern assemblages, being characteristic of the oxygen minimum zone of the seafloor (100–800 mbsf) in this region.

Sample 334-U1379C-1H-CC (6.63 mbsf) contains *Bulimina marginata, Uvigerina peregrina,* small *Cassidulina* spp., and *Pseudoparrella* spp., indicating an outer continental shelf paleobathymetry. Samples 3H-CC to 68X-CC (24.45–575.36 mbsf) contain *Bolivina interjuncta bicostata* and *Bolivina acuminata,* indicating an outer continental shelf to upper bathyal paleobathymetry. Samples 16H-CC and 20X-CC (90.17 and 117.11 mbsf) contain a few shallow-water specimens of euryhaline or inner shelf fauna such as *Ammonia beccarii* and *Buliminella elegantissima*. Exceptionally, Sample 10H-CC (63.5 mbsf) contains some abundant species such as *Elphidium crispum,* indicative of a beach environment, and thus reflects reworked sediments from coastal shallow-marine or temporal shallowing paleobathymetry.

Samples 334-U1379C-58X-CC to 90X-CC (482.33–757.43 mbsf) contain rare deepwater species such as *Oridorsalis* and *Gyroidina,* which do not occur at depths shallower than 400 mbsf. In addition, Samples 80X-CC and 90X-CC include *Bolivina argentea,* which is found in modern slope sediments from 400 to 900 mbsf. Thus, the paleobathymetry of these horizons is estimated to be the deepest depths of upper bathyal or middle bathyal in the Pleistocene. In Samples 69X-CC and 70X-CC, foraminifers are very rare.

Half the specimens observed in Sample 90X-CC (757.43 mbsf) are brown, indicating diagenetic overgrowth with carbonate.

Sample 334-U1379C-103X-CC (882.3 mbsf), just above the basement, contains a few shallow-marine species such as *Cibicides reflugens,* indicative of a beach environment. Basement Sample 112X-CC (937.16 mbsf) includes *Cassidulina limbata* and *Planulina ornata*. Although the most dominant species are different from the other samples, the benthic foraminiferal fauna in this sample is composed of several species similar to those in the other horizons. Paleobathymetry of this sample is tentatively estimated to be upper or middle bathyal.

Structural geology

The main structural geology objectives during Expedition 334 were to describe and document style, geometry, and kinematics of structural features observed in the cores. Overall, structural data show significant changes below ~600 mbsf (i.e., increase in bedding dip, increase in fault population density, and development of highly fractured and brecciated zones) (Fig. F16). This transition corresponds broadly to the base of lithostratigraphic Unit II (see **"Lithostratigraphy and petrology"**). In Unit II, structures are dominated by gently dipping bedding (<20°) and normal faults. In Unit III, bedding dips and fault density increase. We identified four fault zones at 642.1–652.8, 766.2–777.5, 804.1–804.7, and 871.8–879.5 mbsf.

Structures in slope sediments

Bedding

Bedding planes were recognized as boundary surfaces of thin layers in lithologies such as sand and ash, as boundaries of compositional or grain size difference, and also as thin lamination boundaries.

Structural data from the sedimentary sequence of Hole U1379C indicate increasing bedding dips below 600 mbsf (Fig. F16). In the uppermost part of the section (0 to ~200 mbsf), bedding dips gently (mostly <20°). In the lowermost part of the sedimentary sequence, from 600 mbsf to the top of the basement, bedding dips are 0°–60°. This change in bedding dip across 600 m corresponds to an angular change and discontinuity of reflectors in the seismic profile (BGR99 Line 7).

Only 14 of the 313 measurements of bedding plane attitudes can be restored to the geologic coordinate because of the difficulties of paleomagnetic measurement, mainly because of biscuiting. The corrected data show that the bedding planes mostly strike northwest–southeast (Fig. F17), parallel to the strike of the Costa Rica subduction margin.

Brittle faults

Faults recognized in the Hole U1379C cores are characterized by striated and/or polished surfaces or by offset markers. The sense of slip is determined by offsets of markers such as lamination, bioturbation, and slickensteps on striated slip surfaces. Faults commonly show a normal sense of displacement (Figs. F16, F18, F19), although some faults show a reverse sense of shear. The first faults were recognized between 300 and 350 mbsf, and the first larger population occurs between 500 and 550 mbsf. Between 600 mbsf and the top of the basement at 881.8 mbsf, the density of faults is generally high. Intensively deformed intervals were classified as fault zones, and four fault zones are identified at this site (shaded bands in Fig. F16; see detailed description in **"Fractured and brecciated zones"**). Fault dips measured on discrete faults span a much wider range below 600 mbsf. This change nearly corresponds to the lithological transition from clay-dominated lithostratigraphic Unit II to the fine to medium sandstone of lithostratigraphic Unit III.

Eleven normal faults were rotated to the geographic reference frame using paleomagnetic data (Fig. F19). Although the number of corrected samples is small, two populations of normal faults are apparent. The majority trend east–west and dip to the north or south, whereas other faults dip west, striking primarily north–south. The kinematics for populations of these normal faults indicates north-northeast, south-southwest extension that is nearly parallel to the subduction vector of the Cocos plate (DeMets, 2001).

Healed faults and sediment-filled veins

Healed normal faults, which are less than a few millimeters thick and show fault cohesiveness on visual observation, can be found within cores from lithostratigraphic Units II and III. The cohesiveness of the fault plane may represent early stage, soft-sediment deformation. Examples of such faults are shown in Figure F20. The dip angle is gentle (20°–30°) for the healed normal fault recognized at 470 mbsf. The texture is characterized by an array of parallel faults, and total offsets are ~10 mm.

Sediment-filled veins aligned in arrays parallel or subparallel to the bedding plane were identified at 632–633 mbsf, just above the first fault zone (642.1–652.8 mbsf). Sediment-filled veins are frequently reported from accretionary complexes, slope basins, and forearc sediments in subduction margins (e.g., Hanamura and Ogawa, 1993; Brothers et al., 1996; Grimm and Orange, 1997).

Fractured and brecciated zones

Fractured zones are defined as moderately sheared zones fractured into a few centimeter-sized fragments. Brecciated zones represent intensively sheared zones composed of angular clasts, predominantly millimeter to 1 cm sized fragments (Fig. F21). Each fragment is angular in shape with slickenlines on its surfaces indicating a systematic direction. For the most part, these features are distinguishable from drilling-induced fractures and clasts (see "Structural geology" in the "Methods" chapter [Expedition 334 Scientists, 2012]).

The four fault zones shown in Figure F16 are characterized by alternating sequences of fractured and brecciated zones, always terminated by a weakly fractured zone in the largely undisturbed host rock below. When the interval between the last and next occurrence of fractured/brecciated zones is >20 m, they are defined as two distinct fault zones. Based on this definition, four fault zones have been identified in the lower part of sedimentary sequences at 642.1–652.8, 766.2–777.5, 804.1–804.7, and 871.8–879.5 mbsf. Slip direction and shear sense have been recorded in the fractured zone and indicate a nearly dip-slip–normal fault sense. The thickest fault zone (642.1–652.8 mbsf) is 11 m above the lithologic transition from lithostratigraphic Unit II to III and consists of an 0.8 m thick brecciated zone in the center with an average clast size of 5–10 mm and fractured zones above and below. The fault zone at 766.2–777.5 mbsf is characterized by several extensively fractured intervals and >20 normal faults. The deepest fault zone is defined by a number of normal faults between 871.8 and 879.5 mbsf (Fig. F16).

All the fault zones were developed in the silty clay interval, whereas sand layers just below the fault zone are coherent or contain considerably weaker deformation, implying a lithologic control on fault zone development. The uppermost occurrence of the fault zone corresponds to the lowermost part of lithostratigraphic Unit II (Fig. F16), just above Unit III, which is composed of fine to medium sandstone. The lowermost fault zone was identified just above the basement, corresponding to the base of Unit III.

Structures in the basement

The contact between the slope sediments and the basement is at 881.8 mbsf in Hole U1379C. Bedding planes in the basement dip gently, with angles typically <20°. Soft-sediment deformation, such as convolute lamination, was identified. No pressure-solution cleavage or slaty cleavages were observed in the basement. Mineral-filled veins developed only in the limestones and basalts. The basalts contain multiple generations of quartz and chlorite veins (see "Lithostratigraphy and petrology").

Geochemistry and microbiology

Geochemistry

We collected 110 whole-round samples for pore fluid analysis. In Hole U1379B, we collected two samples per section. In Hole U1379C, the sample frequency was two samples per core in the uppermost 235 mbsf followed by one sample per core for the rest of the hole. Samples from the uppermost interval (Cores 334-U1379B-1H through 2H [0–7.98 mbsf] and Cores 334-U1379C-1H through 6H [0–39.38 mbsf]) were processed under a nitrogen atmosphere to preserve the reduced dissolved species and their isotopic composition (Fe and Mo), which will be analyzed postcruise. The remaining samples were exposed to the atmosphere prior to squeezing. For the organic geochemistry program, we collected 118 sediment plugs (HS) for safety monitoring of headspace hydrocarbon gases and analyzed them by gas chromatography–flame ionization detection (GC-FID) on the natural gas analyzer. In addition, 74 void gas samples (VAC) were collected from voids, whenever present. Most of these samples were analyzed by GC-FID (102 samples), and a replicate sample was preserved for isotope analyses at onshore laboratories. The inorganic and organic geochemistry data are listed in Tables T6, T7, and T8 and are plotted in Figures F22, F23, F24, F25, and F26. Microbiology data (cell counts) are shown in Figures F27 and F28.

The pore fluid profiles of sulfate, alkalinity, ammonium, and calcium in the uppermost 50 mbsf reflect typical changes associated with organic carbon cycling. Alkalinity and ammonium increase from seawater values to maxima at 12 mbsf, reflecting organic matter diagenesis. At ~14 mbsf, the sulfate gradient decreases associated with a concomitant decrease in NH_4 concentrations and a decrease in the alkalinity gradient. Based on the sulfate data, the depth of the sulfate–methane transition zone (SMTZ) is estimated to be ~30 mbsf (Fig. F22). This zone is characterized by a decrease in dissolved calcium to values as low as 2.5 mM, suggesting authigenic carbonate precipitation between 20 and 30 mbsf. Below the SMTZ, methane concentrations increase with depth (Fig. F22) and reach the highest concentrations from 42.31 to 67.18 mbsf (Fig. F25). Methane at these depths is dominated by microbial production, as indicated by the high ratio of methane to heavier homologs (ethane and propane), with $CH_4/(C_2H_6 + C_3H_8)$ ratios ranging from 8,000 to 10,000 (Fig. F26).

Based on the limited shipboard data set collected at Site U1379, the pore fluid geochemistry below the zone of most intense biogeochemical cycling in the uppermost 50 m can be split into three zones. The first zone extends from ~50 to 500 mbsf and is characterized by a steady increase in Ca concentration and a decrease in Mg and K concentrations with depth. Within this zone there are two maxima in NH_4 concentration of ~10 mM at 158 and 386 mbsf (Fig. F23). There are small maxima in potassium and alkalinity associated with the NH_4 peak at 386 mbsf. The high NH_4 concentrations observed in the uppermost 400 m of the sediment column, generally between 3 and 10 mM, is likely the result of the high sedimentation rates at this site (see **"Lithostratigraphy and petrology"** and **"Paleontology and biostratigraphy"**) causing the ammonium produced by organic matter diagenesis to remain buried in the section. Within this zone, ethane concentrations increase progressively below ~100 mbsf, whereas propane to pentane are only detected in insignificant amounts to ~360 mbsf (Fig. F25). Two discrete peaks in C_2 to C_5 gas concentrations are observed at ~360 and 440 mbsf, which roughly correlate with an increase in NH_4 concentration observed in pore fluids. The profiles of C_2 to C_5 indicate the presence of thermogenic gases at and below 360 mbsf.

The second geochemical zone occurs between ~500 and 800 mbsf and is characterized by a broad interval of low Cl, Ca, Mg, NH_4, and alkalinity concentrations, with the lowest concentrations occurring at ~680 mbsf (Fig. F23). The K concentration-depth profile, however, steadily decreases in this interval, similar to the gradient observed in the uppermost 500 m of the sediment section. The lowest $CH_4/(C_2H_6 + C_3H_8)$ ratios observed at this site (137–327) occur in the zone between 598.49 and 656.55 mbsf, with methane concentration ranging between ~3000 and 6000 ppmv (Fig. F25). A strong peak in C_2 to C_5 concentrations occurs at ~650 mbsf and is coincident with the minima in Cl concentration observed in the pore fluids. The broad decrease in the major elements and decrease in the ratio of methane to the heavier hydrocarbons correlates with lithostratigraphic Unit III, which is dominated by coarser grained sediments as well as several fault zones identified below ~600 mbsf (see **"Structural geology"**). Collectively, the inorganic and organic geochemical data suggest lateral flow of a freshened fluid with elevated concentrations of thermogenic hydrocarbons (up to *iso*-pentanes) and potassium. The geothermal gradient at Site U1379 is 40°C/km (see **"Physical properties"**); thus, the temperature between 600 and 800 mbsf ranges from 24° to 32°C. This temperature range is too low for in situ production of thermogenic hydrocarbons or for extensive clay dehydration, suggesting the fluid sampled in Unit III originated from a deeper source and is migrating laterally and upward along the permeable sand horizons and faults. This inference will be confirmed by isotopic analyses of the pore fluids postcruise.

The third geochemical zone occurs from ~800 to ~900 mbsf and is characterized by a strong linear increase in Ca concentrations and a decrease in Mg concentrations (Fig. F23). Within this interval calcium concentrations increase from 14 to 35 mM (~3 times seawater value) and Mg concentrations decrease from 22 to 10 mM (~20% of seawater value). This zone extends from the base of lithostratigraphic Unit III to basement (Unit IV; see **"Lithostratigraphy and petrology"**). The Ca and Mg trends (Fig. F24) suggest that the deepest sampled fluid is distinct from that of Unit III and is dominated by fluid-rock reaction with basalt in the basement mélange. Within this interval, CH_4 concentrations reach 9630 ppmv and the $CH_4/(C_2H_6 + C_3H_8)$ ratio increases to 834. With the limited shipboard data set, it is difficult to determine whether the fluids in the sampled basement section have migrated from depth or simply reflect in situ diagenesis. The source of the deepest sampled fluids will be constrained by shore-based chemical and isotopic analyses.

Microbiology

Microbiological sampling consisted of 5 cm whole-round samples cut on the catwalk and subsampled in the laboratory using sterile techniques. In Hole U1379B, whole-round samples were taken at a frequency of one per meter of core. In Hole U1379C, whole-round samples were taken at a frequency of two per core during APC coring and once per 10–15 cores during XCB coring. The deepest sample was taken from Core 334-U1379C-92X at ~770 mbsf. Subsampling of the whole-round samples was performed for three different categories of postcruise studies: (1) frozen samples for molecular analyses, (2) refrigerated samples for cultivation studies, and (3) paraformaldehyde-fixed samples for cell counting and contamination testing.

Fixed samples for cell counting were further prepared on board with a SYBR Green I staining procedure, and enumeration estimates performed for samples from 0.7 to 211 mbsf revealed cell concentrations ranging from 10^6 to 10^8 cells/cm^3, generally declining with depth. (Fig. F27). Closer inspection of the uppermost 45 mbsf shows a localized trend of increasing cell concentrations from 15 to 33 mbsf, near the proposed SMTZ, before decreasing again (Fig. F28). Contamination was assessed qualitatively in XCB cores using fluorescent microspheres. Microscopic analysis of the fluorescent microspheres

revealed at least some drill fluid contamination of XCB-cored sediment into the centre of the core. Hence, cell enumeration estimates became increasingly unreliable with great depth, and those beyond 200 mbsf were not included in this analysis.

Physical properties

At Site U1379, physical properties measurements were made to provide basic information characterizing lithostratigraphic units. After sediment cores reached thermal equilibrium with ambient temperature at ~20°C, gamma ray attenuation (GRA) density, magnetic susceptibility, and *P*-wave velocity were measured on whole-round core sections using the Whole-Round Multisensor Logger (WRMSL). For basement cores, only GRA density and magnetic susceptibility were measured. After WRMSL scanning, the whole-round sections were logged for natural gamma radiation (NGR). Thermal conductivity was measured using the full-space method on sediment cores and the half-space method on split lithified sediment and basement cores. A photo-image capture logger and a color spectrophotometer were used to collect images of the split surfaces of the archive-half cores on the Section Half Imaging Logger and Section Half Multisensor Logger (SHMSL), respectively. Discrete *P*-wave measurements were made on split sediment cores and on cubes subsampled from lithified sediment and basement working-half cores on the Section Half Measurement Gantry (SHMG). Moisture and density (MAD) were measured on discrete subsamples collected from the working halves of the split cores.

Density and porosity

Bulk density values at Site U1379 were determined from both GRA measurements on whole cores and mass/volume measurements on discrete samples from the working halves of split cores (see **"Physical properties"** in the "Methods" chapter [Expedition 334 Scientists, 2012]). Samples were chosen from relatively undisturbed portions and preferentially from clay sediments rather than silty or sandier sections. A total of 530 discrete samples were analyzed for MAD.

In general, wet bulk density values determined from whole-round GRA measurements agree with measurements from discrete samples (Fig. **F29A**). Wet bulk density values increase with depth. This increase is likely due to dewatering caused by overburden pressure and is well described by a linear trend between 100 and ~880 mbsf. Lack of good core recovery deeper than 880 mbsf made GRA measurements difficult. Bulk density values in the brecciated basement have a density of ~2.3 g/cm^3.

Grain density measurements were determined from mass/volume measurements on discrete samples. Values are relatively constant with depth to ~430 mbsf, with an average value of 2.67 g/cm^3 and generally ranging between 2.6 and 2.8 g/cm^3 (Fig. **F29B**). Below 430 mbsf, data are more scattered, with maximum values >2.75 g/cm^3 reflecting a change in the nature of grains. At the bottom of the sedimentary section and just above the basement, the scatter is significantly reduced, possibly indicating a more homogeneous formation, and grain density is 2.75 g/cm^3. On the whole, these values suggest terrigenous composition.

Porosity values (see **"Physical properties"** in the "Methods" chapter [Expedition 334 Scientists, 2012]) were determined from mass/volume measurements on discrete samples using MAD Method C on sediment cores and Method D on basement cores. Within the sedimentary section, porosity is inversely correlated with bulk density. In the slope sediments, porosity decreases linearly from ~62% to 40%, with several intervals showing higher values. Porosity within the brecciated basement is ~30% (Fig. **F29C**).

Magnetic susceptibility

Volumetric magnetic susceptibilities were measured using the WRMSL and point measurements were made on the SHMSL for all recovered cores at Site U1379. Uncorrected values of magnetic susceptibility are presented in Figure **F30.** Magnetic susceptibility values measured by these two methods are in good agreement. Overall, magnetic susceptibility in the sedimentary sequence is low, indicating an abundance of non-iron-bearing clays. Magnetic susceptibility in the uppermost 100 mbsf is variable, with values to ~0.8 SI. With the exception of some notable excursions, magnetic susceptibility values between ~100 and 880 mbsf are relatively low and more uniform. Conspicuous excursions occur between ~100 and 200 mbsf. These excursions exhibit high wave number variability and may be due to lithologic variations between silt and clay. In the 470–520 and 800–840 mbsf intervals, high magnetic susceptibility values correspond to sand and tephra layers.

Magnetic susceptibility values in the basement are generally greater than those in the slope sediments. The apparent variability is an artifact of incomplete recovery.

Natural gamma radiation

NGR results are reported in counts per second (cps; Fig. **F31**). NGR counting intervals were ~10 min per whole-core interval. Despite the short counting time, NGR counts are considered reliable.

NGR values in the sediment section are between 15 and 35 cps and show high wave-number variability, likely due to edge effects that have not been filtered. The highest values are at ~280 mbsf. From ~630 mbsf to the top of basement, the downhole decrease of NGR is consistent with a downhole increase of both sandy sediments (see **"Lithostratigraphy and petrology"**) and grain density (Fig. **F29**). NGR values in basement are generally low, which is consistent with sandy lithologies described in this interval (Fig. **F31**).

P-wave velocity

Unconfined measurements of *P*-wave velocity at Site U1379 were determined from measurements on sediment whole cores and on discrete samples from the working halves of sediment and basement split cores (see **"Physical properties"** in the "Methods" chapter [Expedition 334 Scientists, 2012]). In general, whole-core measurements yielded reliable values at depths shallower than 80 mbsf (Fig. **F32**). *P*-wave velocity increases with depth and varies between ~1535 and 1620 m/s. Deeper in the hole, *P*-wave velocity values from the WRMSL, SHMG, and bayonet yielded unreliable values. Based on visual inspection of the core, this unreliability is attributed to the low water content of the clays.

P-wave velocity SHMG measurements in the *z*-direction were measured on discrete samples below 500 mbsf. *P*-wave velocity is generally slower in the *z*-direction than it is in the *x*- and *y*-directions, and measurements in the other two directions could not be made. Between 500 and 850 mbsf, *P*-wave velocity ranges between 1400 and 1800 m/s, with no clear trend. Values below 1600 m/s are unreliable but may be a consequence of measuring *P*-wave velocity in the *z*-direction. At ~850 mbsf, a sharp increase of *P*-wave velocity is observed, but the increase is not correlated with a sharp increase of bulk density or a sharp decrease of porosity. The sharp increase of *P*-wave velocity in the basement reflects the low porosity and high consolidation of the rocks.

Thermal conductivity

Thermal conductivity measurements were performed on sediment whole-round cores using the needle-probe method and on lithified split cores using the half-space method (see **"Physical properties"** in the "Methods" chapter [Expedition 334 Scientists, 2012]). In general, thermal conductivity increases with depth and is inversely correlated to porosity (Fig. **F33**). In the uppermost 100 mbsf, variability is significant and may reflect cracking in the cores and changing lithologies. Relatively high values of thermal conductivity are present between ~50 and 90 mbsf and may be correlated with a section of siltstone. Below ~100 mbsf, thermal conductivity increases linearly with depth.

Downhole temperature

Downhole temperature was measured using the APCT-3. Six measurements were attempted between 30.2 and 90.2 mbsf in Hole U1379C (Table **T9;** Fig. **F33**). All measurements were made in lithostratigraphic Unit II. Sediment Temperature Tool measurements were not attempted at this site.

All measurements were made in a good sea state (<1 m swell), and all temperature-time series were recorded with a sample interval of 1 s. The temperature tool was stopped at the mudline for as long as 10 min prior to each penetration. The average bottom water temperature was 22.6°C (Table **T9**). Temperature-time series for each temperature measurement are shown in Figure **F34.** Significant frictional heating occurred on all penetrations of the APCT-3, with the temperature-time records exhibiting characteristic probe penetration and subsequent decay. Tool movement while the probe was in the sediment is minimal. The effective origin time of the frictional heat pulse was estimated by varying the assumed origin time until the thermal decay pulse best fit a theoretical curve. All of the measurements appear to be reliable. Equilibrium temperatures plotted as a function of depth are relatively linear; coupled with the average bottom water temperature, they give a least-squares gradient of 41.6°C/km (Fig. **F33**).

Heat flow

Because thermal conductivity appears relatively constant over the depth of temperature measurements, we computed the heat flow as the product of the thermal gradient and thermal conductivity. Using the mean thermal conductivity of 0.97 W/(m·K) gives a heat flow of 40 mW/m². This value is consistent with forearc values of heat flow.

If heat transfer is by conduction and heat flow is constant, the thermal gradient will be inversely proportional to thermal conductivity according to Fourier's law. This relationship can be linearized by plotting temperature as a function of summed thermal resistance (Bullard, 1939),

$$T(z) = T_o + q \times \Sigma[\Delta z_i/k(z)_i],\ i = 1{:}N,$$

where

T = temperature,
z = depth,
T_o = bottom water temperature,
q = heat flow, and
$[\Delta z_i/k(z)_i]$ = thermal resistance.

We assume a linear increase of thermal conductivity with depth and extrapolate temperatures to the sediment basement interface (Fig. F33). The estimated temperature at this depth is 48°C.

Vane shear

Undrained shear strength increases with depth (Fig. F35). The trend is approximately linear in the uppermost 80 mbsf, with a maximum value of 152 kPa. Below 80 mbsf, shear strength suddenly decreases and displays more erratic behavior. This change occurs near the depth where the coring method changed from APC to XCB.

Color spectroscopy

Color reflectance measurement results are presented in Figure F36. L* values are generally between 20 and 40. Regions of lower values correspond to ~40 and 200 mbsf. a* and b* values are inversely correlated. a* values are generally between –5 and 0 and b* values generally vary from –5 to 10.

Paleomagnetism

We made pass-through magnetometer measurements on all split-core archive sections with variable measuring intervals (2–10 cm). Discrete samples were also collected from the working halves of Hole U1379C at a spacing of one sample per section (1.5 m). In order to isolate the characteristic remanent magnetization (ChRM), we subjected the cores to alternating-field (AF) demagnetization. The split cores were typically demagnetized up to 30 mT. In order to test the split-core data, we demagnetized 85 discrete samples using progressive AF demagnetization techniques and measured them in both the superconducting rock magnetometer and JR6 magnetometer (see "Paleomagnetism" in the "Methods" chapter [Expedition 334 Scientists, 2012]). Cores 334-U1379C-1H through 17H were cored with the APC system using a nonmagnetic cutting shoe. These cores were oriented with the Flexit orientation tool. Unfortunately, crucial orientation data were lost during the coring process, which hampers the magnetostratigraphy investigation for Site U1379. Cores 334-U1379C-18X through 118X were cored with the XCB system using a standard cutting shoe.

Natural remanent magnetization

Downhole variations of paleomagnetic data obtained at Site U1379 are shown in Figure F37. The natural remanent magnetization (NRM) intensity is on the order of 10^{-2} to 10^{-1} A/m. Variations in NRM intensity of archive-half cores are correlated with lithology. Paleomagnetic measurements indicate that the olive-green sands in lithostratigraphic Unit III (~651–880 mbsf) have the lowest NRM intensity. A few discrete peaks of higher NRM values appear in some depth intervals in Units II and III (e.g., at ~100, ~490, and ~890 mbsf; Fig. F37), which can be tied directly to the presence of volcanic tephra in these regions (see "Lithostratigraphy and petrology"). Another peak occurs at ~590 mbsf, which is above the fault zone (see "Structural geology"). Below the peak at ~590 mbsf in the fault zone, NRM intensity slightly decreases. Magnetic susceptibility data also show positive peaks at these intervals (see "Physical properties").

As with cores recovered from nearly all ocean drilling programs, remagnetization imparted by the coring process is commonly encountered at Site U1379. NRM inclinations are strongly biased toward the vertical (mostly toward +90°) in a majority of cores. Upon AF demagnetization to 30 mT, a significant decrease in intensity (about one order of magnitude; Fig. F37) and a shift of inclination toward shallower values were observed. The inclination from the APC core (shallower than ~100 mbsf) became close to the expected time-averaged geomagnetic field inclination at this site (~±18°), whereas the inclinations from the XCB cores remain much steeper (~50°–60°).

The patterns of the magnetic declination are also different between APC- and XCB-cored sections. NRM declinations of APC cores are different from each other, which is expected. However, declinations of XCB cores show strong concentration along the +*x*-direction in the IODP coordinate scheme, with values highly clustered at 0°. Upon AF demagnetization, the declinations of XCB cores start to become randomly oriented. It appears that the core barrel assembly has a very strong effect on the declinations. The paleomagnetism of APC and XCB cores are discussed separately below.

Demagnetization behavior of APC cores

Although the APC core NRM obtained from the pass-through measurements were strongly affected by drilling overprint, as evidenced by the steep inclinations, AF demagnetization was effective in removing this overprint (Fig. F37). Moreover, declination is uniform within each core and different among cores (Fig. F38). This behavior is expected for the remanence of natural origin recovered by APC coring. APC coring minimizes the internal rotation of the core and therefore preserves the uniformity of remanence direction within the core. On the other hand, the core liner is arbitrarily oriented with respect to the direction of Earth's magnetic field and so is the IODP coordinate for each core. This produces ran-

dom declination among different cores, as shown in Figure F38.

The magnetic properties observed from the split cores were also confirmed by discrete sample measurements. The nearly vertical overprint was removed by AF demagnetization of 5–10 mT (e.g., Fig. F39A), and the stable component has a similar direction to those in the corresponding core sections (Fig. F37). AF demagnetization was extremely successful: 31 out of 32 tested samples revealed ChRM with maximum angular dispersion <15° (Kirschvink, 1980). Generally, NRM was completely demagnetized by ~40 mT.

Several spot readings in the pass-through measurements revealed negative inclinations (e.g., ~100 mbsf), but this behavior was not found in the ChRM of discrete samples except for a nearly horizontal inclination (–0.1°) in interval 334-U1379C-8H-4, 38 cm (Fig. F37).

Demagnetization behavior of XCB cores

NRM of XCB cores obtained by pass-through measurements also show a magnetic overprint with steep inclinations. Unlike APC cores, the inclinations in XCB cores are extremely stable and display only minor changes upon AF demagnetization at 30 mT (Fig. F39B). This stable overprint magnetization hindered retrieval of reliable paleomagnetic directions from the pass-through measurements of XCB cores.

The declinations of XCB cores further testify to the existence of this stable overprint. As shown in Figure F37A, NRM of XCB cores is almost invariably oriented parallel to the +*x*-direction, with declinations highly clustered at 0°. Because XCB coring produces internal rotation of the core, we expect remanence of natural origin to be randomly oriented throughout. The ~0° declinations of NRM of XCB cores strongly suggest an artificial overprint. Such orientation could derive from a radially inward magnetization induced by the coring process (e.g., Stokking et al., 1993). Interestingly, upon AF demagnetization the highly clustered declination pattern became random (Fig. F37B), suggesting that at least part of the radial-inward overprint was removed. Inclinations after AF demagnetization still maintained moderate to steep downward directions, suggesting that magnetization is still contaminated by the vertical overprint.

In an attempt to extract reliable paleomagnetic information from XCB cores, we performed progressive AF demagnetization experiments on discrete samples taken from the working halves. We observed steep inclinations and ~0° declinations in NRM measurements of the discrete samples (Fig. F39), indicating the existence of the radial-inward overprint. Seventeen samples out of 54 tested samples revealed ChRM with maximum angular dispersion <15°. Some other samples are either completely dominated by the artificial overprint or revealed scattered demagnetization behavior (Fig. F40). All samples showed rapid removal of near-vertical overprint at 5–15 mT demagnetization steps. The 17 ChRMs revealed a relatively uniform distribution for the declination. This may imply the success of removal of the radial overprint; however, the sample number is small and care must be taken. The inclination shows a broad distribution. Some inclination values are clearly higher than the theoretically expected value for the latitude of this site (17.3°), pointing to the incomplete removal of the vertical overprint or being affected by the steeper titling of bedding as observed in depth intervals below 600 mbsf (see **"Structural geology"**).

Implications for core orientation

Results from discrete sample demagnetization also provide an opportunity to evaluate the accuracy of the archive-half core remanence data that are used in combination with the discrete sample results to reorient core pieces to a common geographic framework. Paleomagnetic core reorientation method has been successfully used for both continental and oceanic outcrops (e.g., Fuller, 1969; Kodama, 1984; Shibuya et al., 1991). This method is to assume the direction of stable remanent magnetization, either viscous remanent magnetization or primary magnetization, with respect to a common reference line that is scribed the length of the core, represent the expected magnetic direction at site. The orientation of the paleomagnetic ChRM, which specifies the rotation of the core relative to the geographic coordinates, is then used to restore the azimuth of the core. For intervals of particular interest for structural geology at Site U1379, we used the stable ChRM isolated from progressive demagnetization of discrete samples.

For APC cores, both the pass-through and the discrete sample measurements indicate that after AF demagnetization, we can recover remanence of natural origin. XCB cores are more severely affected by drilling overprints. AF demagnetization appears successful in removing the radial overprint, implying the declination of ChRM may be reliable even when the vertical overprint was not completely removed. However, we suspect that some ChRM with steep (>45°) inclination either still exhibits a steep drilling overprint or they are affected by bed titling, and caution should be used with these core reorientation data.

Implication for magnetostratigraphy

We used ChRM inclinations from discrete measurements to define magnetic polarity sequences for Site U1379, although at low-latitude areas such as Site U1379, a near-180° shift in declination in the cores would be a more reliable sign of the polarity transition. For the uppermost part of lithostratigraphic Unit II, both pass-through and discrete sample measurements do not indicate reversed polarity of ChRM. Because the orientation data from the Flexit tool were lost, we cannot compare the declinations across APC cores to check whether there is a near-180° shift in declinations. However, we tentatively conclude that the APC-cored interval in Unit II is within the Brunhes Chron (<0.78 Ma).

In the lowermost part of lithostratigraphic Unit II, only one relatively well defined polarity interval was identified in the downhole magnetostratigraphic records at ~701–704 mbsf (Fig. **F37B**). Sections 334-U1379C-83X-3 and 83X-4 show dominantly reversed polarity after AF demagnetization. Discrete samples taken from these two sections also show negative inclinations, consistent with magnetization of these cores in a reversed field. Lower Pleistocene biostratigraphic Zone NN19 is also placed at this interval (see **"Paleontology and biostratigraphy"**). Using calcareous nannoplankton zonal schemes for the eastern equatorial Pacific for the lower boundary of Zone NN19 (2.3 Ma), this observed reversed polarity may correlate with Chron C1r.2r (1.185–1.778 Ma). If true, this would suggest extremely fast sedimentation accumulation rates (>388 m/m.y.) for Hole U1379C.

Paleomagnetic characterization of basement rocks

At the time of this writing, we have not obtained the shipboard paleomagnetic samples from the basement. Pass-through magnetic measurements indicate that NRM intensity of the basement rocks is on the same order as that of the overlying sediments.

Preliminary pass-through paleomagnetic data have revealed important magnetic signatures that await further verification in terms of age and origin. A strong radial overprint is observed in most cores below ~90 mbsf. The relative intensity of the two magnetic overprint components varies along the cores, suggesting that some physical properties of the sediment itself may play a role in the acquisition of the overprint. The core barrel assembly also has a very strong effect on the overprint. The average inclination of the cores recovered using the standard assembly is clearly different from that of the cores where the nonmagnetic assembly was used. Further integrated work with shipboard micropaleontological data and structural measurements and paleomagnetic study on discrete samples from each section are required to constrain the timing and origin of the magnetization recorded by the Hole U1379C sediments.

Downhole logging

Logging-while-drilling operations

Hole U1379A was drilled and logged with a Schlumberger LWD tool string that included (from top to bottom) the adnVISION 675 (density, neutron porosity, and ultrasonic caliper), the TeleScope 675 (measurement while drilling: power and data transmission and drilling parameters), the arcVISION 675 (propagation resistivity, gamma radiation, and annular pressure), and the geoVISION 675 (resistivity images and gamma radiation). The LWD tools were 6¾ inch diameter versions in a BHA with a 8½ inch bit and 6½ inch drill collars. For details, see **"Downhole logging"** in the "Methods" chapter (Expedition 334 Scientists, 2012).

Hole U1379A was spudded at 137 m drilling depth below rig floor (DRF) at 1000 h on 20 March 2011 (all times are local Costa Rica time, UTC – 6 h). Drilling started at high rates of penetration (ROPs) of 30–40 m/h in the first 6 h, slowing down to ~20 m/h afterward (these total drilling rates include time for pipe connections). Drilling proceeded smoothly until 624 mbsf at 1700 h on 21 March, when the driller noted high standpipe and downhole pressures and high torque on the top drive. Backreaming and mud sweeps were required to clean the hole before drilling could be resumed. These procedures were occasionally necessary while drilling the rest of the hole, but drilling progressed at overall ROP of ~8 m/h.

At 0300 h on 23 March, the real-time logs showed at 892 mbsf a sharp step change in resistivity from ~1 Ωm above to 2–3 Ωm below. This interface was interpreted as the boundary between slope sediments and basement. After logging this basement formation for ~75 m, drilling was stopped at 1100 h at a total depth of 966 mbsf, exceeding the original target depth of 950 mbsf.

The measurements recorded by the LWD tools were downloaded and processed successfully, except for the geoVISION data. The Schlumberger logging engineers noted that the geoVISION tool clock did not record time properly, and they sent the geoVISION data recorded in Hole U1379A to a Schlumberger LWD data processing center in Houston, Texas (USA), in an attempt to recover useful measurements. The data in the tool memory were found to

be corrupted beyond repair, and data recovery was unsuccessful. No geoVISION data are available for Hole U1379A.

Gas monitoring with logging-while-drilling measurements

As the first hole at Site U1379 was drilled with LWD, the LWD data had to be monitored for safety to detect gas entering the wellbore. As explained in "Downhole logging" in the "Methods" chapter (Expedition 334 Scientists, 2012), the primary measurement we used in the gas monitoring was the annular pressure measured while drilling by the arcVISION tool and transmitted in real time to the surface. We looked for sustained decreases of >30–50 psi in the annular pressure, which could be due to low-density gas entering the wellbore.

Figure F41 shows a residual pressure that is the measured annular pressure minus the hydrostatic pressure (for a seawater density of 1025 kg/m^3). The downward trend toward pressures higher than hydrostatic is due to solid particles that increase the effective density of the borehole fluid. The 50–100 psi downhole pressure fluctuations observed below 670 mbsf are likely due to cuttings restricting flow in the borehole annulus, which required backreaming and hole cleaning. These pressure fluctuations consisted of an increase followed by a decrease to the overall pressure trend as hole cleaning progressed. The only exception is a pressure decrease below 920 mbsf caused by an improvement in hole conditions in the basement rocks. No sustained pressure drops below the general trend that exceeded the 30–50 psi threshold set in the monitoring protocol and that could be due to gas entry were observed, and no drilling interruptions were necessary.

Logging data quality

Figure F41 also shows the quality control logs for Hole U1379A. A major control on LWD measurement quality is the borehole size, which is obtained by the adnVISION tool from the difference between the short- and long-spaced density measurements and from an ultrasonic traveltime measurement. Figure F41 shows the average borehole diameters estimated from these measurements. The most reliable measurement of borehole diameter is the ultrasonic caliper, which shows enlarged hole intervals (10–13 inches; 25–33 cm) from the seafloor to 120 mbsf and at 340–500 and 600–890 mbsf. The density correction, which is also calculated from the difference between the short- and long-spaced density measurements, generally varies from 0 to 0.2 g/cm^3. This correction, however, did not result in accurate density values in some enlarged hole intervals, where the measured LWD densities were anomalously low (see the comparison to core data below).

The average instantaneous ROP was ~80 m/h near the seafloor, decreasing to 20–40 m/h below 200 mbsf. This ROP is the rate of penetration of the LWD tools while the hole is being drilled and does not include time for pipe connections. geoVISION resistivity image quality is best for ROPs ~20 m/h, and in drilling Hole U1379A some resolution in the shallowest interval was traded for drilling time. Previous experience shows that high-quality geoVISION resistivity images can be acquired at ROPs as high as those employed while drilling Hole U1379A (e.g., Cook et al., 2009; Guerin et al., 2009). No geoVISION data are available for Hole U1379A, however, and the possible effect of ROP on the resistivity image quality cannot be assessed.

Depths relative to seafloor were fixed for all of the LWD logs by identifying the step change in the gamma ray and density logs associated with the seafloor. For Hole U1397A, the logging pick for the seafloor was at 133 m DRF, ~4 m above the seafloor depth estimated by the drillers. The rig floor logging datum was located 9.8 m above sea level.

Characterization of logging-while-drilling logs

Figure F42 is a summary of the LWD logs and images measured in Hole U1379A. The two density curves are conventional bulk density (RHOB) and density estimated from the adnVISION azimuthal measurements to minimize the effect of sensor standoff (image-derived density [IDRO]). These two density measurements give very similar values. Figure F42 also shows density porosity (ϕ) computed from the IDRO bulk density ρ_b as

$$\phi = (\rho_g - \rho_b)/(\rho_g - \rho_w),$$

where ρ_w is the water density and ρ_g the grain density. The density porosity curve in Figure F42 is calculated assuming a water density of 1.025 g/cm^3 and a grain density of 2.65 g/cm^3.

The comparison of density porosity and neutron porosity in Figure F42 shows that neutron porosity is always higher. As noted in "Downhole logging" in the "Methods" chapter (Expedition 334 Scientists, 2012), the likely reason for the higher porosity measured by the neutron log is the presence of clay minerals. The hydrogen in the clay mineral hydroxyls contributes to the slowing down of neutrons and increases the estimated porosity (Ellis, 1986). Density porosity is the more accurate measure of porosity in sediments containing appreciable amounts of clay.

Figure F42 also shows two propagation resistivity curves that span the resolution of the resistivities measured by the arcVISION tool. These resistivities are based on the attenuation and phase shifts of electromagnetic waves that travel through the formation (see "Downhole logging" in the "Methods" chapter [Expedition 334 Scientists, 2012] for details). The two resistivity curves in Figure F42 are the relatively low vertical resolution A40B, based on the attenuation measured at a transmitter–receiver separation of 40 inches (101.6 cm), and the high-resolution P16B, based on the phase shift measured at a transmitter–receiver separation of 16 inches (40.6 cm). The "B" in the acronym is for "blended," because these curves include measurements at the two electromagnetic wave frequencies used by the tool (400 kHz and 2 MHz).

To a first approximation, resistivity in a sediment sequence is controlled by porosity. The sediment grains are effectively insulators, and the medium that conducts electricity is saline water in the pore network. This implies a close inverse relationship between resistivity and sediment porosity and a direct relationship between resistivity and bulk density. These relationships are evident in Figure F42, with the exception of a few intervals where the logged densities show large negative peaks without corresponding drops in resistivity (e.g., 600–670 mbsf). This difference could be due to a measured log density that is too low in enlarged hole intervals (see the hole diameter logs in Fig. F41) and is discussed below, also taking into account core measurements.

Finally, Figure F42 shows two images of bulk density and borehole radius measured by the adnVISION tool. The image display is highly compressed in the vertical direction. For a 10 inch (25.4 cm) diameter borehole, the unwrapped borehole images are ~80 cm wide and the vertical scale is compressed by a factor of ~150:1 in the images of Figure F42.

These images are obtained by azimuthal measurements in 16 sectors and thus are sampled at a relatively coarse interval of 22.5°. Because of their limited angular resolution, these images typically do not resolve fine-scale sedimentary or structural features. On the other hand, the radius image clearly displays vertical bands of large borehole radius, which are typically interpreted as borehole breakouts caused by differences in the principal horizontal stresses (e.g., Chang et al., 2010). Borehole breakouts in Hole U1379A are analyzed below.

Logging units

We define four logging units on the basis of the variation in logging properties displayed in Figure F42. Logging Unit 1 (0–492 mbsf) corresponds to a compacting sequence where the density and resistivity progressively increase and density porosity decreases with depth, reaching nearly constant values of ~1.9 g/cm^3, 1 Ωm, and 45% porosity at the base of the unit. The NGR log shows an initial increase from the seafloor (~30 gAPI) to 220 mbsf (~50 gAPI) and then shows minor fluctuations around a constant value to the base of the unit, except for a sharp peak in NGR at 476 mbsf corresponding to volcanic ash layers in Core 334-U1379A-58X (see "Lithostratigraphy and petrology").

The top of logging Unit 2 (492–600 mbsf) is marked by a small density and resistivity step increase that remains constant within this unit at ~2 g/cm^3 and 1.3 Ωm. The average density porosity is ~40% and the NGR log shows constant values of ~50 gAPI. Logging Unit 3 (600–892 mbsf) does not show an appreciable change in resistivity from the unit above, but it is clearly distinct because it contains many borehole enlargements, clearly shown by the borehole diameter logs in Figure F41 and the borehole radius image in Figure F42. Although density follows an increasing trend with depth, the logged values show large fluctuations with sharp negative peaks caused by borehole enlargements. These enlargements are likely to correspond to intervals containing unconsolidated sands or fractured intervals, which are prone to washout during drilling. For example, a negative excursion in the density log at 640–650 mbsf corresponds to fractured and brecciated zones in Cores 334-U1379C-76X and 77X (see "Structural geology" and "Core-log integration"). The cores also have higher sand content in logging Unit 3 compared to the sediment above (see "Lithostratigraphy and petrology").

Logging Unit 4 (892–955 mbsf) corresponds to the basement rocks of the sedimentary sequence, inferred by the seismic reflection profile and confirmed by coring in Hole U1379C. The top of logging Unit 4 is clearly identified by a sharp shift in baseline NGR, photoelectric factor, density, and resistivity logs. Compared to the slope sediments above, this unit shows a markedly higher average density and resistivity (2.3 g/cm^3 and 2.5 Ωm) and lower density porosity (~20%). These properties indicate a well-lithified sedimentary rock. In this unit, the resistivity logs show local peaks that reach 5–6 Ωm, suggesting lithologic variation such as blocks of more lithified rocks in the basement. Differences in NGR and photoelectric factor with the sediments above suggest a different mineral composition.

Borehole breakout analyses

Borehole breakout analyses were performed to assess the orientation of the maximum horizontal stress di-

rection within the borehole. Although these density and radius images are sampled only in 16 azimuthal sectors (every 22.5°), obvious breakout features appear as two vertical dark bands in both images from Hole U1379A (Fig. F42). As borehole radius images are constructed by direct measurement of borehole diameter, these images were used to estimate borehole morphology. No obvious borehole breakouts are identified in the interval from the seafloor to 292 mbsf and in the basement, and breakouts occur discontinuously in the interval between 292 and 885 mbsf as two vertical bands separated by 180°. The widths of the breakout bands are variable and typically range from 20° to 90°. The breakout bands are wider and show a complicated morphology at 335–445 and 600–682 mbsf because of a large-diameter, irregular borehole. In contrast, distinct narrow breakouts are developed at 445–600 and 720–860 mbsf, where the borehole is less enlarged (Fig. F43). The average azimuth of the breakouts is roughly north–south to north-northwest–south-southeast with a range of three sectors (315°–22.5°), indicating that the maximum horizontal stress is oriented east–west to east-northeast–west-southwest. Detailed statistical analyses of breakout azimuths and widths will be conducted postexpedition.

Core-log integration

Figure F44 is a comparison of NGR, bulk density, and porosity measurements made by LWD in Hole U1379A and in core samples in Hole U1379C. This comparison is useful to correlate depths in the LWD logs and depths of core samples and to integrate information from log and core measurements.

NGR log measurements are calibrated to a degree API (gAPI) scale by comparison to a standard artificial formation built to simulate about twice the radioactivity of a typical shale and conventionally set to 200 gAPI (Ellis and Singer, 2007). The NGR measurement made on whole-core sections on the R/V *JOIDES Resolution* is in counts per second (for a detailed description of the NGR apparatus, see Vasiliev et al., 2010). The comparison of log and core NGR measurements in Figure F44 shows that their curves overlap if 1 cps equals ~2 gAPI. Occasionally, low NGR values are measured at the end of core sections. To avoid these end effects, measurements from the uppermost and lowermost 10 cm of each section have been excluded from the NGR data plotted in Figure F44. Most patterns in the log and core NGR records match closely, with only a few exceptions (e.g., the high NGR values at 270–315 mbsf or the sharp peak in the downhole log at 476 mbsf). This general agreement indicates a close correlation in the depths of the log and core records.

Figure F44 also compares IDRO logs to densities measured on whole-core sections by GRA and on discrete core samples by MAD analysis. The bulk density values are generally comparable, with the exception of several intervals where the log densities are clearly lower than the core densities (e.g., from the seafloor to 20 mbsf or at 600–670 mbsf). Possible reasons for these differences are discussed in the next section.

An interesting interval in this bulk density comparison is between 110 and 500 mbsf, where the core densities are systematically lower than the logged densities. The difference is ~0.05 g/cm^3, or ~3% of the bulk density. Several cores in this depth interval showed >100% recovery, and the small decrease in density between core and log may be due to core expansion by elastic rebound (Moran, 1997). The MAD porosities are density porosities calculated with the measured grain densities in each sample. As the MAD densities in this interval are slightly lower than the log densities, the MAD porosities are slightly higher than the porosities computed from the density log.

Figure F45 shows a detailed comparison of log and core data in an interval near the top of logging Unit 3 where there are large fluctuations in borehole size. The purpose of this comparison is to distinguish low logged density values that are due to an enlarged borehole from log measurements that are representative of formation properties. As noted earlier, the electrical resistivity is mostly controlled by water content and hence porosity, and the logged electrical resistivities are not very sensitive to borehole size. Therefore, a negative peak in logged density that corresponds to a borehole enlargement but is not matched by a low electrical resistivity suggests that the measured density is affected by borehole size. A few of these density lows caused by borehole size are indicated in Figure F45. Also, the porosities of ~80% corresponding to these density lows are unrealistically high.

Intervals do exist, however, where low logged densities correspond to low resistivities (e.g., 616–619 and 642.5–644.5 mbsf; shaded intervals in Fig. F45). The low density logged in these intervals is likely to be representative of the actual formation density. This conclusion is supported by MAD measurements at 616–619 mbsf, which also show a density decrease. The fractured and brecciated zone observed in Cores 334-U1379C-76X and 77X corresponds to an interval where MAD data do not match the low logged densities (642.5–644.5 mbsf). The low logged density and resistivity values in this interval may reflect in situ fracture porosity, which is not measured in the MAD samples.

References

Berggren, W.A, Hilgen, F.J., Langereis, C.G., Kent, D.V., Obradovich, J.D., Raffi, I., Raymo, M.E., and Shackelton, N.J., 1995a. Late Neogene chronology: new perspectives in high-resolution stratigraphy. *Geol. Soc. Am. Bull.,* 107(11):1272–1287. **doi:10.1130/0016-7606(1995)107<1272:LNCNPI>2.3.CO;2**

Berggren, W.A., Kent, D.V., Swisher, C.C., III, and Aubry, M.-P., 1995b. A revised Cenozoic geochronology and chronostratigraphy. *In* Berggren, W.A., Kent, D.V., Aubry, M.-P., and Hardenbol, J. (Eds.), *Geochronology, Time Scales and Global Stratigraphic Correlation.* Spec. Publ.—SEPM (Soc. Sediment. Geol.), 54:129–212.

Brothers, R.J., Kemp, A.E.S., and Maltman, A.J., 1996. Mechanical development of vein structures due to the passage of earthquake waves through poorly consolidated sediments. *Tectonophysics,* 260(4):227–244. **doi:10.1016/0040-1951(96)00088-1**

Bullard, E.C., 1939. Heat flow in South Africa. *Proc. R. Soc. London, Ser. A,* 173(955):474–502. **doi:10.1098/rspa.1939.0159**

Chang, C., McNeill, L.C., Moore, J.C., Lin, W., Conin, M., and Yamada, Y., 2010. In situ stress state in the Nankai accretionary wedge estimated from borehole wall failures. *Geochem., Geophys., Geosyst.,* 11:Q0AD04. **doi:10.1029/2010GC003261**

Cook, A., Guerin, G., Mrozewski, S., Collett, T., and Boswell, R., 2009. Gulf of Mexico gas hydrate joint industry project Leg II—Walker Ridge 313 LWD operations and results. *Proc. Drill. Sci. Results 2009 Gulf of Mexico Gas Hydrate Jt. Ind. Proj. Leg II.* **http://www.netl.doe.gov/technologies/oil-gas/publications/Hydrates/2009Reports/WR313LWDOps.pdf**

DeMets, C., 2001. A new estimate for present-day Cocos-Caribbean plate motion: implications for slip along the Central American volcanic arc. *Geophys. Res. Lett.,* 28(21):4043–4046. **doi:10.1029/2001GL013518**

Ellis, D.V., 1986. Neutron porosity devices—what do they measure? *First Break,* 4(3):11–17. **doi:10.3997/1365-2397.1986005**

Ellis, D.V., and Singer, J.M., 2007. *Well Logging for Earth Scientists,* (2nd ed.): Dordrecht, The Netherlands (Springer).

Expedition 334 Scientists, 2012. Methods. *In* Vannucchi, P., Ujiie, K., Stroncik, N., Malinverno, A., and the Expedition 334 Scientists, *Proc. IODP,* 334: Tokyo (Integrated Ocean Drilling Program Management International, Inc.). **doi:10.2204/iodp.proc.334.102.2012**

Fuller, M., 1969. Magnetic orientation of borehole cores. *Geophysics,* 34(5):772–774. **doi:10.1190/1.1440047**

Grevemeyer, I., Kopf, A.J., Fekete, N., Kaul, N., Villinger, H.W., Heesemann, M., Wallmann, K., Spiess, V., Gennerich, H.-H., Muller, M., and Weinrebe, W., 2004. Fluid flow through active mud dome Mound Culebra offshore Nicoya Peninsula, Costa Rica: evidence from heat flow surveying. *Mar. Geol.,* 207(1–4):145–157. **doi:10.1016/j.margeo.2004.04.002**

Grimm, K.A., and Orange, D.L., 1997. Synsedimentary fracturing, fluid migration, and subaqueous mass wasting: intrastratal microfractured zones in laminated diatomaceous sediments, Miocene Monterey Formation, California, U.S.A. *J. Sediment. Res.,* 67(3):601–613. **doi:10.1306/D42685E5-2B26-11D7-8648000102C1865D**

Guerin, G., Cook, A., Mrozewski, S., Collett, T., and Boswell, R., 2009. Gulf of Mexico gas hydrate joint industry project Leg II—Green Canyon 955 LWD operations and results. *Proc. Drill. Sci. Results 2009 Gulf of Mexico Gas Hydrate Jt. Ind. Proj. Leg II.* **http://www.netl.doe.gov/technologies/oil-gas/publications/Hydrates/2009Reports/GC955LWDOps.pdf**

Hanamura, Y., and Ogawa, Y., 1993. Layer-parallel faults, duplexes, imbricate thrusts and vein structures of the Miura Group: keys to understanding the Izu fore-arc sediment accretion to the Honshu fore arc. *Isl. Arc,* 2(3):126–141. **doi:10.1111/j.1440-1738.1993.tb00081.x**

Harris, R.N., Spinelli, G., Ranero, C.R., Grevemeyer, I., Villinger, H., and Barckhausen, U., 2010. Thermal regime of the Costa Rican convergent margin: 2. Thermal models of the shallow Middle America subduction zone offshore Costa Rica. *Geochem., Geophys., Geosyst.,* 11(12):Q12S29. **doi:10.1029/2010GC003273**

Ingle, J.C., Jr., Keller, G., and Kolpack, R.L., 1980. Benthic foraminiferal biofacies, sediments and water masses of the southern Peru-Chile Trench area, southeastern Pacific Ocean. *Micropaleontology,* 26(2):113–150. **doi:10.2307/1485435**

Kirschvink, J.L., 1980. The least-squares line and plane and the analysis of palaeomagnetic data. *Geophys. J. R. Astron. Soc.,* 62(3):699–718. **doi:10.1111/j.1365-246X.1980.tb02601.x**

Kodama, K.P., 1984. Palaeomagnetism of granitic intrusives from the Precambrian basement under eastern Kansas: orienting drill cores using secondary magnetization components. *Geophys. J. R. Astron. Soc.,* 76(2):273–287. **doi:10.1111/j.1365-246X.1984.tb05045.x**

LaFemina, P., Dixon, T.H., Govers, R., Norabuena, E., Turner, H., Saballos, A., Mattioli, G., Protti, M., and Strauch, W., 2009. Fore-arc motion and Cocos Ridge collision in Central America. *Geochem., Geophys., Geosyst.,* 10(5):Q05S14. **doi:10.1029/2008GC002181**

Martini, E., 1971. Standard Tertiary and Quaternary calcareous nannoplankton zonation. *Proc. Second Planktonic Conf. Roma 1970,* 2:739–785.

Moran, K., 1997. Elastic property corrections applied to Leg 154 sediment, Ceara Rise. *In* Shackleton, N.J., Curry, W.B., Richter, C., and Bralower, T.J. (Eds.), *Proc. ODP, Sci. Results,* 154: College Station, TX (Ocean Drilling Program), 151–155. **doi:10.2973/odp.proc.sr.154.132.1997**

Shibuya, H., Merrill, D.L., Hsu, V., and Leg 124 Shipboard Scientific Party, 1991. Paleogene counterclockwise rotation of the Celebes Sea—orientation of ODP cores utilizing the secondary magnetization. *In* Silver, E.A., Rangin, C., von Breymann, M.T., et al., *Proc. ODP, Sci. Results,* 124: College Station, TX (Ocean Drilling Program), 519–523. **doi:10.2973/odp.proc.sr.124.169.1991**

Stokking, L., Musgrave, R., Bontempo, D., Autio, W., Rabinowitz, P.D., Baldauf, J., and Francis, T.J.G., 1993. Handbook for shipboard paleomagnetists. *ODP Tech. Note,* 18. **doi:10.2973/odp.tn.18.1993**

Vannucchi, P., Fisher, D.M., Bier, S., and Gardner, T.W., 2006. From seamount accretion to tectonic erosion: formation of Osa mélange and the effects of Cocos Ridge subduction in southern Costa Rica. *Tectonics*, 25(4):TC2004. **doi:10.1029/2005TC001855**

Vasiliev, M.A., Blum, P., Chubarian, G., Olsen, R., Bennight, C., Cobine, T., Fackler, D., Hastedt, M., Houpt, D., Mateo, Z., and Vasilieva, Y.B., 2011. A new natural gamma radiation measurement system for marine sediment and rock analysis. *J. Appl. Geophys.,* 75(3):455–463. **doi:10.1016/j.jappgeo.2011.08.008**

Wade, B.S., Pearson, P.N., Berggren, W.A., and Pälike, H., 2011. Review and revision of Cenozoic tropical planktonic foraminiferal biostratigraphy and calibration to the geomagnetic polarity and astronomical time scale. *Earth-Sci. Rev.,* 104(1–3):111–142. **doi:10.1016/j.earscirev.2010.09.003**

Zijderveld, J.D.A., 1967. AC demagnetization of rocks: analysis of results. *In* Collinson, D.W., Creer, K.M., and Runcorn, S.K. (Eds.), *Methods in Palaeomagnetism:* New York (Elsevier), 254–286.

Publication: 12 April 2012
MS 334-104

Figure F1. Prestack depth-migrated seismic BGR99 Line 7 showing locations of Sites U1378 and U1379 on the middle and upper slope, respectively. CMP = common midpoint.

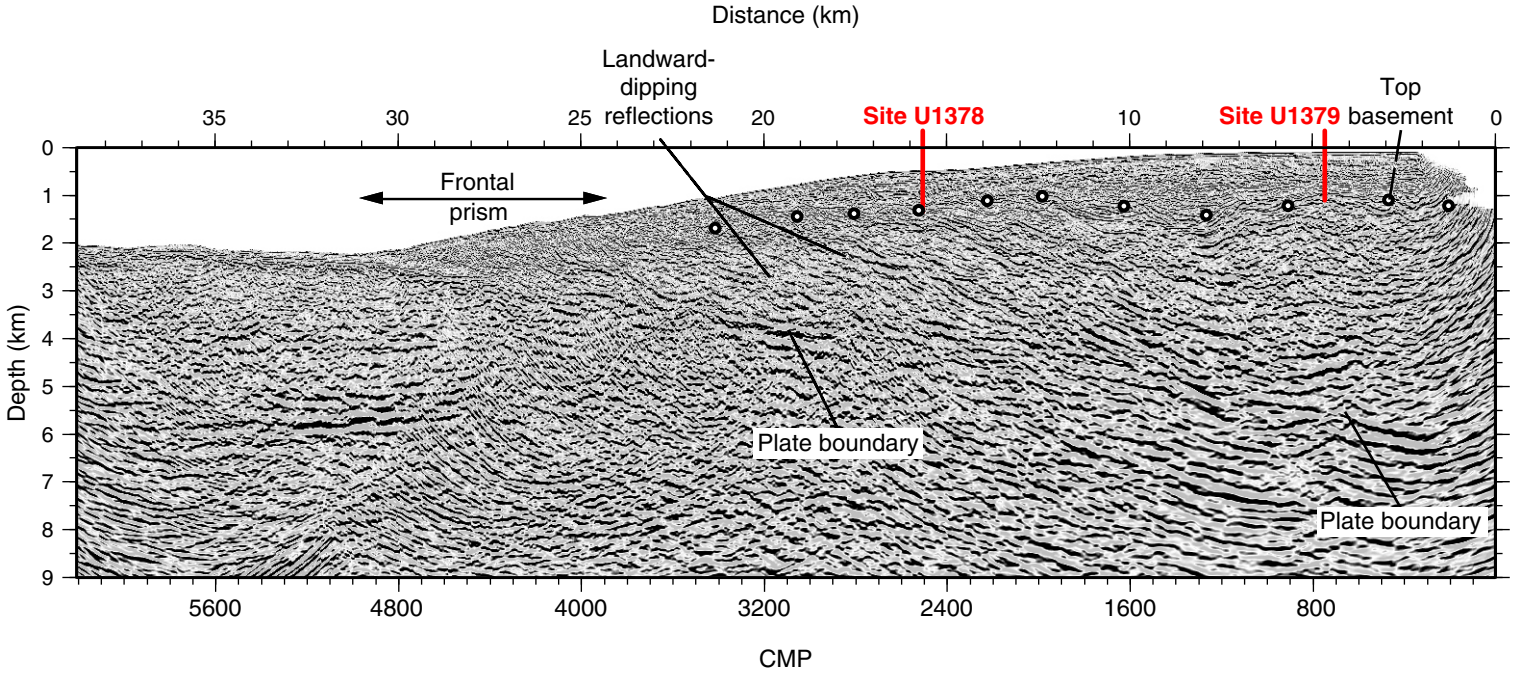

Figure F2. Detail of poststack time-migrated seismic BGR99 Line 7 centered at Site U1379. CMP = common midpoint.

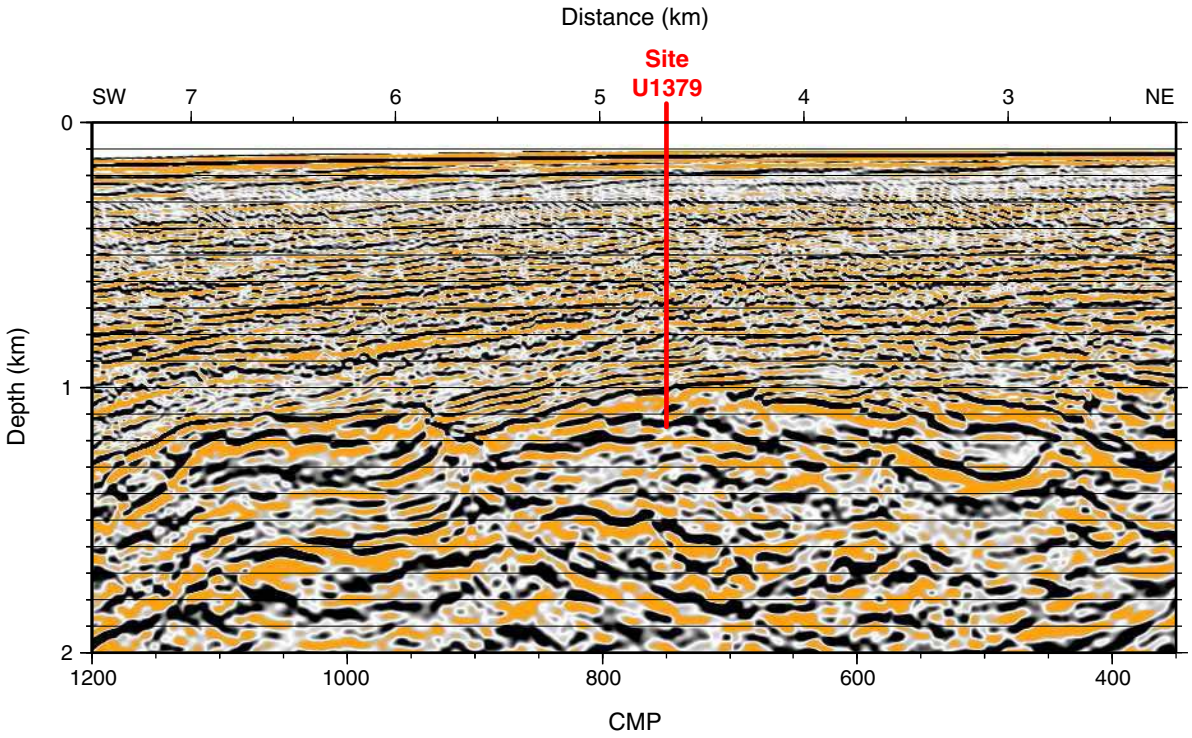

Figure F3. Graphic summary log, Hole U1379C.

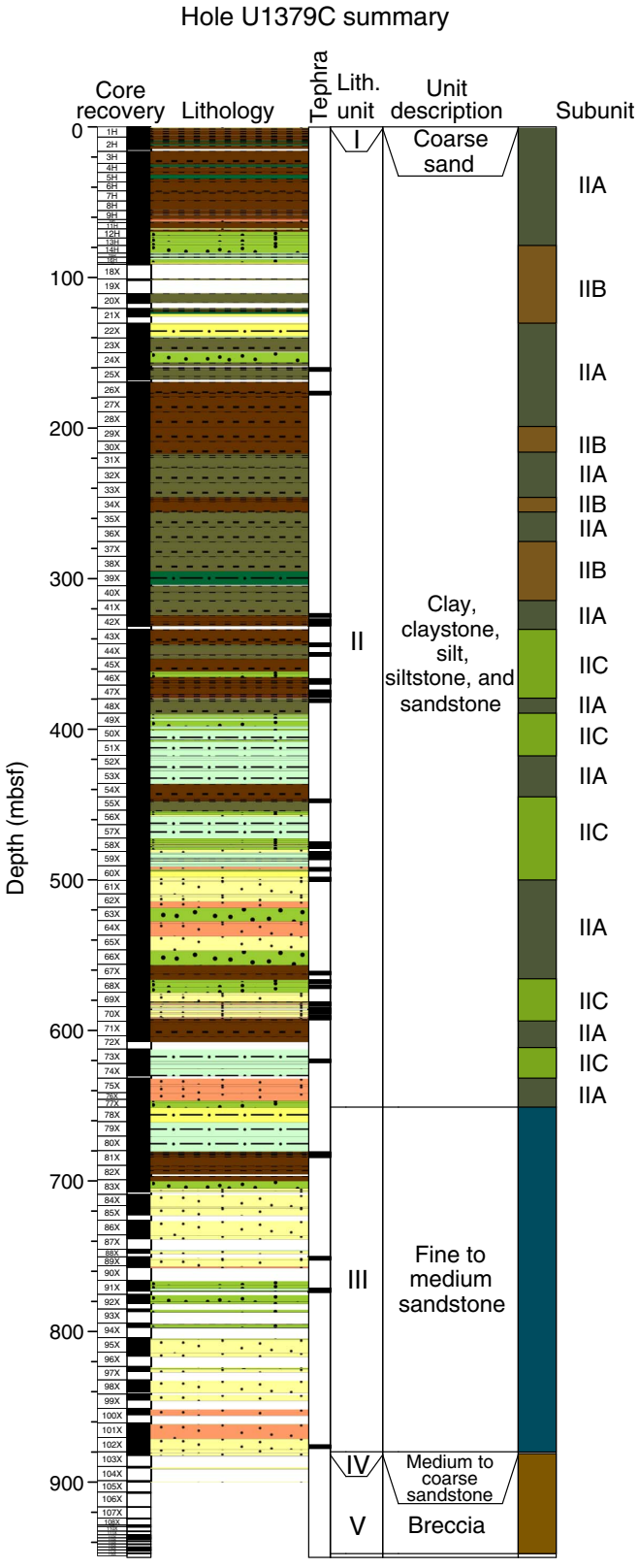

Figure F4. Representative core image of Unit I (interval 334-U1379C-1H-1, 53–63 cm).

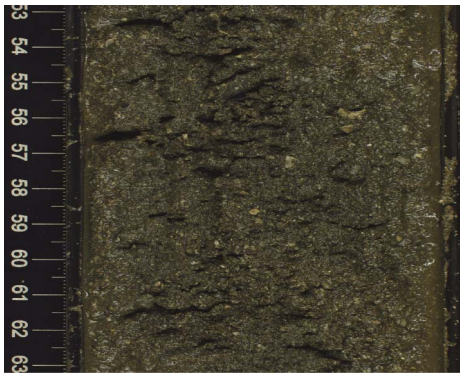

Figure F5. Representative core image of Subunit IIA (interval 334-U1379C-24X-3, 60–69 cm).

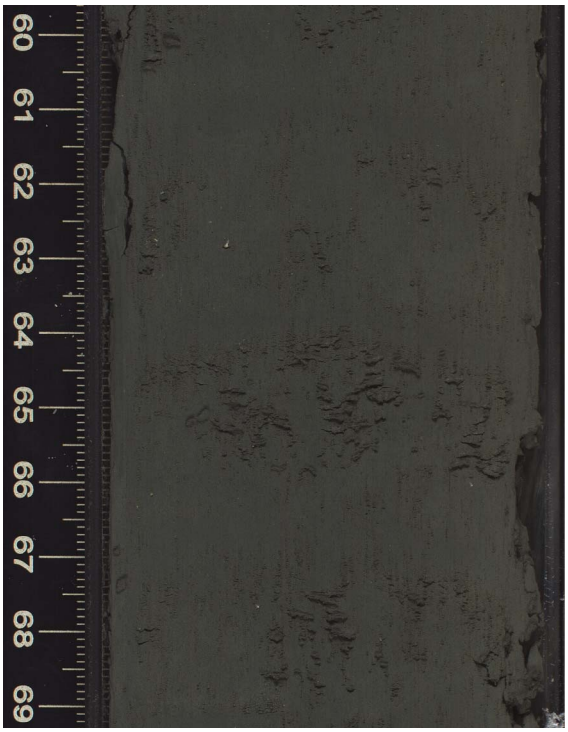

Figure F6. Representative core image of Subunit IIB (interval 334-U1379C-16H-1, 100–115 cm).

Figure F7. Representative core image of Subunit IIC (interval 334-U1379C-73X-3, 80–92 cm).

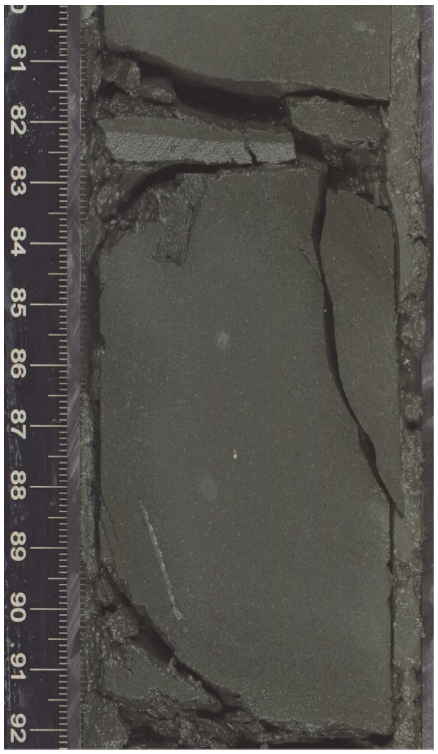

Figure F8. Representative core image of Unit III, which is characterized by coarse sand mixed with large mud pebbles (interval 334-U1379C-82X-6, 65–75 cm).

Figure F9. Representative core image of Unit IV with a calcite-cemented shell-shard horizon (interval 334-U1379C-103X-1, 50–60 cm).

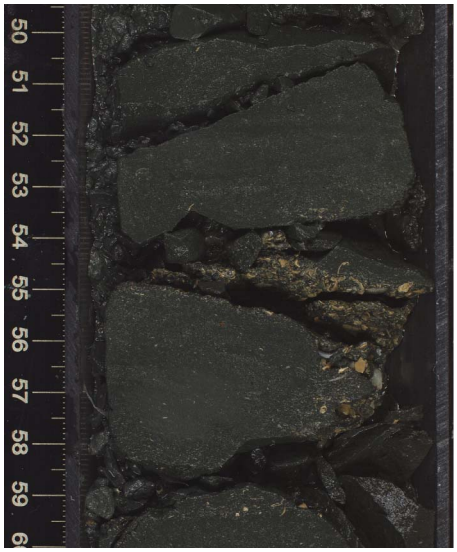

Figure F10. Core image of the Unit IV/V boundary (interval 334-U1379C-103X-3, 18–34 cm).

Figure F11. Core image of moderately phyric plagioclase basalt. The basalt is overprinted by a network of cross-cutting veins (interval 334-U1379C-103X-CC, 0–13 cm).

Figure F12. Core image of pinkish white tephra layer with normal gradation from medium ash at the base to fine ash at the top. The lower, darker portions of the tephra layer are characterized by heavy mineral enrichment (interval 334-U1379C-26X-5, 128–143 cm).

Figure F13. A. Representative X-ray diffractogram showing peaks consistent with quartz, calcite, and anorthite in Subunit IIA, Site U1379. **B.** Representative X-ray diffractogram showing the occurrence of calcite, magnesium-rich calcite, and aragonite in Subunit IIB.

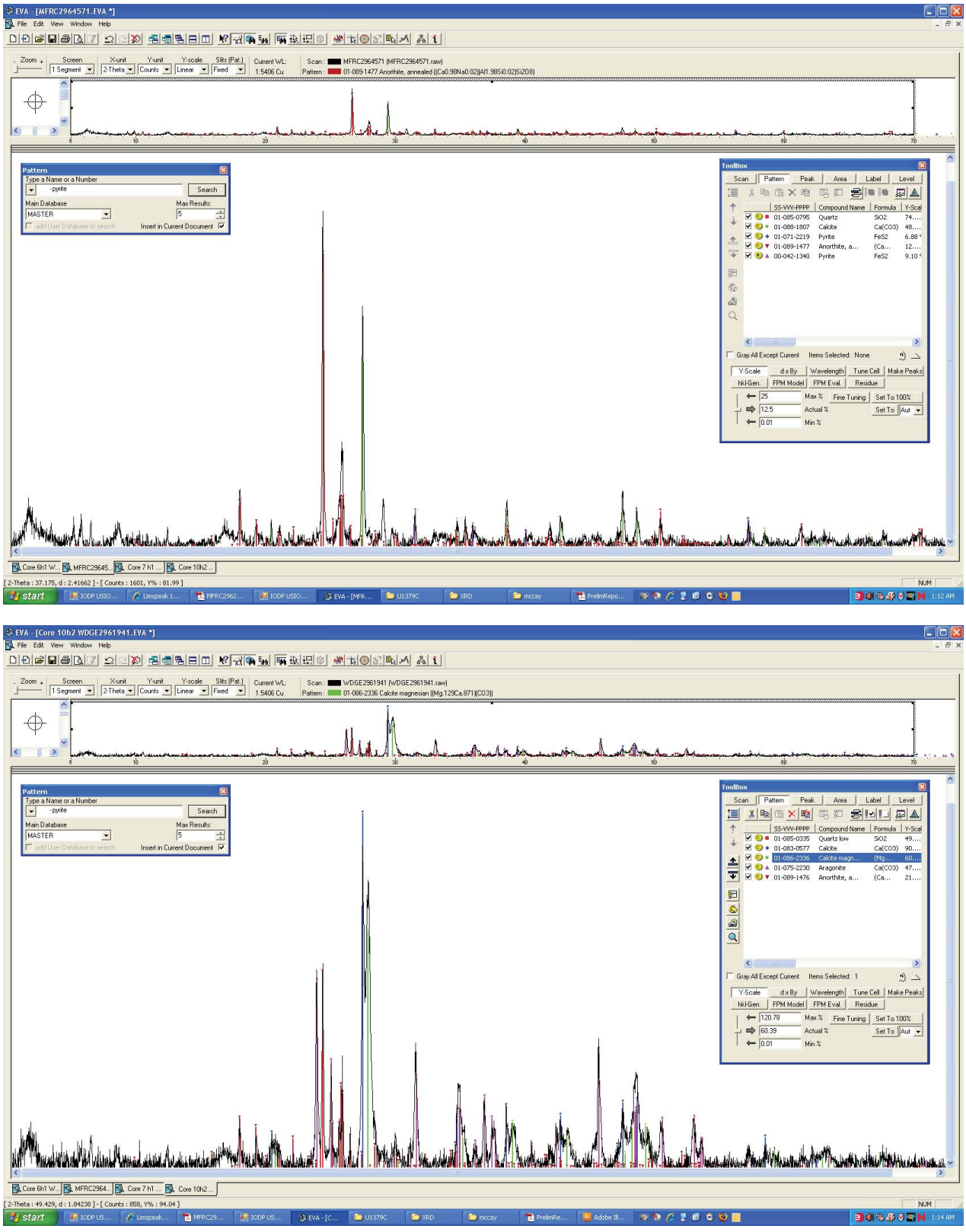

Figure F14. Late Neogene biostratigraphic zonation used for Hole U1379C. Numerical ages are based on Berggren et al. (1995a, 1995b) and Wade et al. (2011).

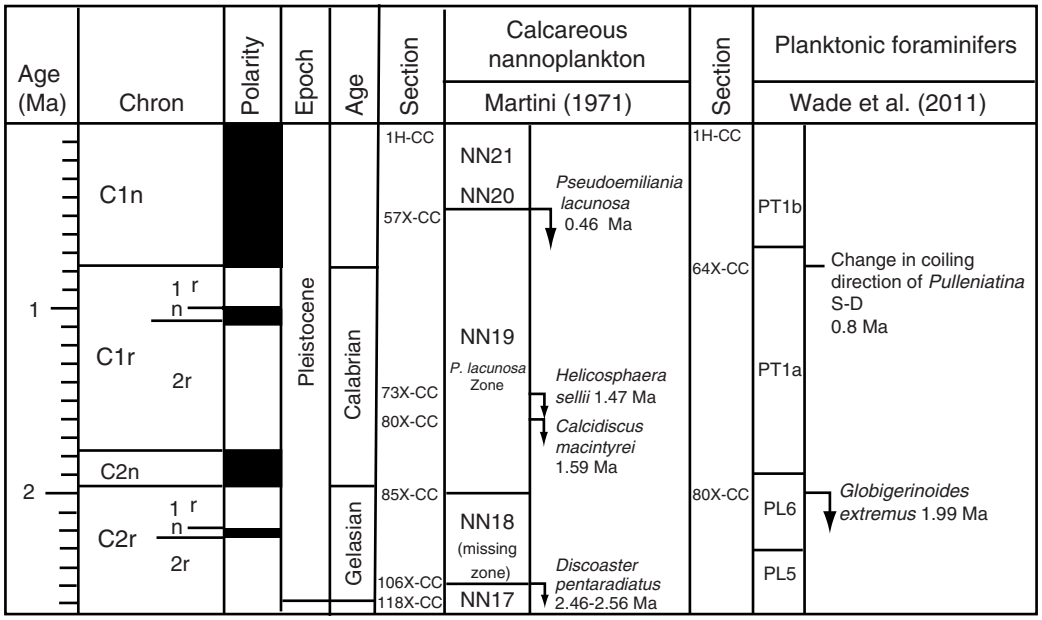

Figure F15. Age-depth plot based on the last occurrences (LOs) and biostratigraphic zonal intervals of calcareous nannofossils at Site U1379. Approximate sediment accumulation rates (red dashed line) are based on the LO of *Pseudoemiliania lacunosa* in Sample 334-U1379C-57X-CC (476.20 mbsf), the LO of *Helicosphaera sellii* in Sample 73X-CC (622.28 mbsf), the LO of *Calcidiscus macintyrei* in Sample 80X-CC (679.99 mbsf), the last confirmed sample of the *P. lacunosa* Zone in Sample 85X-CC (722.48 mbsf), and the *Discoaster pentaradiatus* Zone in Samples 106X-CC through 118X-CC (907.14–947.25 mbsf).

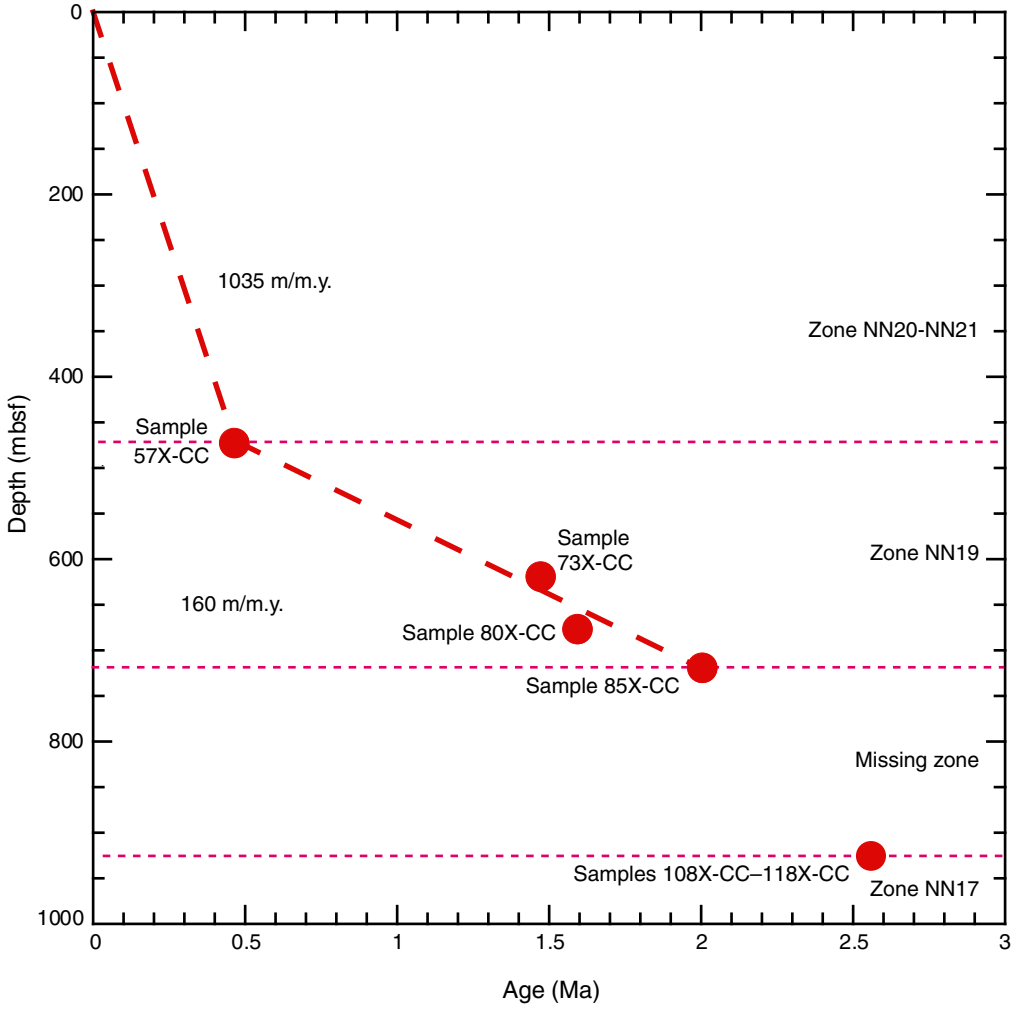

Figure F16. Plot of bedding dips, faults, and fractures as a function of depth, Hole U1379C. Shaded bands indicate four fault zones recognized in the slope sediments.

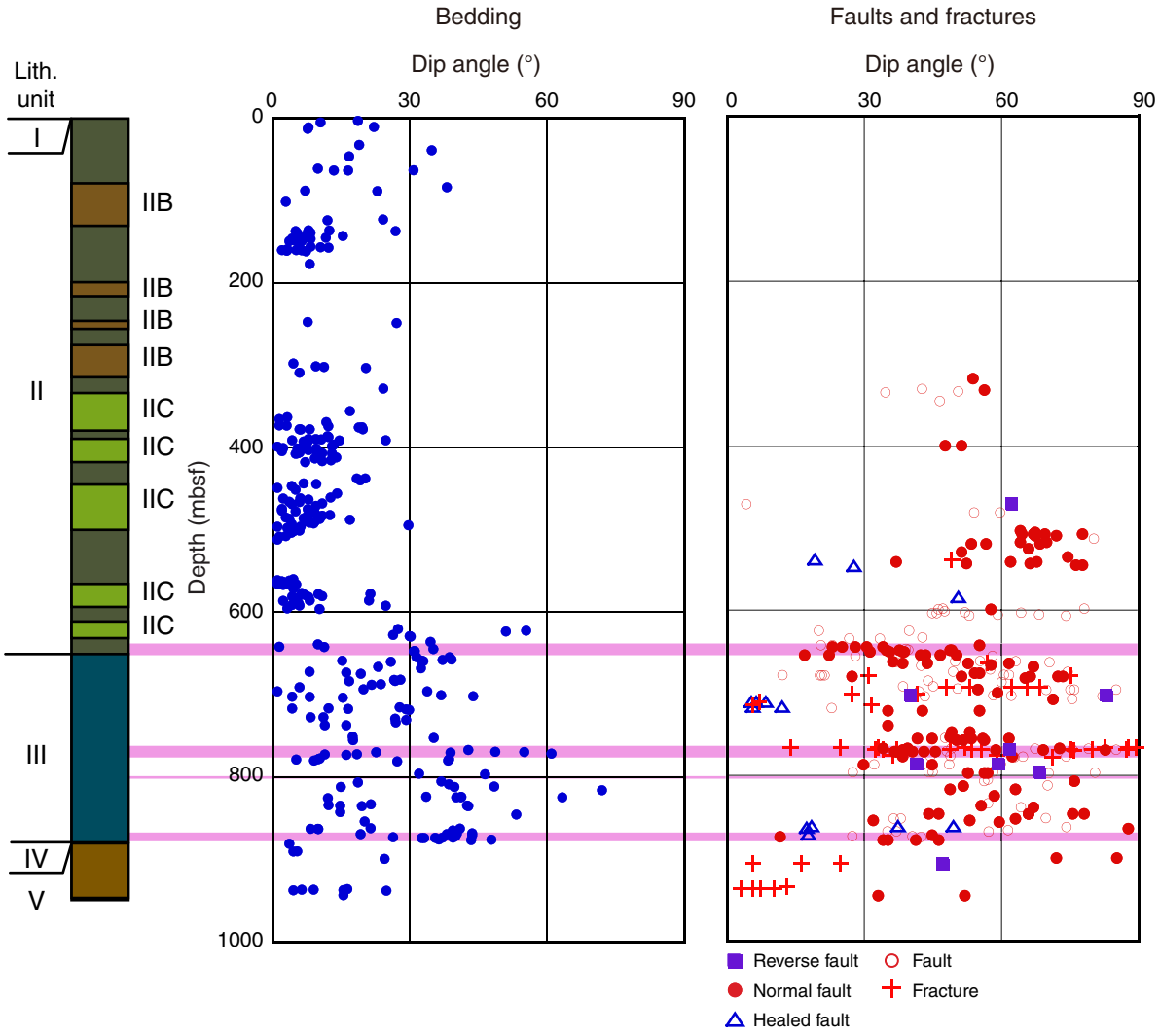

Figure F17. Lower hemisphere equal area projection of bedding planes (large circles) with poles (solid circles) after paleomagnetic corrections, Hole U1379C.

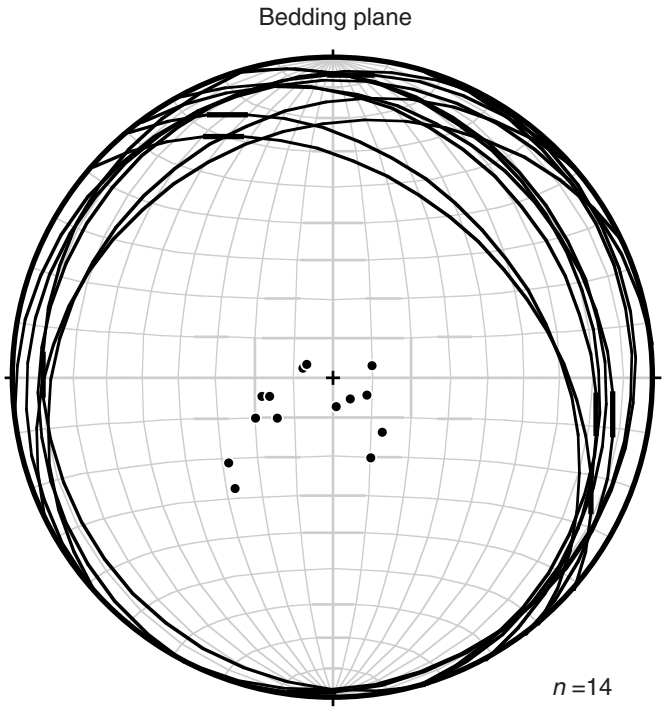

Figure F18. Photograph of an example of slickensides used to constrain slip sense, Hole U1379C. Dashed line is the trend of slickenline, and the white arrow is the slickenstep.

Figure F19. A. Lower hemisphere equal area projection of normal fault planes (large circles) with striae (solid circles) after paleomagnetic corrections, Hole U1379C. Fault dips are primarily north and south along east–west trending faults. A small number of westward-dipping normal faults are also apparent. Arrows indicate the movement direction of the hanging wall based on the slickenlines on the fault plane. **B.** Kinematic solution for the population of normal faults in Hole U1379C shown in A with P (compression, red) and T (extension, blue) axes for each fault and compressional (transparent) and associated extensional (gray shaded) quadrants.

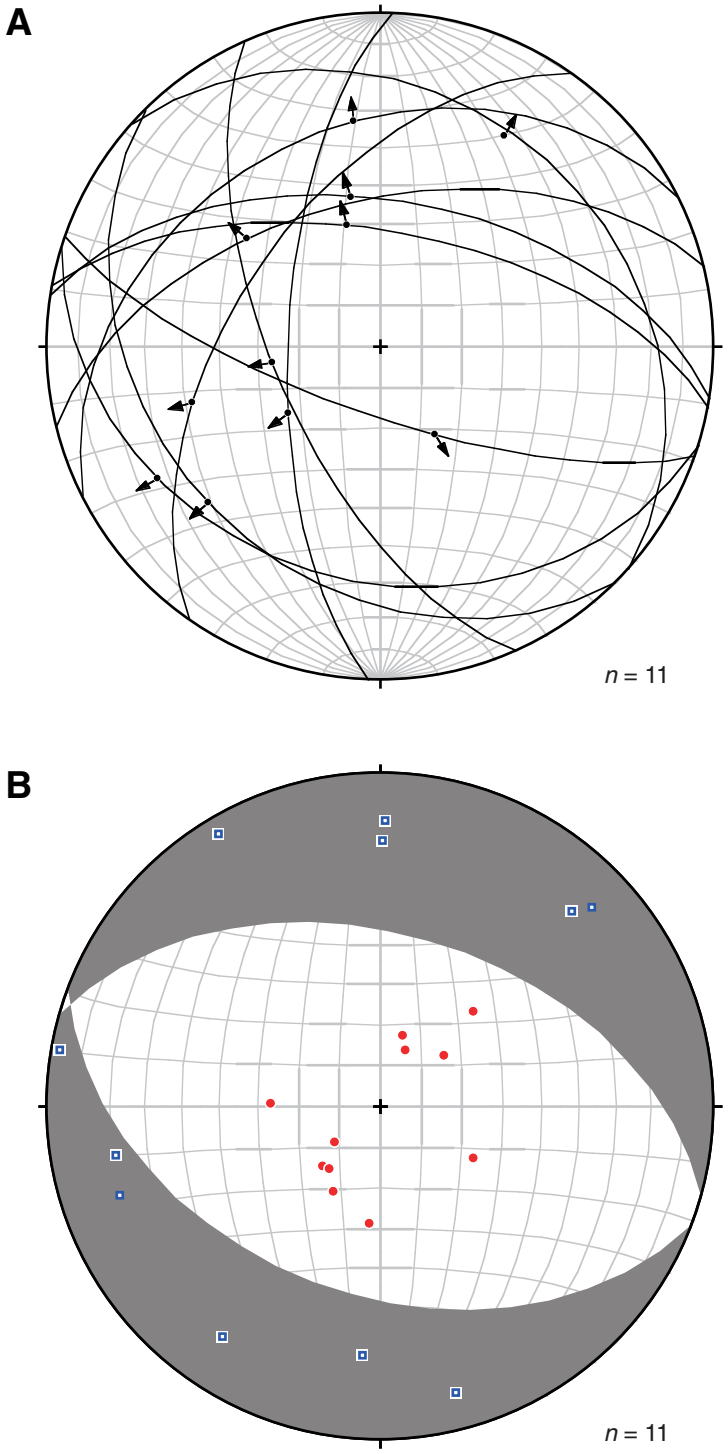

Figure F20. Core image and sketch of healed normal fault truncated by a subhorizontal healed fault, Hole U1379C. Half arrows indicate sense of shear as identified by the offset of bedding and lamina.

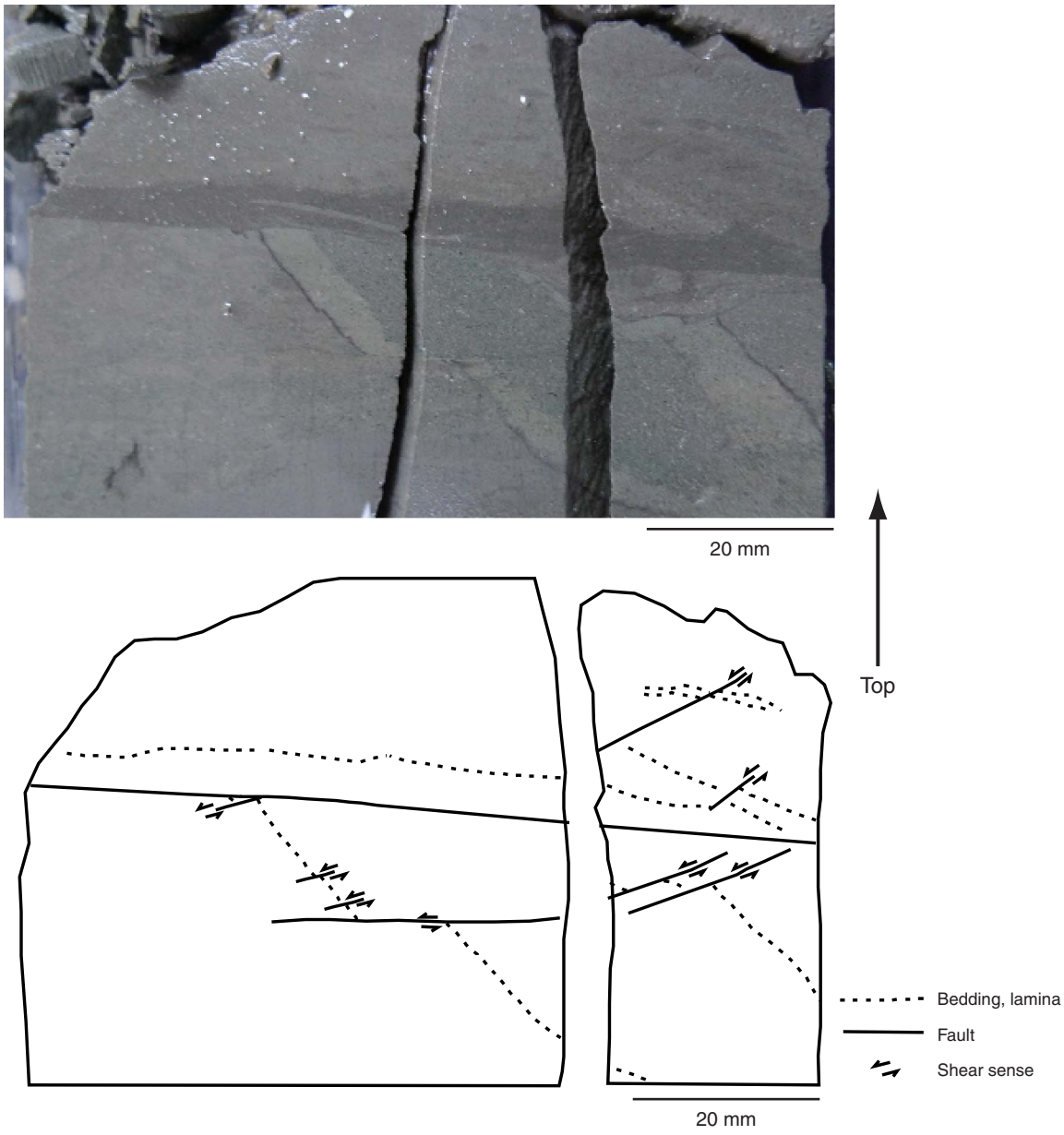

Figure F21. Core images of fractured and brecciated zones from the upper fault zone between 642.1 and 652.8 mbsf, Hole U1379C. Note the dominant fragment size (<1 cm) within the brecciated zone and the large fragments within the fractured zone.

Figure F22. Plots of alkalinity, sulfate, ammonium, methane, and calcium in the uppermost 50 mbsf, Site U1379.

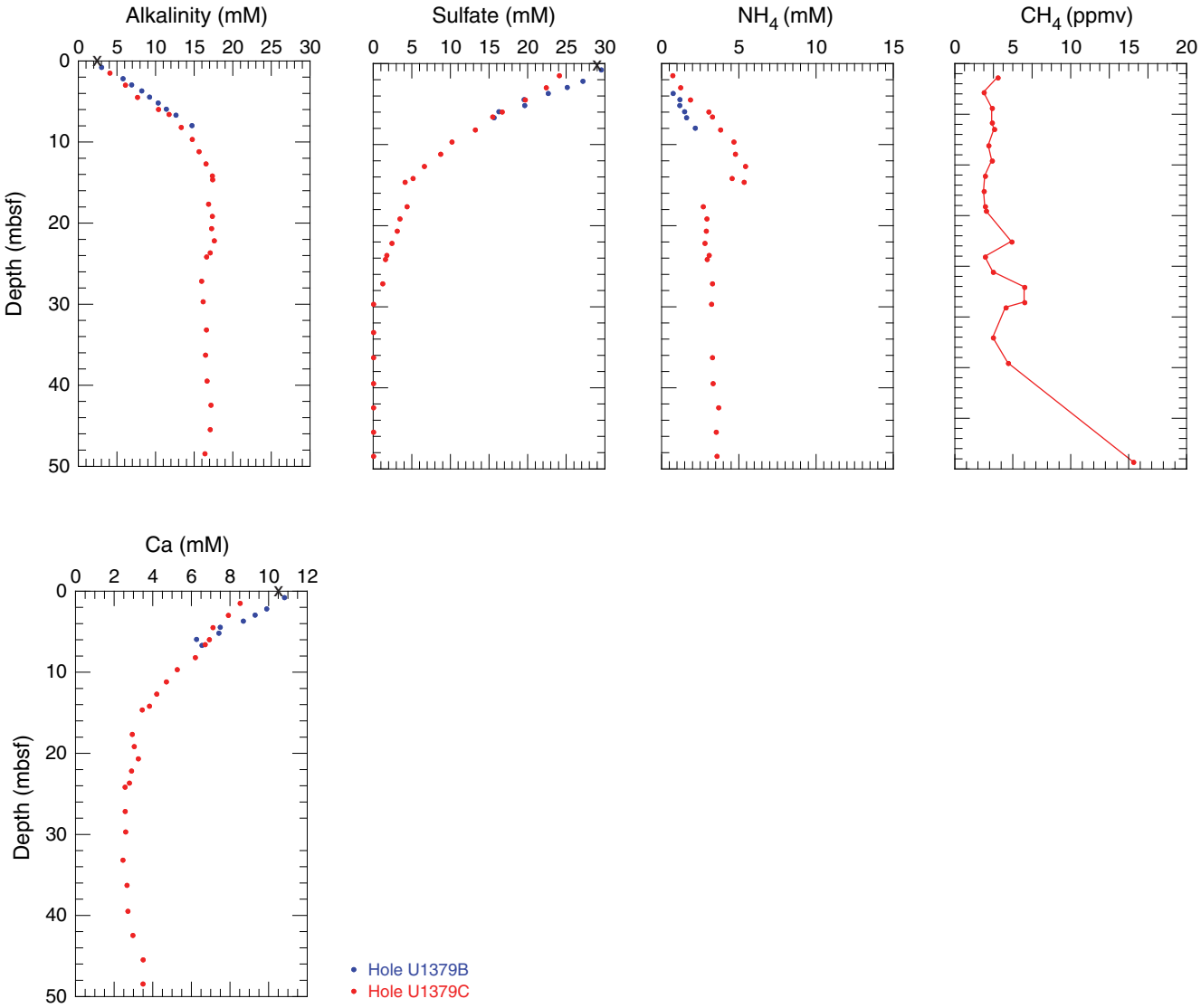

Figure F23. Concentration-depth profiles of salinity, chloride, potassium, ammonium, calcium, magnesium, and Ca/Mg, Site U1379. X = seawater value.

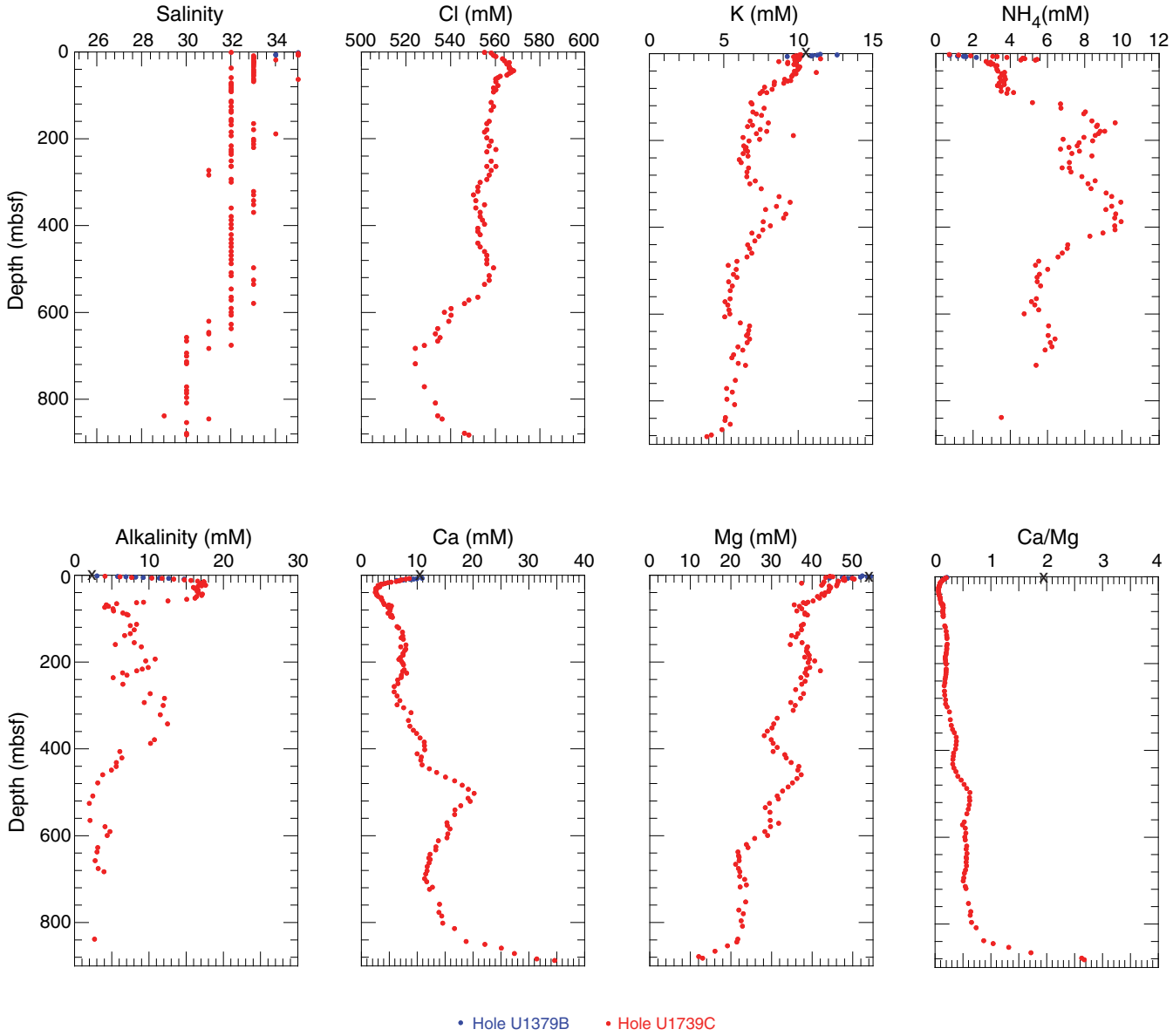

Figure F24. Plot of calcium and magnesium, Site U1379. SW = seawater ratio.

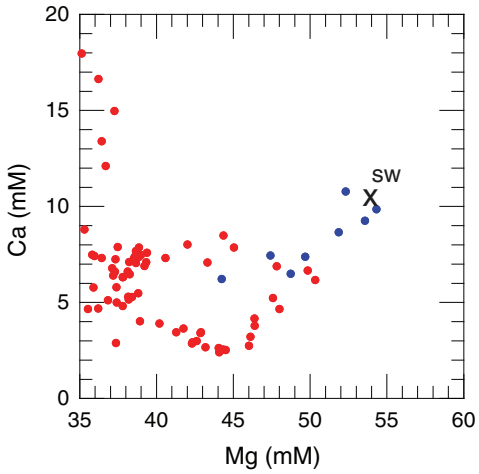

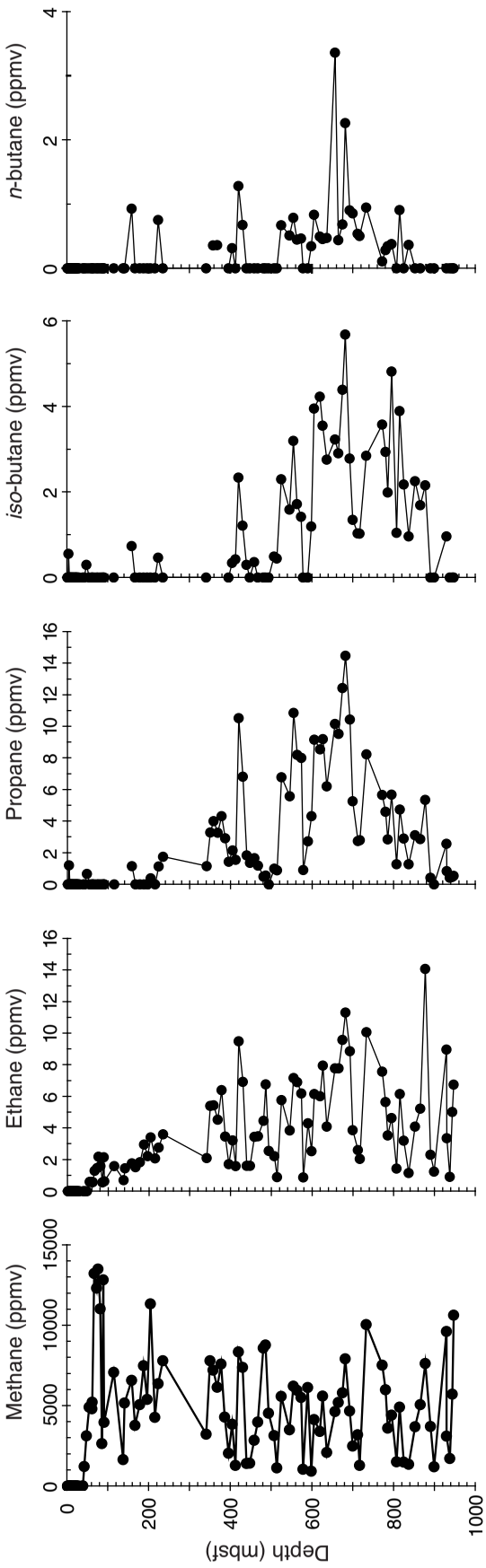

Figure F25. Concentration-depth profiles of C_1 to C_4 hydrocarbons, Site U1379.

Figure F26. Depth profile of $CH_4/(C_2H_6 + C_3H_8)$, Site U1379.

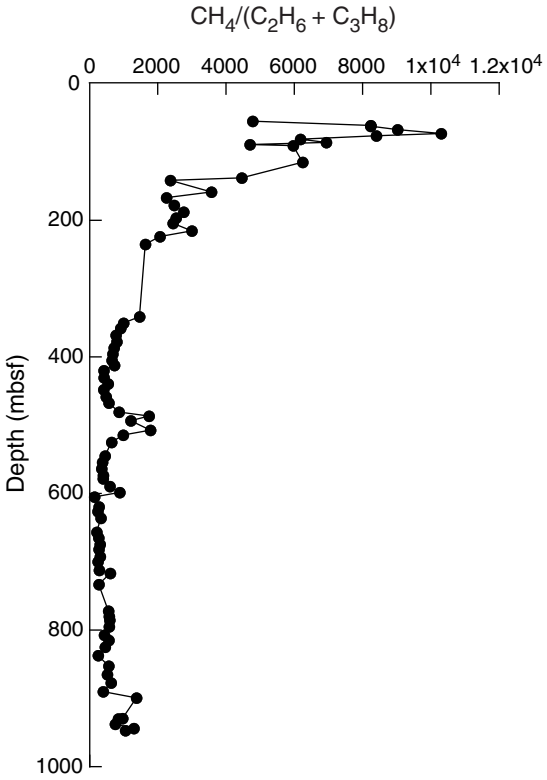

Figure F27. Depth profile of cell concentration in the uppermost 250 mbsf, Site U1379.

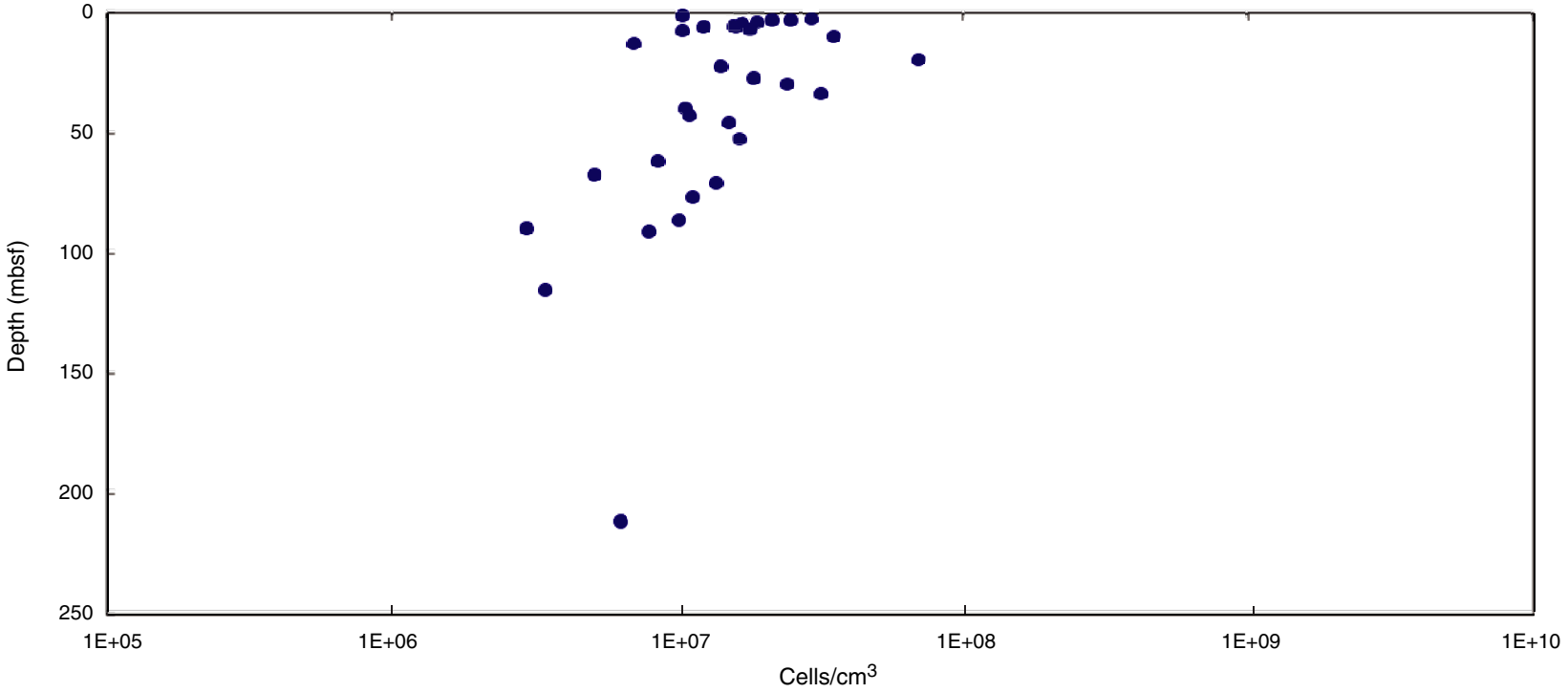

Figure F28. Depth profile of cell concentration in the uppermost 45 mbsf, Site U1379.

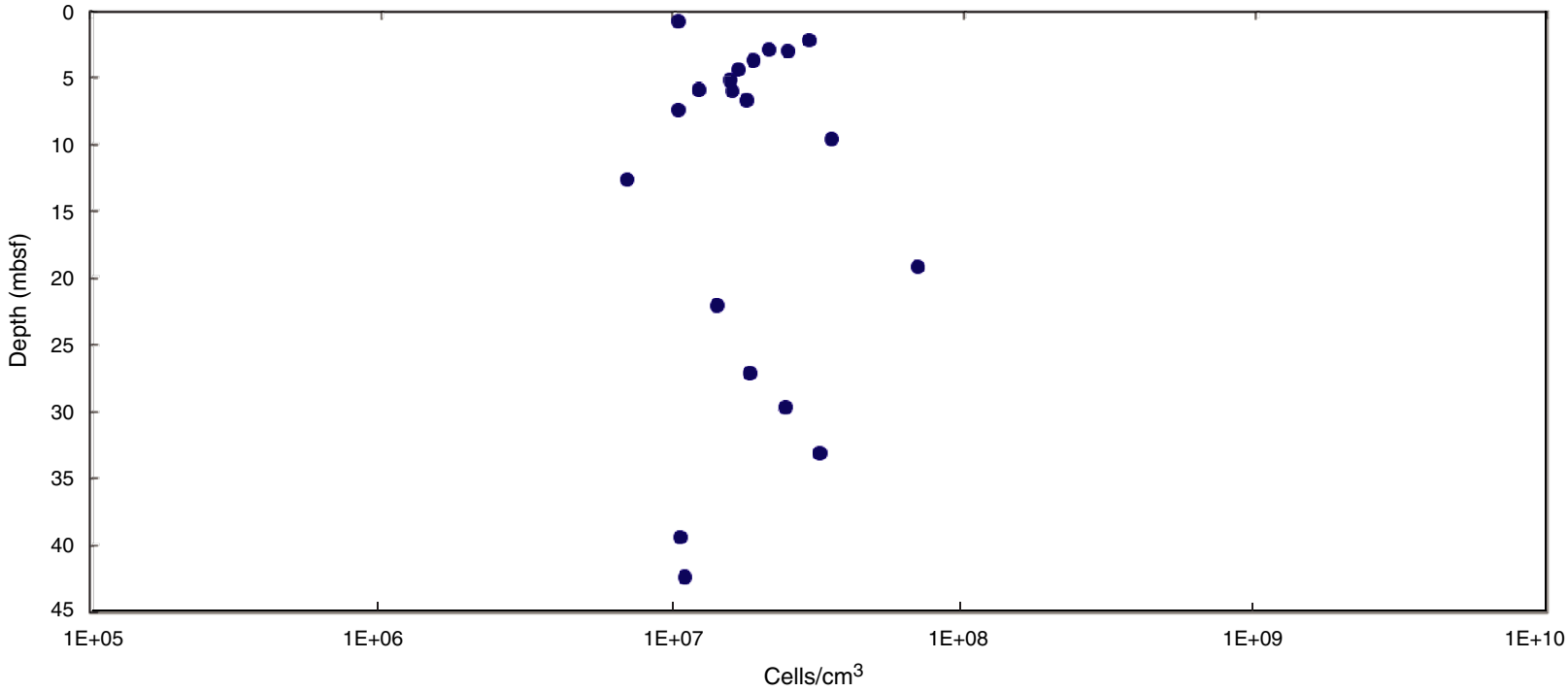

Figure F29. Plots of combined results of density and porosity measurements, Site U1379. **A.** Gamma ray attenuation density measured on the Whole-Round Multisensor Logger (black circles) and wet bulk density measured on discrete samples using the mass/volume method (red circles). **B.** Grain density measured on discrete samples using the moisture and density (MAD) mass/volume method. **C.** Porosity determined using MAD Method C.

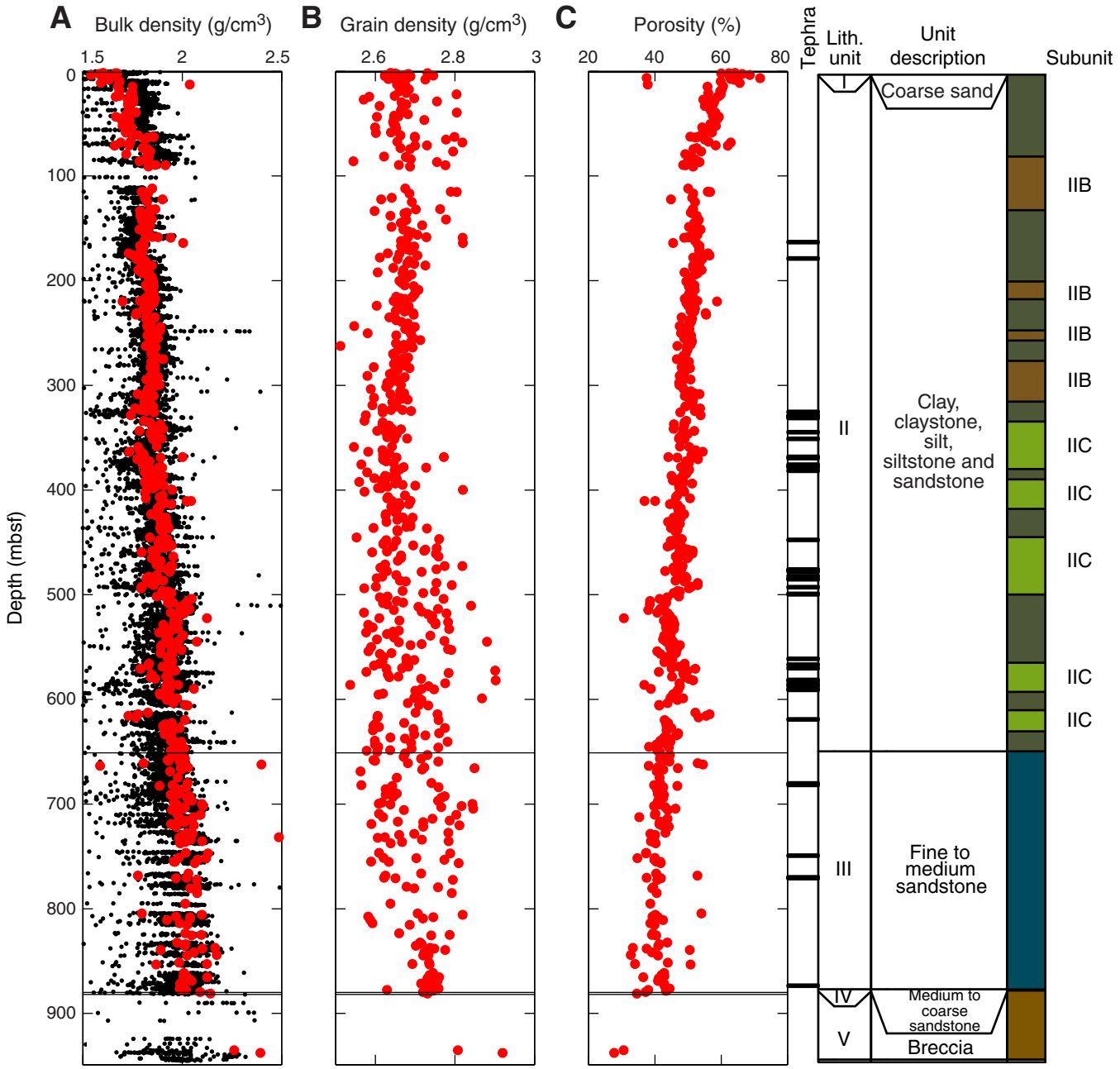

Figure F30. Plots of magnetic susceptibility as a function of depth, Site U1379. Volumetric magnetic susceptibility measurements were made on the Whole-Round Multisensor Logger and point measurements were made on the Section Half Multisensor Logger.

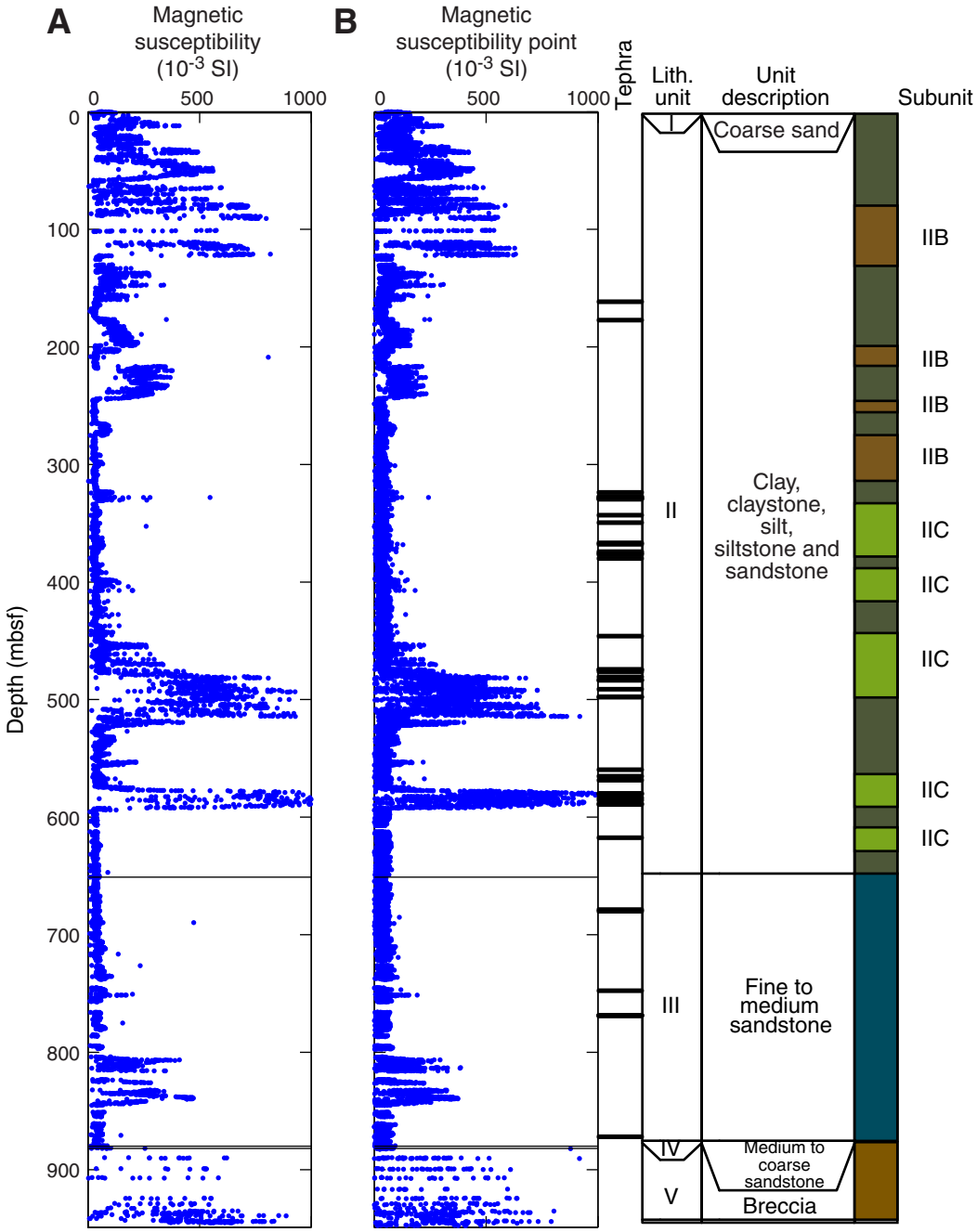

Figure F31. Plot of natural gamma radiation (NGR) as a function of depth, Site U1379.

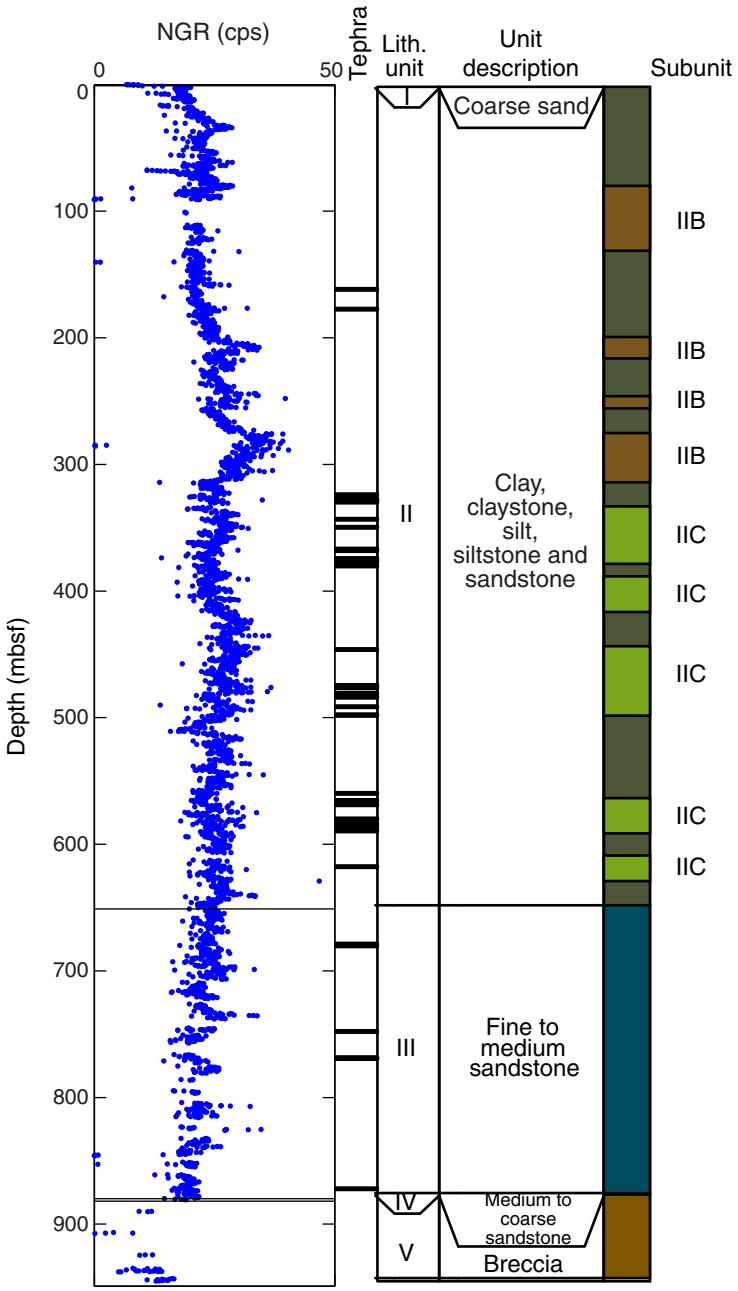

Figure F32. Plot of compressional wave velocity, Site U1379. *P*-wave velocity measured on discrete samples using the Section Half Measurement Gantry. WRMSL = Whole-Round Multisensor Logger.

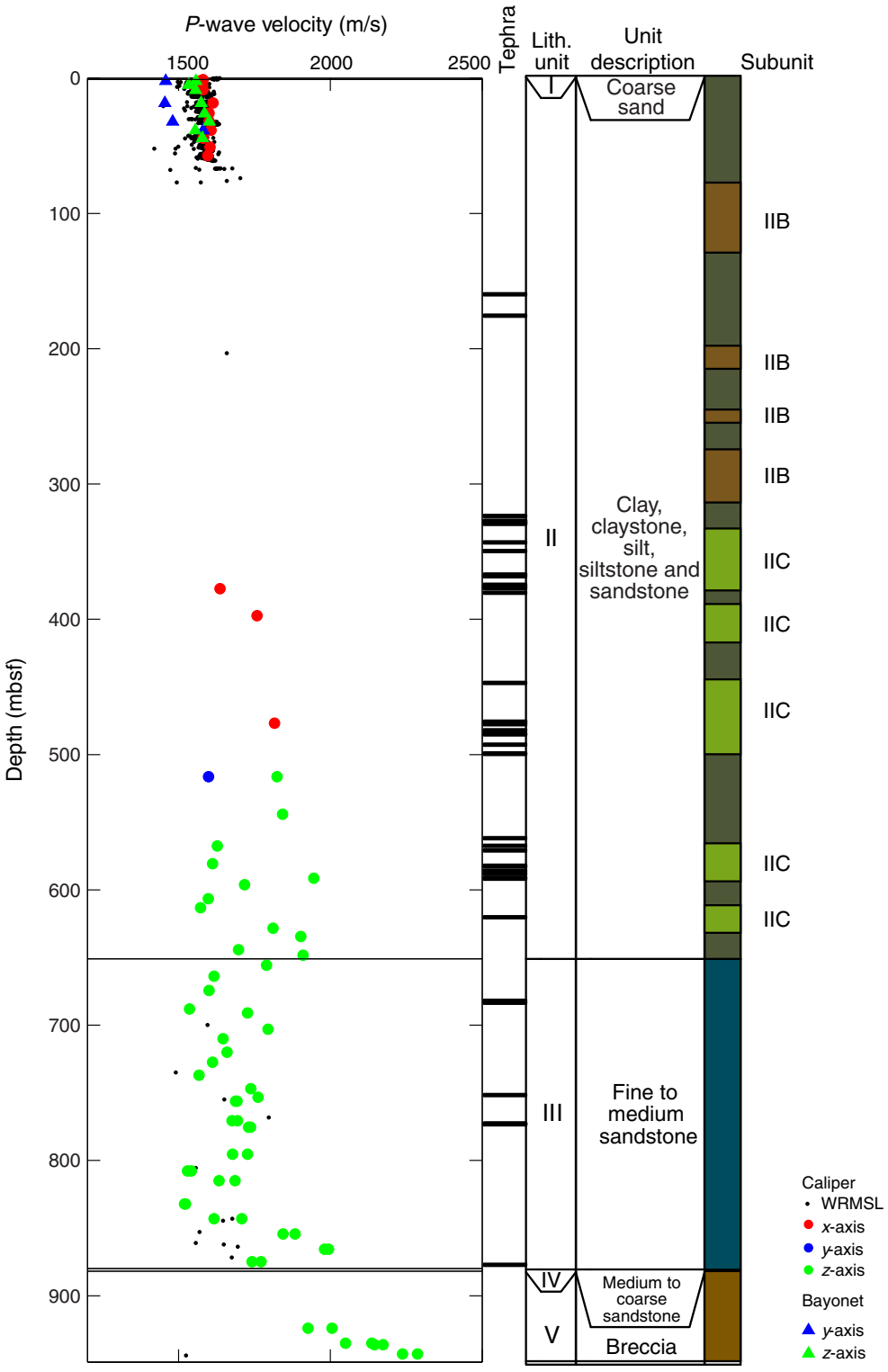

Figure F33. Plots of thermal data, Site U1379. **A.** Thermal conductivity values as a function of depth. **B.** Equilibrium temperatures. Estimated temperature (line) based on linear fit to thermal conductivity and thermal gradient.

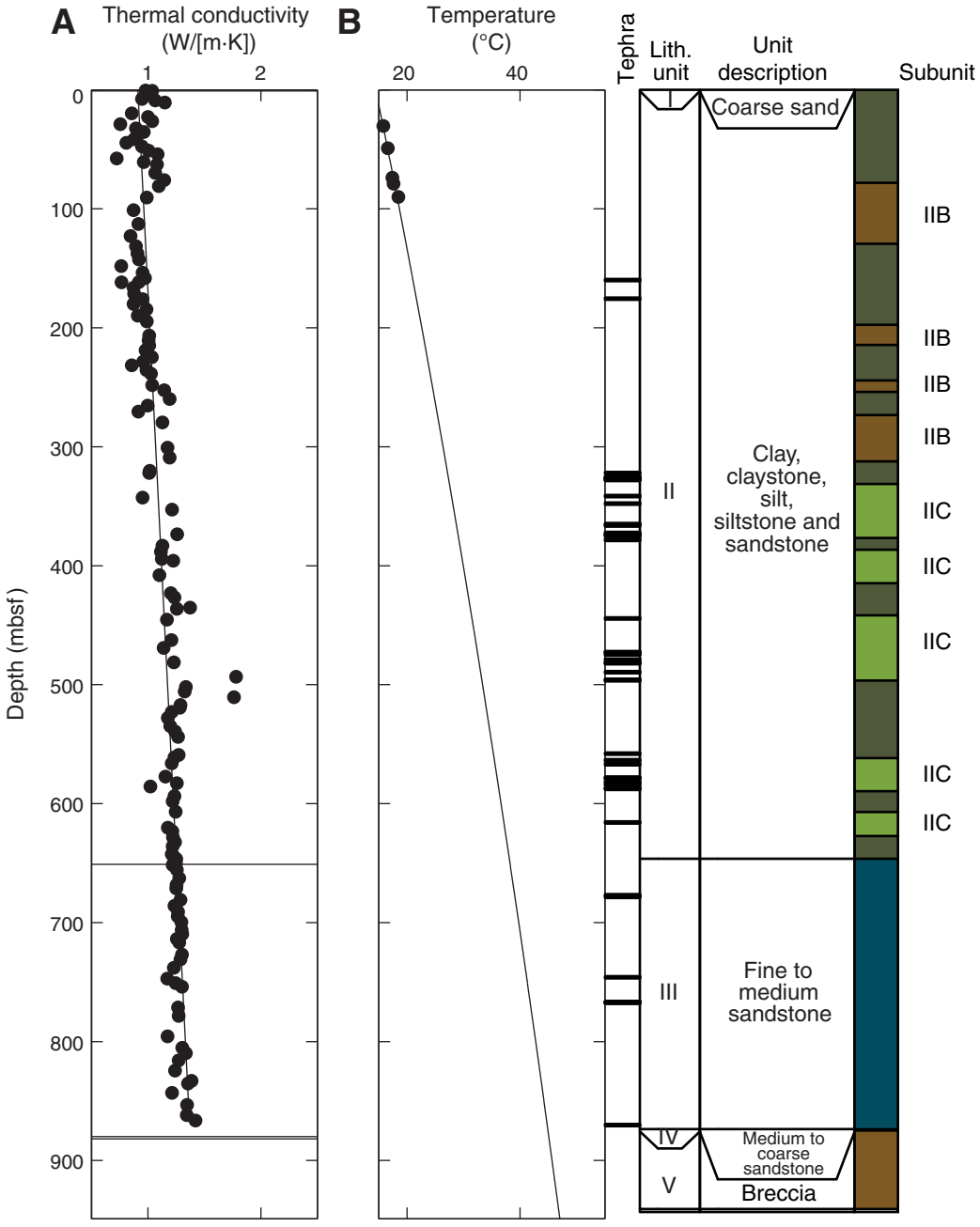

Figure F34. Plots of temperature-time series measured during the deployment of the advanced piston corer temperature tool (APCT-3), Site U1379. Unshaded area indicates data used for equilibrium temperature fit. Triangle indicates beginning of fit and inverted triangle indicates end of fit. (Continued on next page.)

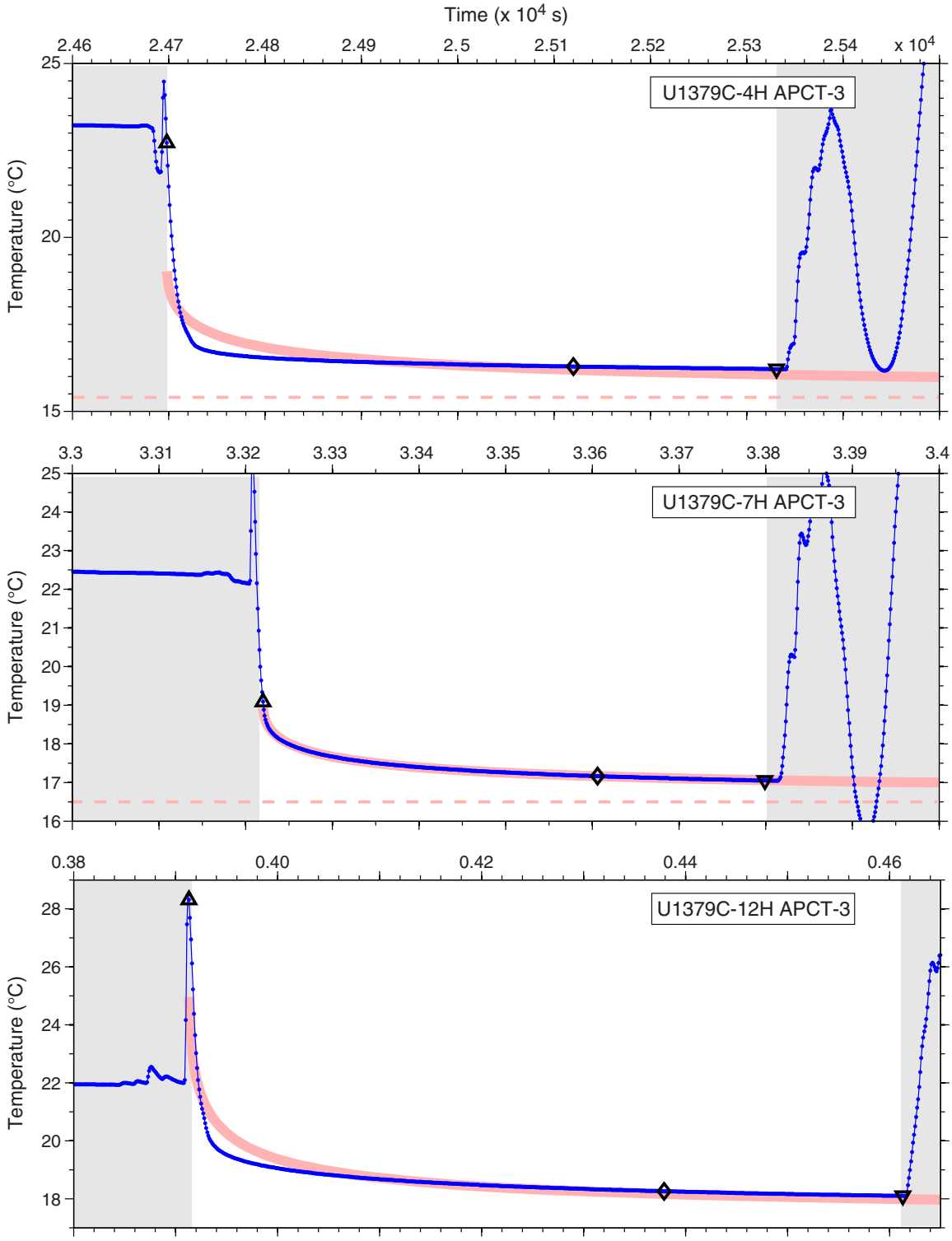

Figure F34 (continued).

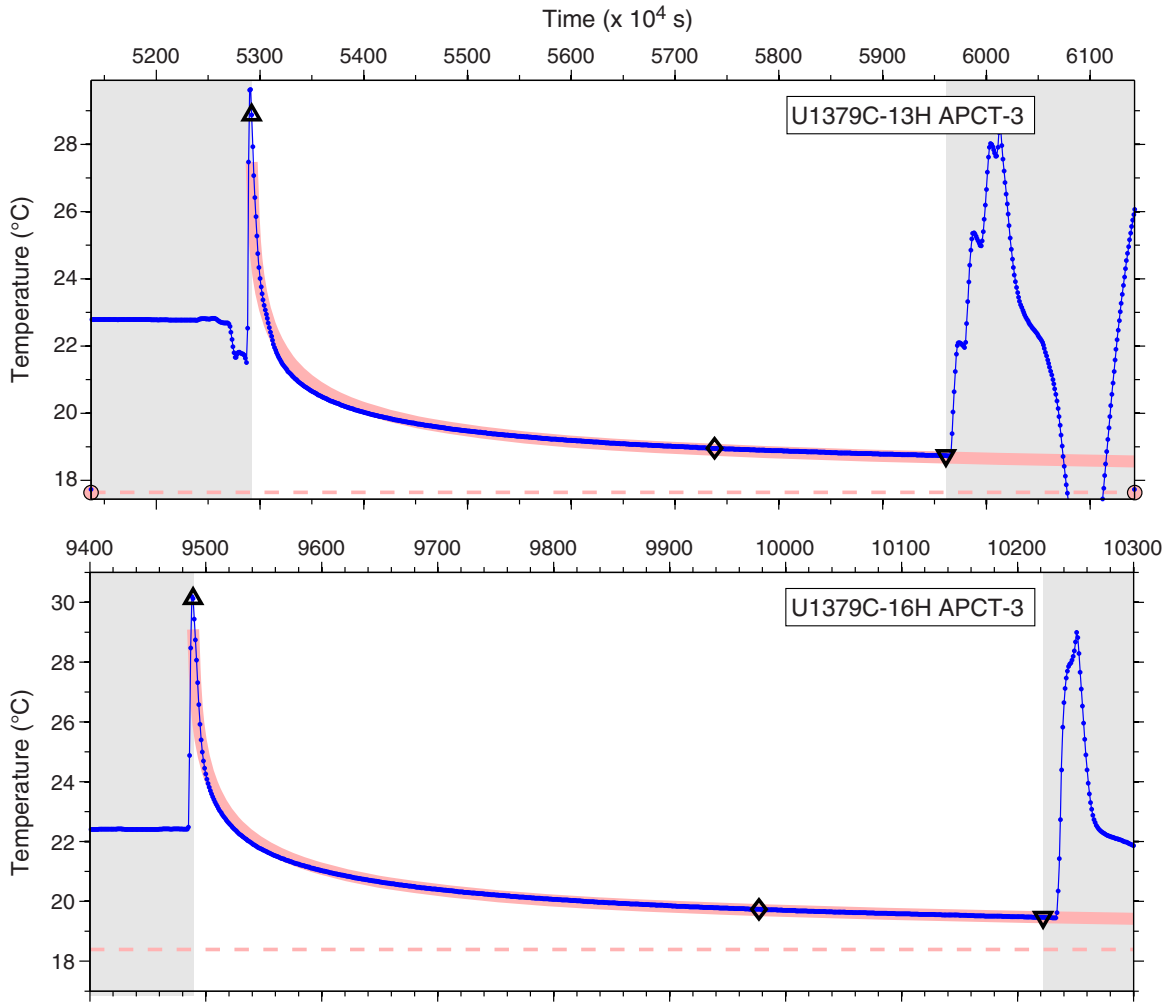

Figure F35. Plot of undrained shear strength measured using an automatic vane shear, Site U1379.

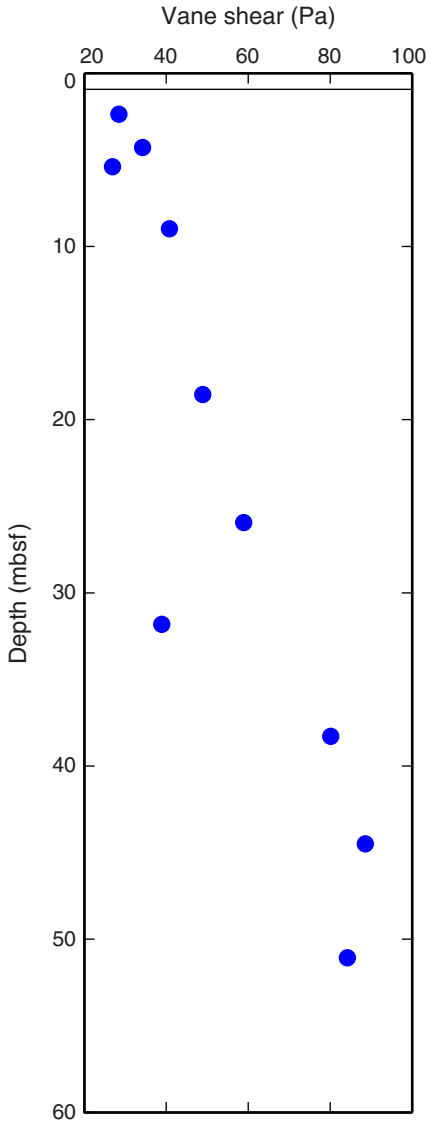

Figure F36. Plots of L*, a*, and b* reflectance values vs. depth, Site U1379.

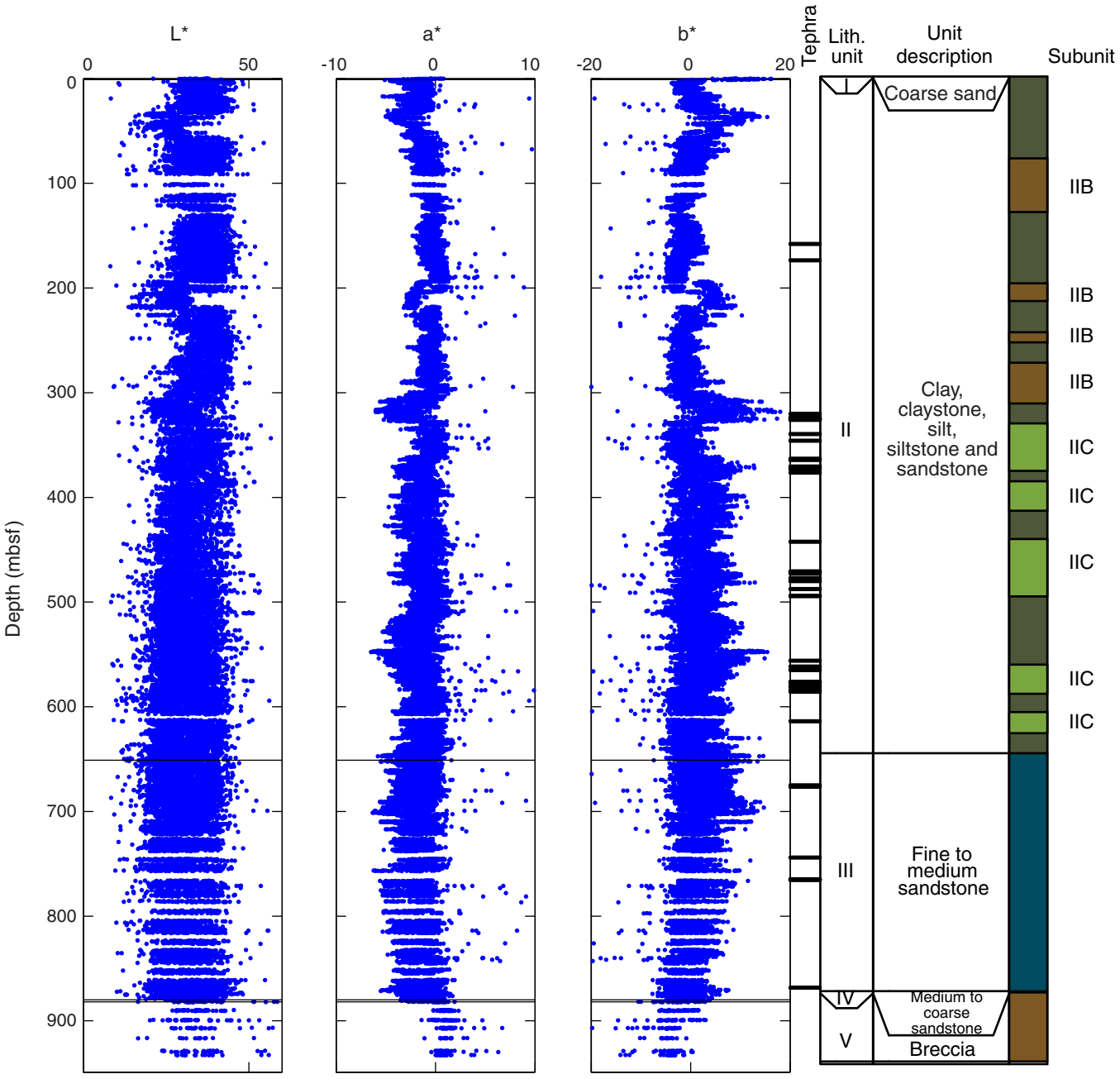

Figure F37. Plots of paleomagnetic measurements on archive sections of (**A**) natural remanent magnetization and (**B**) after 30 mT AF demagnetization, Hole U1379C. Red stars indicate characteristic remanent magnetization of discrete samples.

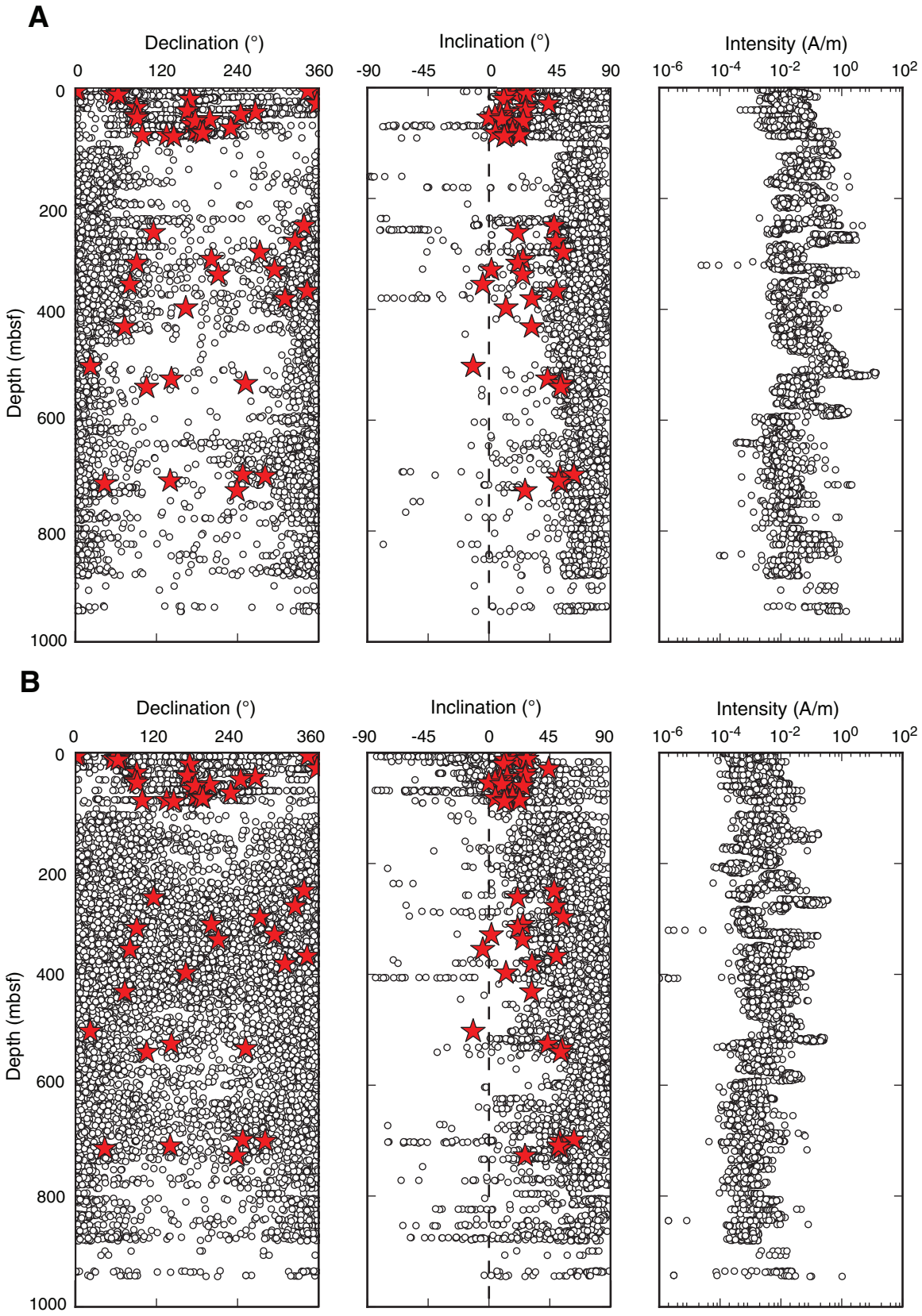

Figure F38. Plot of declination variations of paleomagnetic measurements on archive sections after 30 mT AF demagnetization for APC cores, Hole U1379C. Red stars indicate characteristic remanent magnetization of discrete samples, and dashed red horizontal lines represent core boundaries.

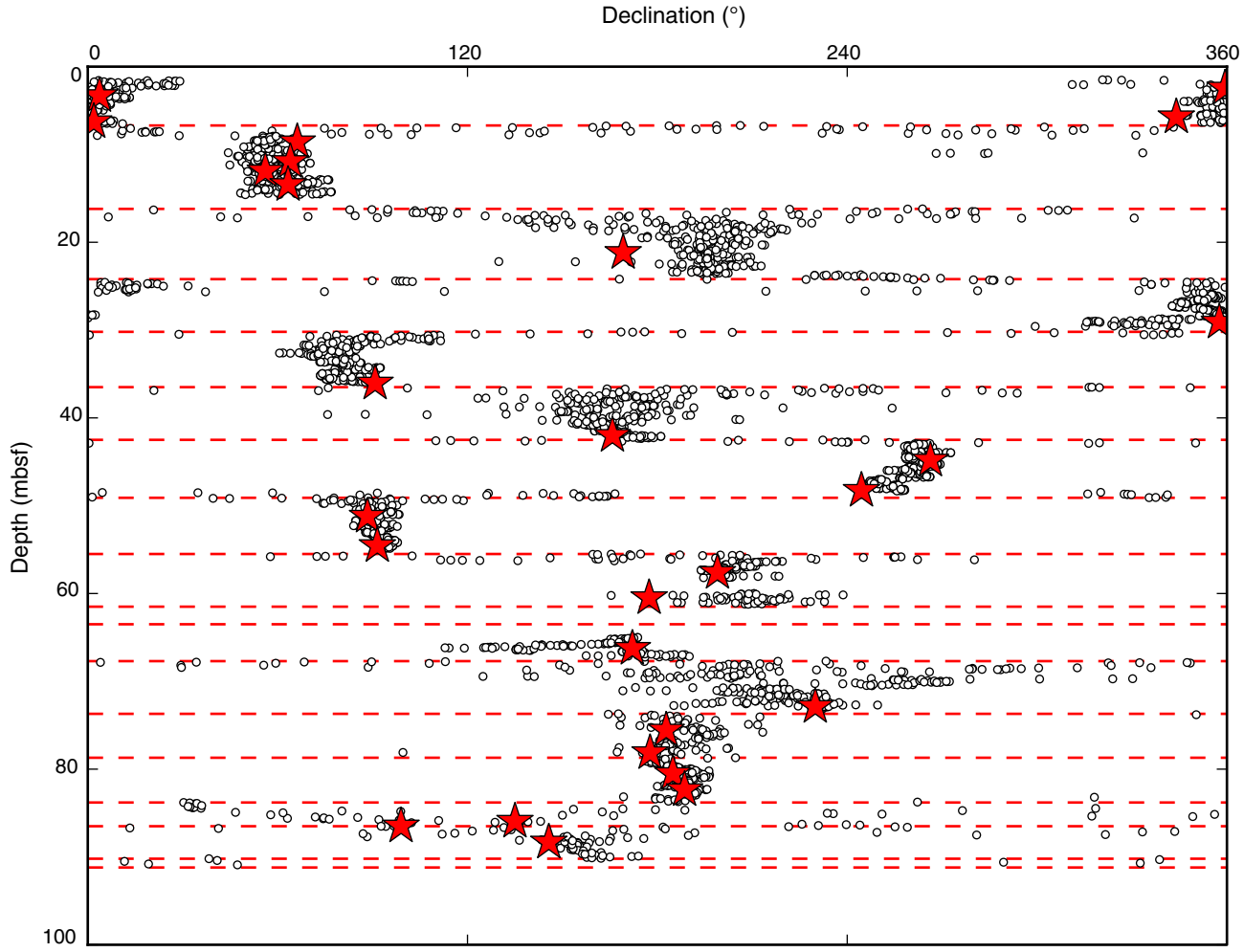

Figure F39. Representative vector endpoint diagrams (Zijderveld, 1967) of magnetization directions through stepwise AF demagnetization for (**A**) sample from an APC core, (**B**) sample from an XCB core with well-defined characteristic remanent magnetization, and (**C**) sample from an XCB core with strong drilling overprint. Open squares and solid circles represent the projection of the magnetization vector endpoints onto the vertical and horizontal planes, respectively. NRM = natural remanent magnetization.

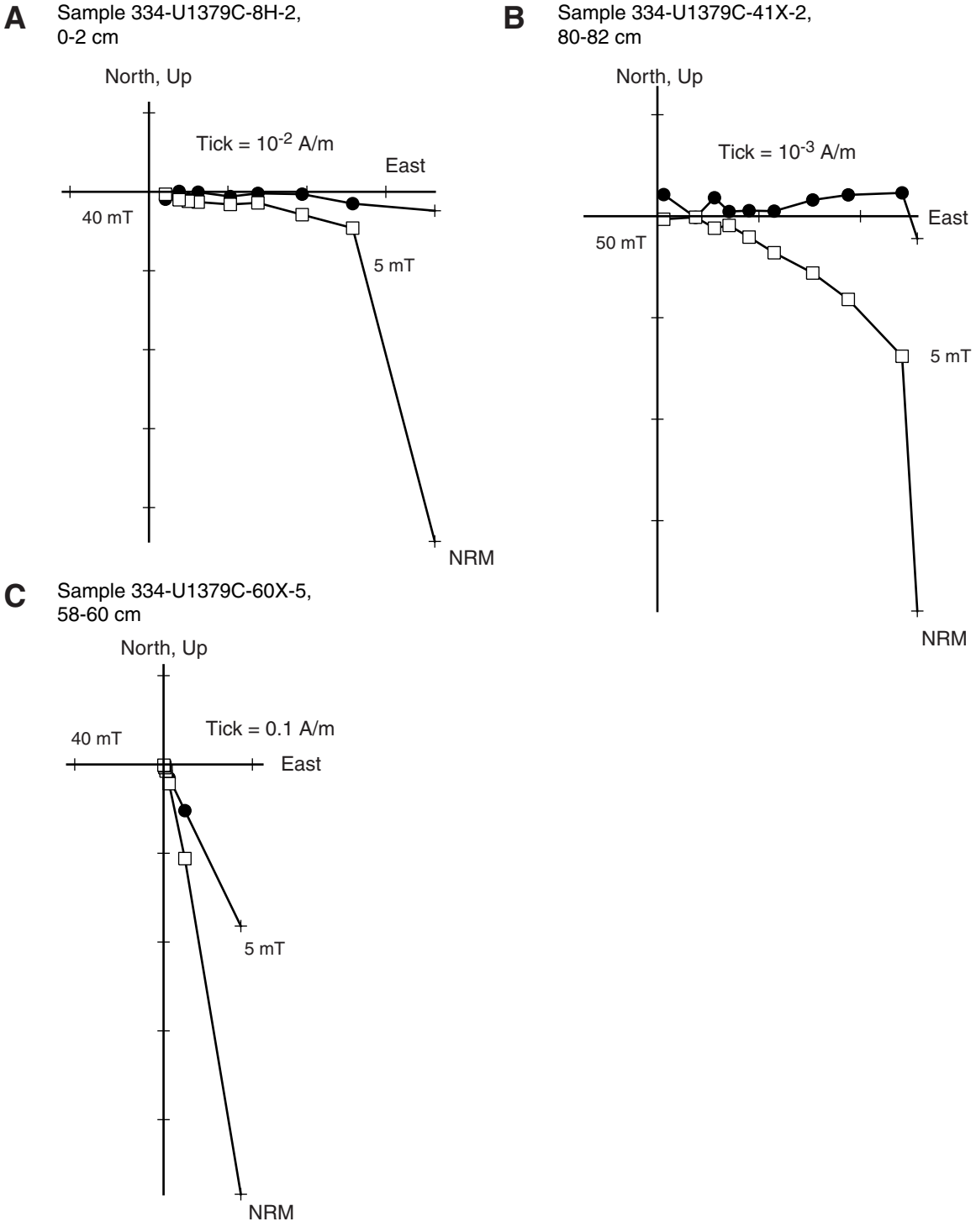

Figure F40. Histograms of declination and inclination for discrete samples from XCB cores in Hole U1379C showing the effects of radial overprint. AF demagnetization is capable of removing both the radial and vertical overprints, as shown by the distribution of declination (more random in **C** than in **A**) and inclination (more significant in **D** than in **B**). NRM = natural remanent magnetization, ChRM = characteristic remanent magnetization.

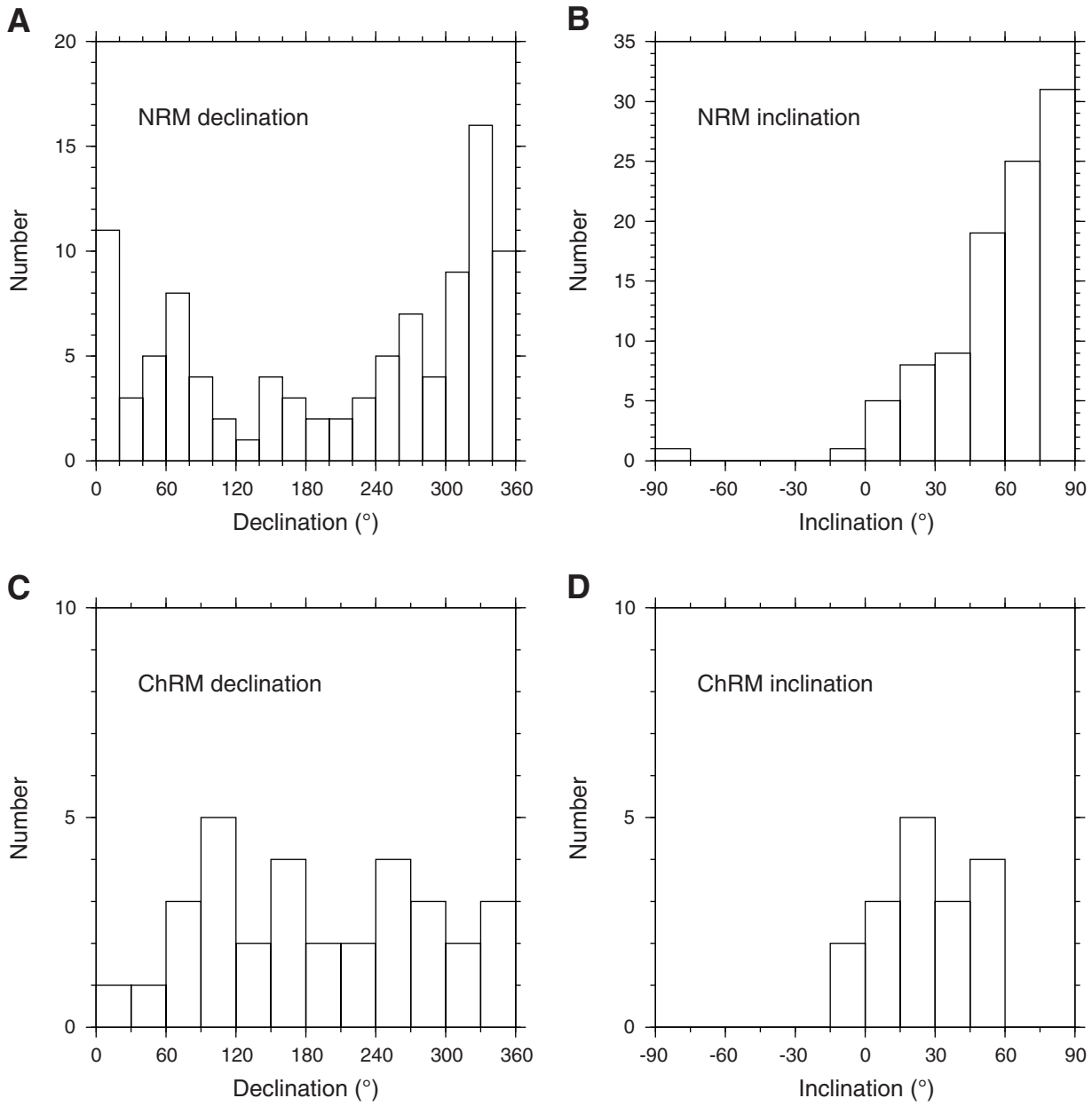

Figure F41. Monitoring and quality control LWD logs, Hole U1379A. D = hole diameter from density measurements, U = hole diameter from ultrasonic measurements, ROP = rate of penetration.

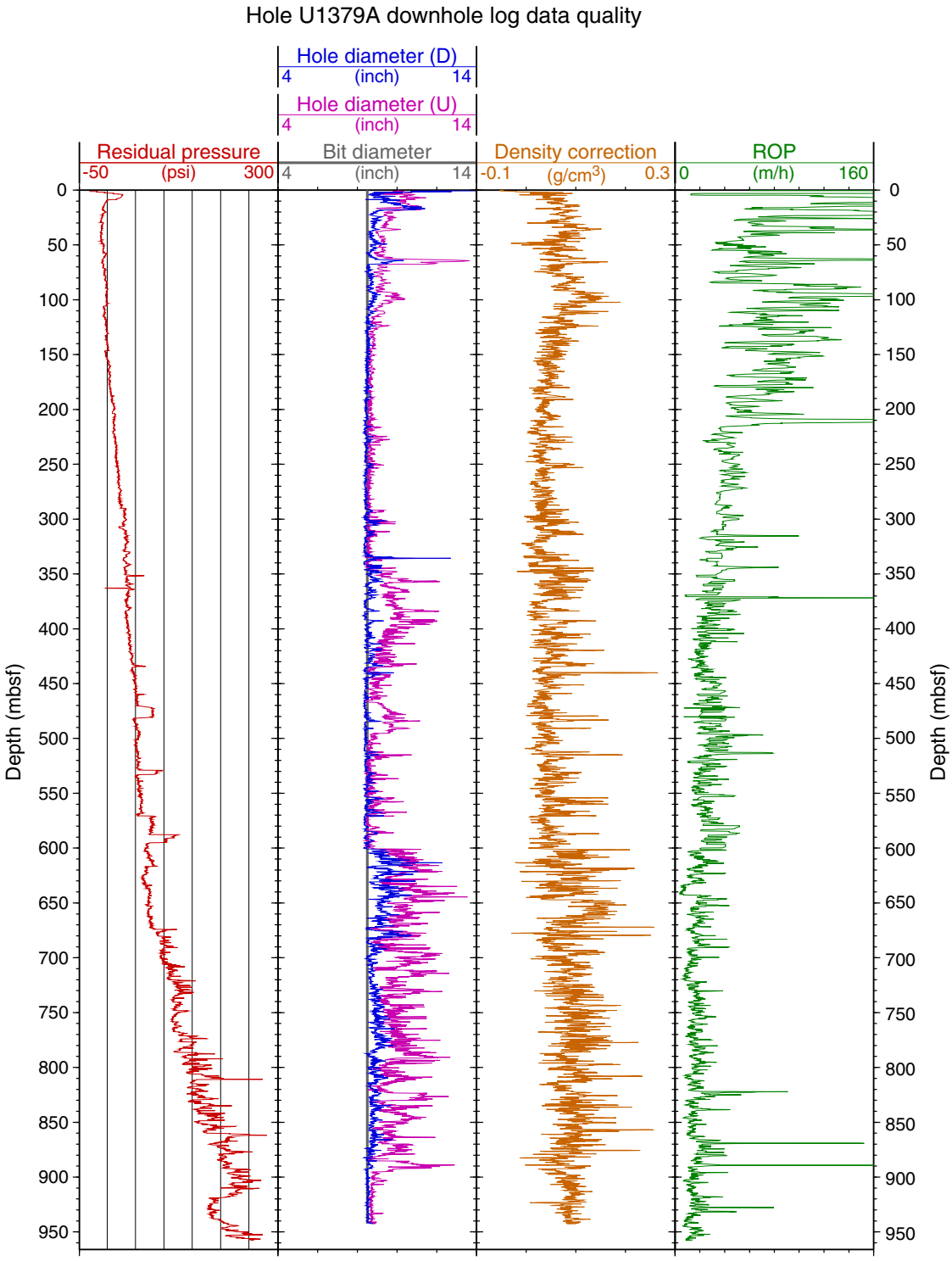

Figure F42. Summary of LWD measurements, Hole U1379A. ARC = arcVISION tool, PEF = photoelectric factor, IDRO = image-derived density, RHOB = bulk density, P16B = phase-shift resistivity measured at a 16 inch source–receiver separation, A40B = attenuation resistivity measured at a 40 inch source–receiver separation.

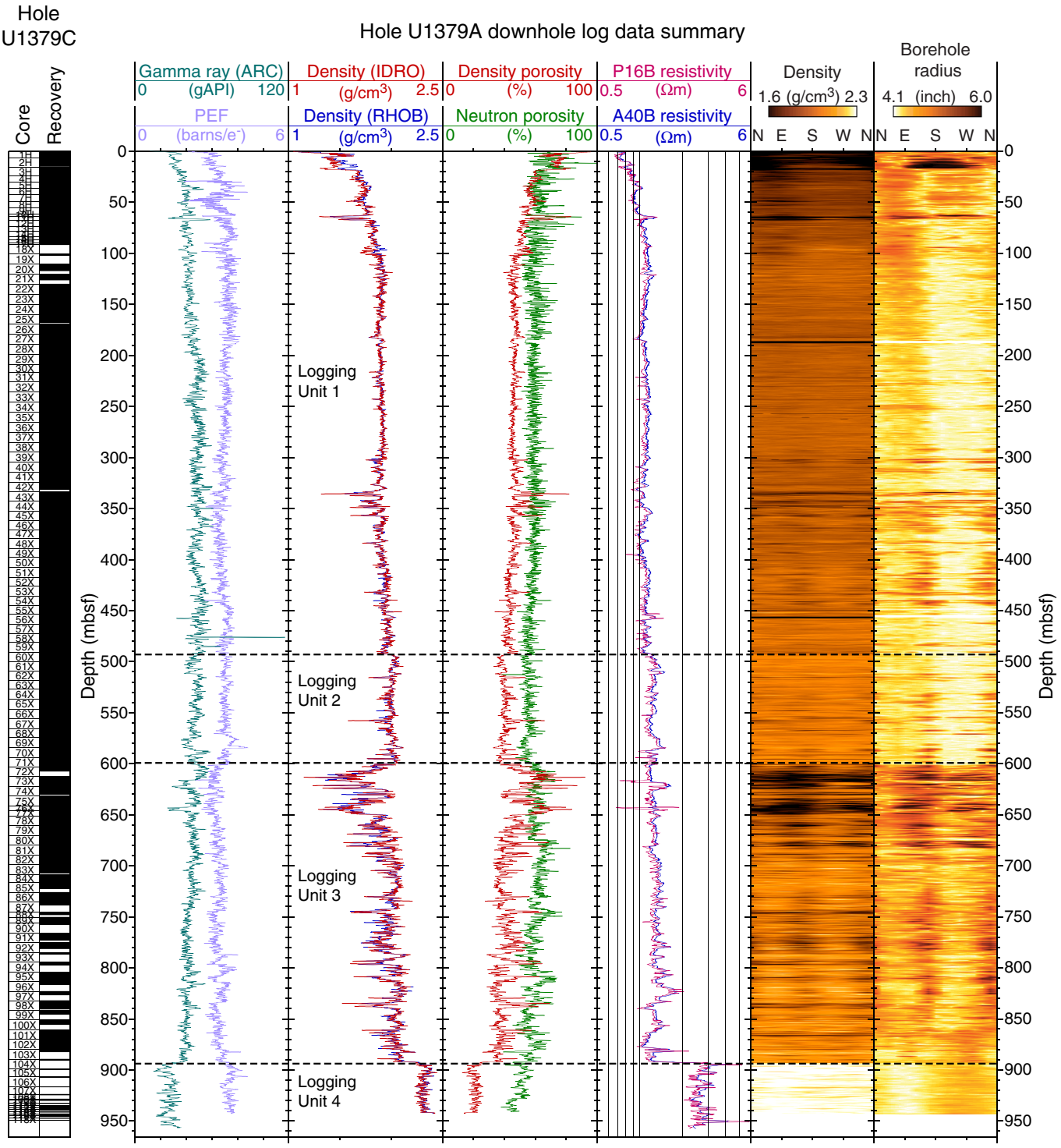

Figure F43. Example borehole radius images of distinct narrow breakouts observed in Hole U1379A.

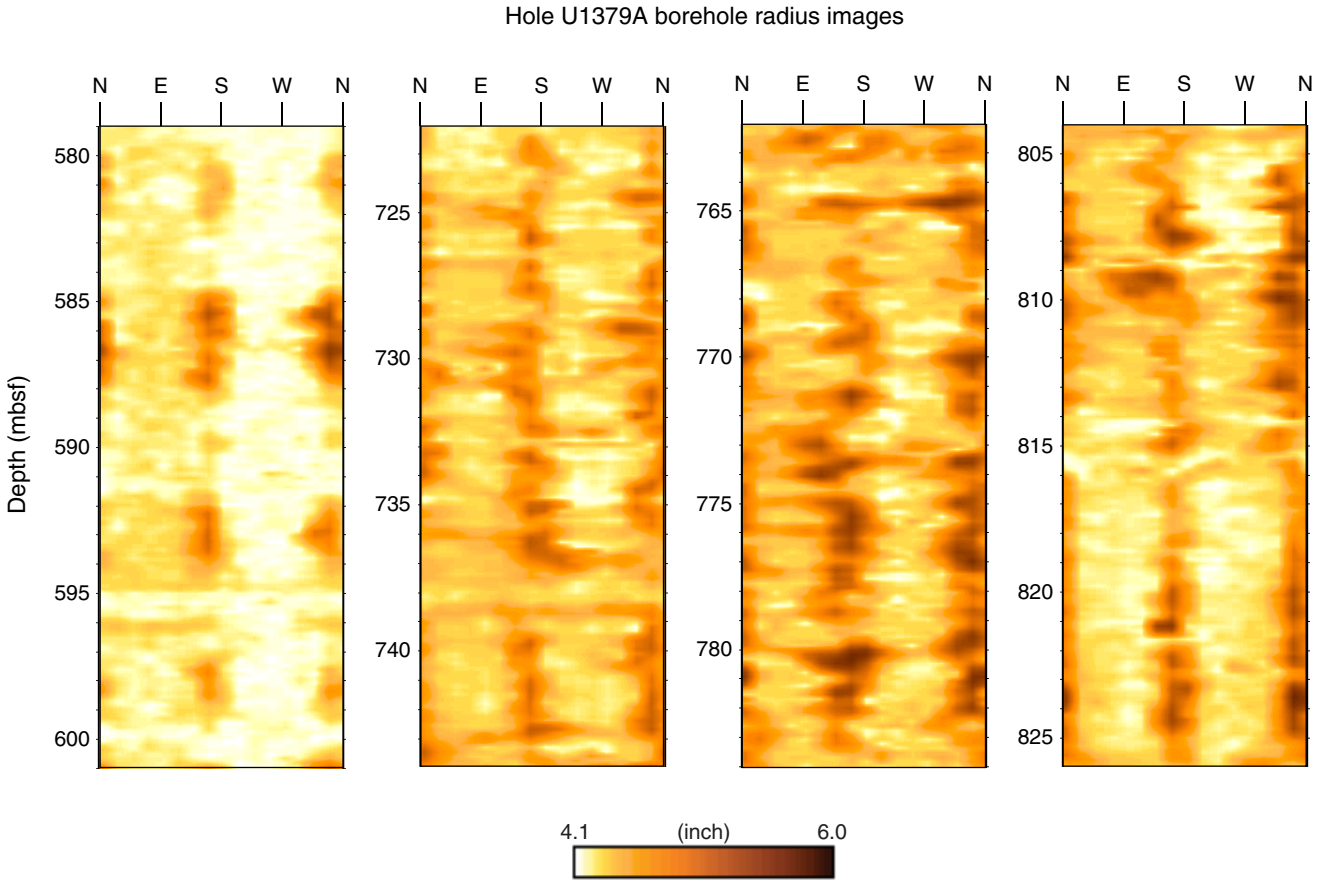

Figure F44. Comparison of LWD log data in Hole U1379A (colored curves) and core measurements in Hole U1379C (black circles). ARC = arcVISION tool, NGR = natural gamma ray core measurement, IDRO = image-derived density (adnVISION tool), GRA = gamma ray attenuation core measurement, MAD = moisture and density core measurement.

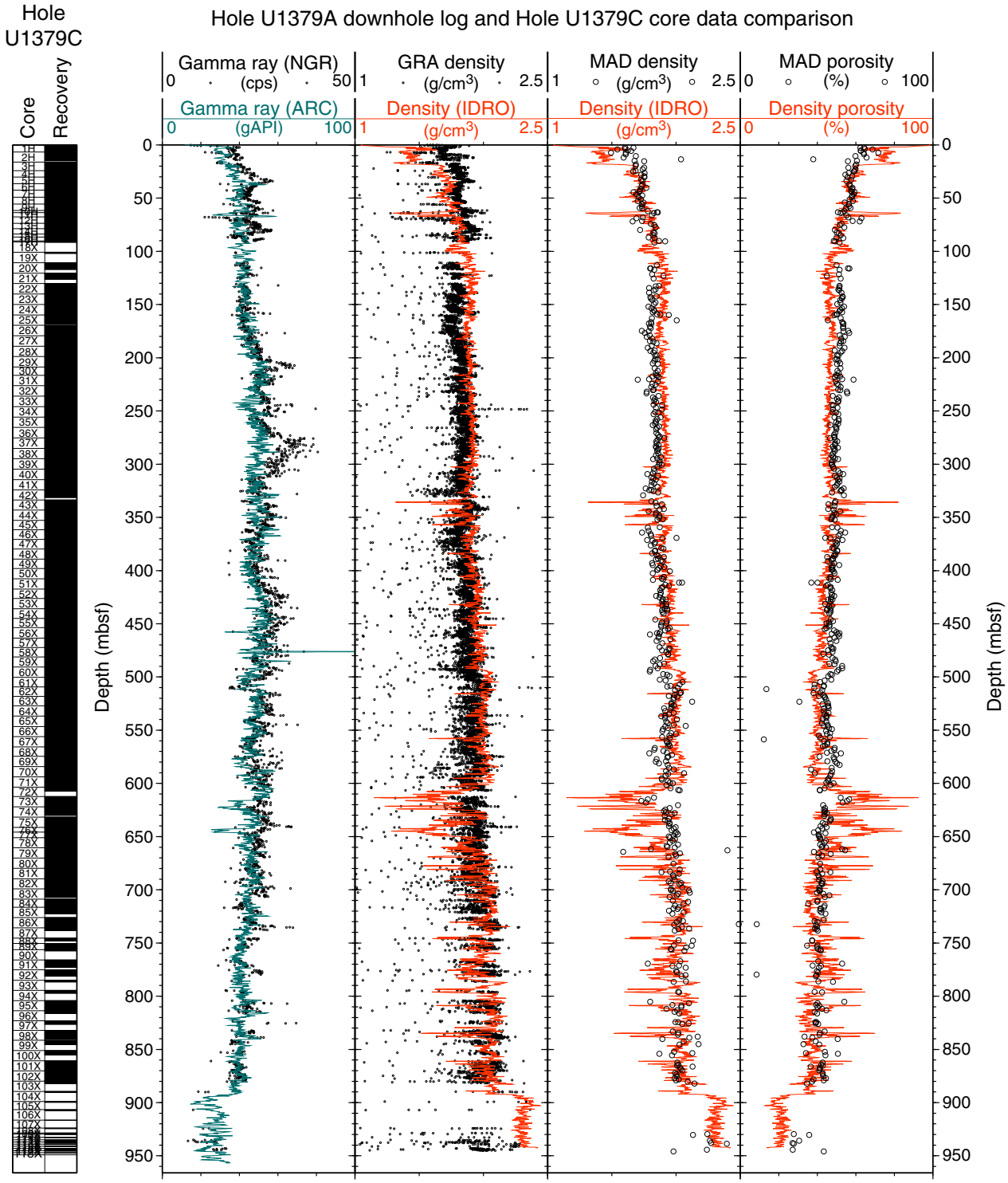

Figure F45. Comparison of LWD log data in Hole U1379A (colored curves) and core measurements in Hole U1379C (black curves and circles). D = hole diameter from density measurements, U = hole diameter from ultrasonic measurements, ARC = arcVISION tool, NGR = natural gamma ray core measurement, MAD = moisture and density core measurement, IDRO = image-derived density (adnVISION tool), P16B = phase-shift resistivity measured at a 16 inch source–receiver separation, A40B = attenuation resistivity measured at a 40 inch source–receiver separation. Orange circles indicate low density peaks in the logs that are most likely due to matching borehole enlargements. Blue shaded intervals highlight low logged densities that correspond to low resistivities.

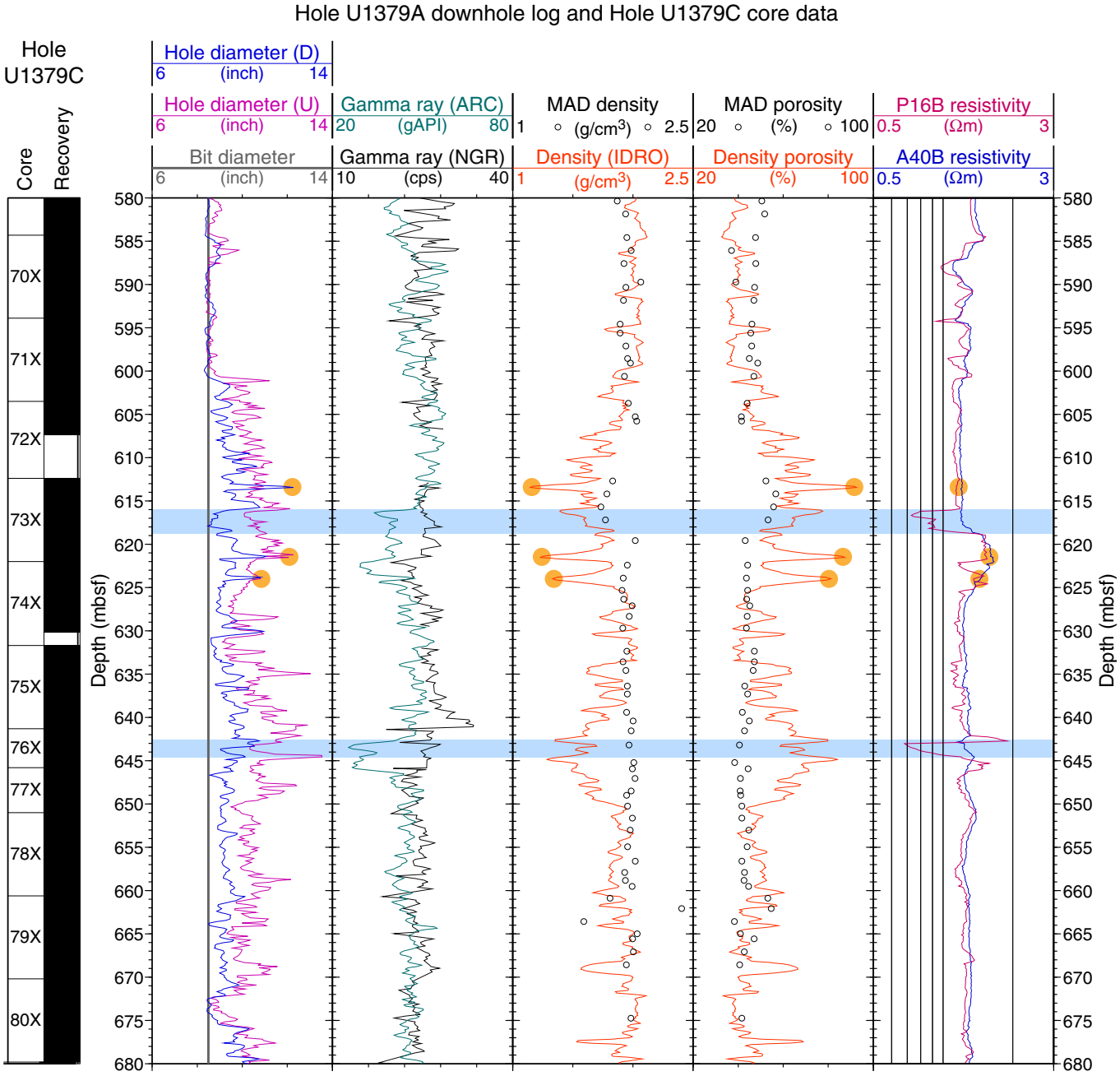

Table T1. Operations summary, Site U1379. (Continued on next two pages.)

Hole U1379A
Latitude: 8°40.8501′N
Longitude: 84°02.0166′W
Time on hole (h): 91.2 (0345 h, 20 March–2300 h, 23 March 2011)
Seafloor (drill pipe measurement below rig floor, m DRF): 137.0
Distance between rig floor and sea level (m): 11.1
Water depth (drill pipe measurement from sea level, mbsl): 125.9
Total penetration (drilling depth below seafloor, m DSF): 962.8
Total length of cored interval (m): 0
Total core recovered (m): 0
Recovery (%): 0
Drilled interval (m): 962.8
Total number of cores: 0

Hole U1379B
Latitude: 8°40.8502′N
Longitude: 84°02.0277′W
Time on hole (h): 5.0 (0530–1030 h, 25 March 2011)
Seafloor (drill pipe measurement below rig floor, m DRF): 138.5
Distance between rig floor and sea level (m): 11.1
Water depth (drill pipe measurement from sea level, mbsl): 127.4
Total penetration (drilling depth below seafloor, m DSF): 10.5
Total length of cored interval (m): 10.5
Total core recovered (m): 8.72
Recovery (%): 83
Drilled interval (m): 0
Total number of cores: 2

Hole U1379C
Latitude: 8°40.8605′N
Longitude: 84°02.0274′W
Time on hole (h): 191.3 (1030 h, 25 March–0945 h, 2 April 2011)
Seafloor (drill pipe measurement below rig floor, m DRF): 138.8
Distance between rig floor and sea level (m): 11.1
Water depth (drill pipe measurement from sea level, mbsl): 127.7
Total penetration (drilling depth below seafloor, m DSF): 949.0
Total length of cored interval (m): 949.0
Total core recovered (m): 815.6
Recovery (%): 86
Drilled interval (m): 0
Total number of cores: 118

Core	Date (2011)	Time (h)	Depth DSF (m) Top of cored interval	Depth DSF (m) Bottom of cored interval	Interval advanced (m)	Depth CSF (m) Top of cored interval	Depth CSF (m) Bottom of cored interval	Length of core recovered (m)	Recovery (%)
334-U1379A-									
11	23 Mar	0500			*****Drilled from 0.0 to 962.8 m DSF*****				
334-U1379B-									
1H	25 Mar	1555	0.0	1.0	1.0	0.0	0.9	0.93	93
2H	25 Mar	1730	1.0	10.5	9.5	1.0	8.8	7.79	82
334-U1379C-									
1H	25 Mar	1915	0.0	6.7	6.7	0.0	6.7	6.68	100
2H	25 Mar	2005	6.7	16.2	9.5	6.7	15.0	8.27	87
3H	25 Mar	2055	16.2	24.2	8.0	16.2	24.5	8.30	104
4H	25 Mar	2155	24.2	30.2	6.0	24.2	30.2	6.02	100
5H	25 Mar	2235	30.2	36.5	6.3	30.2	36.6	6.41	102
6H	25 Mar	2320	36.5	42.5	6.0	36.5	43.8	7.26	121
7H	26 Mar	0035	42.5	49.1	6.6	42.5	49.1	6.58	100
8H	26 Mar	0110	49.1	55.5	6.4	49.1	55.4	6.30	98
9H	26 Mar	0155	55.5	61.5	6.0	55.5	61.6	6.05	101
10H	26 Mar	0255	61.5	63.5	2.0	61.5	63.6	2.05	103
11H	26 Mar	0345	63.5	67.7	4.2	63.5	67.7	4.20	100
12H	26 Mar	0445	67.7	73.7	6.0	67.7	73.8	6.06	101
13H	26 Mar	0555	73.7	78.7	5.0	73.7	78.8	5.12	102
14H	31 Mar	0735	78.7	83.8	5.1	78.7	83.8	5.11	100
15H	30 Mar	0830	83.8	86.5	2.7	83.8	86.7	2.85	106
16H	30 Mar	0950	86.5	90.2	3.7	86.5	90.2	3.72	101
17H	30 Mar	1035	90.2	91.2	1.0	90.2	91.1	0.94	94

Table T1 (continued). (Continued on next page.)

Core	Date (2011)	Time (h)	Depth DSF (m) Top of cored interval	Depth DSF (m) Bottom of cored interval	Interval advanced (m)	Depth CSF (m) Top of cored interval	Depth CSF (m) Bottom of cored interval	Length of core recovered (m)	Recovery (%)
18X	30 Mar	1305	91.2	100.9	9.7	91.2	91.6	0.37	4
19X	30 Mar	1345	100.9	110.7	9.8	100.9	102.0	1.12	11
20X	30 Mar	1430	110.7	120.5	9.8	110.7	117.2	6.46	66
21X	30 Mar	1515	120.5	130.3	9.8	120.5	126.1	5.64	58
22X	30 Mar	1615	130.3	140.1	9.8	130.3	140.3	10.01	102
23X	30 Mar	1715	140.1	149.9	9.8	140.1	149.8	9.68	99
24X	30 Mar	1825	149.9	159.7	9.8	149.9	159.8	9.89	101
25X	30 Mar	1930	159.7	169.5	9.8	159.7	168.1	8.38	86
26X	26 Mar	2025	169.5	179.3	9.8	169.5	179.3	9.75	99
27X	26 Mar	2135	179.3	189.1	9.8	179.3	189.2	9.88	101
28X	26 Mar	2240	189.1	198.9	9.8	189.1	199.4	10.32	105
29X	27 Mar	0035	198.9	208.7	9.8	198.9	208.8	9.89	101
30X	27 Mar	0155	208.7	216.5	7.8	208.7	218.6	9.87	127
31X	27 Mar	0325	216.5	226.3	9.8	216.5	226.5	9.99	102
32X	27 Mar	0455	226.3	236.1	9.8	226.3	236.3	9.96	102
33X	27 Mar	0645	236.1	245.9	9.8	236.1	246.0	9.89	101
34X	27 Mar	0820	245.9	255.7	9.8	245.9	255.8	9.89	101
35X	27 Mar	0940	255.7	265.5	9.8	255.7	265.6	9.92	101
36X	27 Mar	1050	265.5	275.3	9.8	265.5	275.6	10.05	103
37X	27 Mar	1200	275.3	285.1	9.8	275.3	285.3	10.01	102
38X	27 Mar	1300	285.1	294.9	9.8	285.1	295.2	10.05	103
39X	27 Mar	1430	294.9	304.7	9.8	294.9	304.1	9.17	94
40X	27 Mar	1535	304.7	314.5	9.8	304.7	314.4	9.74	99
41X	27 Mar	1655	314.5	324.2	9.7	314.5	324.4	9.91	102
42X	27 Mar	1820	324.2	333.7	9.5	324.2	331.5	7.30	77
42X	27 Mar	1820	324.2	333.7	9.5	324.2	331.5	7.30	77
43X	27 Mar	1955	333.7	343.2	9.5	333.7	343.7	10.00	105
44X	27 Mar	2145	343.2	352.7	9.5	343.2	353.2	10.04	106
45X	27 Mar	2300	352.7	361.7	9.0	352.7	362.9	10.20	113
46X	28 Mar	0010	361.7	370.7	9.0	361.7	371.6	9.87	110
47X	28 Mar	0055	370.7	379.7	9.0	370.7	379.4	8.67	96
48X	28 Mar	0210	379.7	389.3	9.6	379.7	389.8	10.12	105
49X	28 Mar	0355	389.3	398.1	8.8	389.3	399.4	10.11	115
50X	28 Mar	0530	398.1	407.7	9.6	398.1	408.1	10.02	104
51X	28 Mar	0705	407.7	417.4	9.7	407.7	417.7	9.96	103
52X	28 Mar	0845	417.4	426.2	8.8	417.4	427.4	9.95	113
53X	28 Mar	1030	426.2	436.0	9.8	426.2	436.1	9.93	101
54X	28 Mar	1220	436.0	444.9	8.9	436.0	446.3	10.33	116
55X	28 Mar	1320	444.9	453.7	8.8	444.9	454.9	10.03	114
56X	28 Mar	1415	453.7	463.4	9.7	453.7	463.7	9.97	103
57X	28 Mar	1515	463.4	472.3	8.9	463.4	473.4	10.03	113
58X	28 Mar	1620	472.3	481.1	8.8	472.3	482.4	10.08	115
59X	28 Mar	1750	481.1	490.7	9.6	481.1	491.1	10.03	104
60X	28 Mar	1835	490.7	500.4	9.7	490.7	500.7	10.04	104
61X	28 Mar	1930	500.4	509.3	8.9	500.4	509.9	9.45	106
62X	28 Mar	2035	509.3	518.2	8.9	509.3	518.4	9.06	102
63X	28 Mar	2230	518.2	527.1	8.9	518.2	527.7	9.47	106
64X	29 Mar	0020	527.1	536.8	9.7	527.1	537.2	10.08	104
65X	29 Mar	0225	536.8	546.5	9.7	536.8	546.7	9.94	102
66X	29 Mar	0405	546.5	556.1	9.6	546.5	556.4	9.90	103
67X	29 Mar	0525	556.1	565.7	9.6	556.1	566.1	10.02	104
68X	29 Mar	0655	565.7	574.6	8.9	565.7	575.4	9.74	109
69X	29 Mar	0800	574.6	584.3	9.7	574.6	584.4	9.78	101
70X	29 Mar	0945	584.3	593.9	9.6	584.3	594.2	9.94	104
71X	29 Mar	1110	593.9	603.5	9.6	593.9	603.8	9.94	104
72X	29 Mar	1525	603.5	612.4	8.9	603.5	607.4	3.85	43
73X	29 Mar	1645	612.4	622.0	9.6	612.4	622.3	9.90	103
74X	29 Mar	1810	622.0	631.7	9.7	622.0	630.2	8.18	84
75X	29 Mar	2005	631.7	641.3	9.6	631.7	641.6	9.91	103
76X	29 Mar	2145	641.3	645.8	4.5	641.3	646.7	5.39	120
77X	29 Mar	2255	645.8	651.0	5.2	645.8	651.0	5.18	100
78X	30 Mar	0320	651.0	660.6	9.6	651.0	660.7	9.69	101
79X	30 Mar	0515	660.6	670.2	9.6	660.6	670.1	9.47	99
80X	30 Mar	0655	670.2	679.8	9.6	670.2	680.0	9.79	102
81X	30 Mar	0840	679.8	689.6	9.8	679.8	689.7	9.86	101
84X	30 Mar	1540	708.9	716.4	7.5	708.9	717.7	8.75	117

Table T1 (continued).

Core	Date (2011)	Time (h)	Depth DSF (m) Top of cored interval	Depth DSF (m) Bottom of cored interval	Interval advanced (m)	Depth CSF (m) Top of cored interval	Depth CSF (m) Bottom of cored interval	Length of core recovered (m)	Recovery (%)
85X	30 Mar	1715	716.4	726.1	9.7	716.4	722.5	6.10	63
86X	30 Mar	1900	726.1	735.8	9.7	726.1	736.0	9.91	102
87X	30 Mar	2055	735.8	745.4	9.6	735.8	738.4	2.59	27
88X	30 Mar	2250	745.4	750.4	5.0	745.4	748.0	2.60	52
89X	31 Mar	0050	750.4	756.3	5.9	750.4	756.4	6.00	102
90X	31 Mar	0210	756.3	766.0	9.7	756.3	757.5	1.18	12
91X	31 Mar	0355	766.0	775.3	9.3	766.0	773.1	7.09	76
92X	31 Mar	0535	775.3	785.0	9.7	775.3	781.2	5.90	61
93X	31 Mar	0705	785.0	794.5	9.5	785.0	786.8	1.77	19
94X	31 Mar	1015	794.5	804.1	9.6	794.5	797.3	2.78	29
95X	31 Mar	1150	804.1	813.6	9.5	804.1	813.8	9.70	102
96X	31 Mar	1325	813.6	823.2	9.6	813.6	816.3	2.73	28
97X	31 Mar	1440	823.2	832.1	8.9	823.2	826.5	3.32	37
98X	31 Mar	1600	832.1	841.5	9.4	832.1	840.2	8.11	86
99X	31 Mar	1850	841.5	851.1	9.6	841.5	845.5	3.97	41
100X	31 Mar	2100	851.1	860.7	9.6	851.1	855.3	4.20	44
101X	31 Mar	2235	860.7	870.3	9.6	860.7	870.6	9.88	103
102X	01 Apr	0040	870.3	879.9	9.6	870.3	880.1	9.77	102
103X	01 Apr	0230	879.9	889.6	9.7	879.9	882.4	2.45	25
104X	01 Apr	0540	889.6	899.0	9.4	889.6	890.6	1.01	11
105X	01 Apr	0745	899.0	906.6	7.6	899.0	899.8	0.80	11
106X	01 Apr	0940	906.6	916.4	9.8	906.6	907.4	0.74	8
107X	01 Apr	1155	916.4	924.0	7.6	916.4	916.7	0.28	4
108X	01 Apr	1320	924.0	928.5	4.5	924.0	924.5	0.52	12
109X	01 Apr	1450	928.5	929.5	1.0	928.5	928.9	0.36	36
110X	01 Apr	1630	929.5	932.5	3.0	929.5	929.9	0.43	14
111X	01 Apr	1800	932.5	935.0	2.5	932.5	932.9	0.40	16
112X	01 Apr	1930	935.0	937.0	2.0	935.0	937.2	1.96	98
113X	01 Apr	2055	937.0	939.0	2.0	937.0	938.2	1.17	59
114X	01 Apr	2235	939.0	941.0	2.0	939.0	939.4	0.43	22
115X	02 Apr	0015	941.0	943.0	2.0	941.0	941.5	0.45	23
116X	02 Apr	0240	943.0	945.0	2.0	943.0	945.0	2.03	102
117X	02 Apr	0525	945.0	947.0	2.0	945.0	945.7	0.68	34
118X	02 Apr	0715	947.0	949.0	2.0	947.0	947.5	0.52	26
				Advanced total:	1922.3			824.28	84
				Total interval cored:	959.5				

DRF = drilling depth below rig floor, DSF = drilling depth below seafloor, CSF = core depth below seafloor. H = APC core, X = XCB core, 1 = drilled interval. Time is Universal Time Coordinated.

Table T2. Summary of lithostratigraphic unit thickness from Hole U1379C.

Unit	Upper contact (mbsf)	Lower contact (mbsf)	Unit thickness (m)	Cumulative thickness (m)
I	0.00	0.93	0.93	0.93
II	0.93	651.00	650.07	651.00
III	651.00	879.90	228.90	879.90
IV	879.90	881.75	1.85	881.75
V	881.75	947.52	65.77	947.52

Table T3. Calcareous nannofossil faunal distribution, Hole U1379C. (Continued on next page.)

Core, section	Depth (mbsf)	Calcareous nannofossil zone	Abundance	Preservation	*Calcidiscus leptoporus*	*Calcidiscus macintyrei*	*Ceratolithus cristatus*	*Coccolithus pelagicus*	*Discoaster brouweri*	*Discoaster pentaradiatus*	*Discoaster prepentaradiatus*	*Emiliania huxleyi*	*Gephyrocapsa* small (<4 µm)	*Gephyrocapsa* large (>4 µm)	*Gephyrocapsa caribbeanica*	*Gephyrocapsa oceanica*	*Helicosphaera carteri*	*Helicosphaera hyalina*	*Helicosphaera neogranulata/hyalina*	*Helicosphaera sellii*	*Pontosphaera discopora*	*Pseudoemiliania lacunosa*	*Reticulofenestra* (small)	*Rhabdosphaera clavigeri*	*Syracosphaera histrica*	*Umbilicosphaera sibogae*
334-U1379C-																										
1H-CC	6.68		A	M	C							C			A	A	A									
2H-CC	14.97		A	M	F			F				C			A	A	A				F					
3H-CC	24.50		A	M	C		R					C			A	C										R
4H-CC	30.22		A	M	C		F					F			C	C	A									
5H-CC	36.59		A	M	C		R					F	C	C	C	A	A									
7H-CC	49.06		A	M	C							F	A	C	A	A	A									
10H-CC	63.53		R	M									F		F	F	F									
16H-CC	90.22		C	M									C	F	C	C	C									
18X-CC	91.56		B																							
22X-CC	140.29		C	P											F		C									
23X-CC	149.77		F	P									F	F	R	R	F									
25X-CC	168.06		A	P	F								V	F	C	C	C									
30X-CC	218.57		A	M	C								V	C	A	C	C									
31X-CC	226.47		A	M									V	A	C	C	A		R		R					
32X-CC	236.24		A	M									A	A	A	A	C				F					
33X-CC	245.99	NN21–NN20	A	M									A	C	C	A	A									
34X-CC	255.77		A	M	F								A	C	C	C	A									
35X-CC	265.60		A	M	F								V	C	C	C	C		R							
36X-CC	275.53		A	M	F								V	C	C	C	C									
37X-CC	285.29		A	M	C								V	F	C	C	C									
38X-CC	295.15		A	M	F								A	C	C	C	C									
39X-CC	304.05		B																							
40X-CC	314.42		A	M	C								V	C	A	A	C									
41X-CC	324.39		A	M	C								A	C	C	C	C					F				
42X-CC	331.48		A	M	C								V	C	A	A	C					R				
50X-CC	408.10		A	M									A	C	C	C	C									
51X-CC	417.64		A	P	F								V	C	A	C	C					R				
52X-CC	427.33		A	M	C								V	C	A		C				F					
53X-CC	436.11		A	M	C			F					V	C	A	C										
54X-CC	446.31		A	G	C								V	C	C	A	C				C					
55X-CC	454.91		A	M	C								V	C	C	A	C				C					
56X-CC	466.37		A	M	C			R					A	A	C	A	C		F		C					C
57X-CC	476.20																									
58X-CC	482.36		A	P	C			R					A	C	C	F	C									
65X-CC	556.40		C	P				C					C		C	F	C									
67X-CC	566.10		A	M	C								V	A	C	C										
68X-CC	575.41		F	P									F													
69X-CC	584.36		A	P	F								V	C			C									
70X-CC	594.22		A	G	C								V	A	C	C	C		F	R	F	F				
71X-CC	603.81		A	M	C								V	A	C		A		A	F	F					
72X-CC	607.33		B																							
73X-CC	622.28	NN19	A	M	C			F					V	C	C		A			F		F				
75X-CC	641.59		C	P	C								C	C	F	F	C				C	R				
76X-CC	646.67		C	P	C								C	C	F	F	C				C	R				
77X-CC	650.96		A	M	C								A	C	C	C	A			C	C	R				
79X-CC	670.05		A	G	C			F					A				A		C	A	C	R				
80X-CC	679.97		A	G	C	R							A				A		C	C		R				
81X-CC	689.64		A	G	C	F		F					A				C		C	C	C	F				
82X-CC	699.58		A	M	C			C									A			C	C	R				
83X-CC	707.18		F	P	R	F		F									F			F	R					
84X-CC	717.63		R	P				R									R		R	R						
85X-CC	722.48		F	P				F									F		F	F						

Table T3 (continued).

Core, section	Depth (mbsf)	Calcareous nannofossil zone	Abundance	Preservation	*Calcidiscus leptoporus*	*Calcidiscus macintyrei*	*Ceratolithus cristatus*	*Coccolithus pelagicus*	*Discoaster brouweri*	*Discoaster pentaradiatus*	*Discoaster prepentaradiatus*	*Emiliania huxleyi*	*Gephyrocapsa* small (<4 µm)	*Gephyrocapsa* large (>4 µm)	*Gephyrocapsa caribbeanica*	*Gephyrocapsa oceanica*	*Helicosphaera carteri*	*Helicosphaera hyalina*	*Helicosphaera neogranulata/hyalina*	*Helicosphaera sellii*	*Pontosphaera discopora*	*Pseudoemiliania lacunosa*	*Reticulofenestra* (small)	*Rhabdosphaera clavigeri*	*Syracosphaera histrica*	*Umbilicosphaera sibogae*
86X-CC	736.01	Undetermined	B																							
87X-CC	738.37		B																							
88X-CC	747.98		B																							
89X-CC	756.38		F	P				F									F			R	F					
90X-CC	757.48		R	P				R					R				R									
91X-CC	773.07		F					F					F				F			F						
92X-CC	781.18		B																							
93X-CC	786.60		B																							
94X-CC	797.00		F	P				F					F				F			F	R					
95X-CC	813.78		B																							
96X-CC	816.31		B																							
97X-CC	826.35		F	P	R			F					F				F			R	F					
98X-CC	837.97		F	P	F								C	C	C		C			F						
99X-CC	845.47		B																							
100X-CC	855.30		B																							
101X-CC	870.56		R	P													F			F	R		F			
102X-CC	880.07		B																							
103X-CC	882.23		B																							
104X-CC	890.47		R	P													R			R		R	F			
105X-CC	899.57		R	P													R						F			
106X-CC	907.17	NN17	C	P	C	F		F									C			C		F	F			
107X-CC	916.53		C	P	F	F		F									C			C			C			
108X-CC	924.39		B																							
109X-CC	928.51		C	P	F	F		F	R	R							C			F			C			
110X-CC	929.73		C	P	C			F	R	F							C			C			C			
116X-CC	945.03		F	P	F			F									F			R			C			
117X-CC	945.66		F	P	F			F	R	R							F			F			C			
118X-CC	947.25		F	P	F			F	R		R						F			R			C			

Abundance: V = very abundant, A = abundant, C = common, F = few, R = rare, B = barren. Preservation: G = good, M = moderate, P = poor. See **"Paleontology and biostratigraphy"** in the "Methods" chapter (Expedition 334 Scientists, 2012) for abundance and preservation definitions.

Table T4. Planktonic foraminiferal faunal distribution, Hole U1379C.

Core, section	Depth (mbsf)	Preservation	*Globigerina bulloides*	*Globigerinella obesa*	*Globigerinita glutinata*	*Globigerinoides conglobatus*	*Globigerinoides extremus*	*Globigerinoides pyramidalis*	*Globigerinoides quadrilobatus*	*Globigerinoides ruber*	*Globigerinoides tenellus*	*Globorotalia crassula*	*Globorotalia fimbriata*	*Globorotalia menardii* (dextral)	*Globorotalia menardii* (sinistral)	*Globorotalia scitula*	*Globorotalia truncatulinoides*	*Globorotalia tumida* (dextral)	*Globorotalia tumida* (sinistral)	*Globorotalia ungulata*	*Globorotaloides hexagona*	*Neogloboquadrina dutertrei*	*Neogloboquadrina humerosa*	*Neogloboquadrina incompta* (dextral)	*Neogloboquadrina pachyderma* (sinistral)	*Orbulina bilobata*	*Orbulina universa*	*Pulleniatina finalis*	*Pulleniatina obliquiloculata*	*Pulleniatina praecursor*	*Pulleniatina* (dextral)	*Pulleniatina* (sinistral)	Unidentified specimens
334-U1379C-																																
1H-CC	6.63	G						2	11	15			1						7			18		6			1					
4H-CC	30.17	G	8			1				4									5	1		13		4	1		1					
5H-CC	36.56	G	15		2					4					1				2			11		3								
10H-CC	63.50	M	1			1				4												4		1								
11H-CC	67.65	G	5						6	4					1				3			5		1								
16H-CC	90.17	G	2		1				9		1			1			1			1				1			2					
20X-CC	117.11	G	1	1					9	5				1				1	1			3					1					
30X-CC	218.52	G				1		1	8	3				6								6		7			5					
39X-CC	304.02	P							3										1			1					2					
50X-CC	408.07	G							2	4									2		1	7		2			2					
53X-CC	436.08	G				2			1			1			9					2		7	2			1	1		4		4		
58X-CC	482.33	G			1				8	3					3							3		3			1					
64X-CC	537.13	G								3					1				3			2		14					3	1		4	
68X-CC	575.36	G							2	1					1							2									1	2	
80X-CC	679.94	M	1		1		2		1	5						1							1						1		2		4	
90X-CC	757.43	—																															
103X-CC	882.30	—																															
112X-2	937.16	P																															8

Preservation: G = good, M = moderate, P = poor, — = no specimens. See **"Paleontology and biostratigraphy"** in the "Methods" chapter (Expedition 334 Scientists, 2012) for preservation definitions.

Table T5. Benthic foraminiferal faunal distribution, Hole U1379C. (Continued on next page.)

Core, section	Depth (mbsf)	Abundance	Preservation	*Ammonia beccarii*	*Angulogerina angulosa*	*Bolivina acuminata*	*Bolivina advena*	*Bolivina argentea*	*Bolivina decussata*	*Bolivina interjuncta bicostata*	*Bolivina humilis*	*Bolivina pacifica*	*Bolivina seminuda*	*Bolivina spinata*	*Bolivina subadvena*	*Bolivina* sp.	*Bolivina semiperforata*	*Bolivina spinescens*	*Bolivina spissa*	*Bolivina wissleri*	*Bolivina vaughani*	*Bulimina denudata*	*Bulimina marginata*	*Bulimina mexicana*	*Buliminella curta*	*Buliminella elegantissima*	*Cassidulina* sp.	*Cancris auricula*	*Cassidulina californica*	*Cassidulina delicata*	*Cassidulina reniforme*	*Cassidulina limbata*	*Cibicides lobatulus*	*Cibicides reflugens*	*Cibicidoides mckannai*	*Elphidium crispum*	*Epistominella pacifica*	*Fissurina* sp.
334-U1379C-																																					
1H-CC	6.63	H	G		1							3					2		2				7				15	2									
3H-CC	24.45	V	G			46				26						1		1	3		1		5				7	2	2			1					
5H-CC	36.56	A	G			15				3	6	1							2				1				15	1									
10H-CC	63.50	A	M							1																						1		12			
11H-CC	67.65	A	G			9				9		11			2			10					2				25								3		
16H-CC	90.17	A	G	1		1			1	1	2			3					2				3		1	1	1	1		1							2
20X-CC	117.11	A	G	1										1								2	2				10										
30X-CC	218.52	A	G							19		1			4							1	1		1		10				1				6		
39X-CC	304.02	A	M			3				5		8			3														1			12		1	3		
50X-CC	408.07	A	G			2		1		4			1		2												1										
58X-CC	482.33	C	G			1	4			12					2		1								2												
68X-CC	575.36	C	G			4				11		2			1		4								2		1			1	1			1	4		
80X-CC	679.94	C	G			1		13				2			1		1										2			1					2		
90X-CC	757.43	C	M					3		2																											
103X-CC	882.30	F	P																														10				
112X-2	937.16	F	P					3				3								3				1								21						

Abundance: H = highly abundant, V = very abundant, A = abundant, C = common, F = few. Preservation: G = good, M = moderate, P = poor. See **"Paleontology and biostratigraphy"** in the "Methods" chapter (Expedition 334 Scientists, 2012) for abundance and preservation definitions. PF = planktonic foraminifers, BF = benthic foraminifers.

Table T5 (continued).

Core, section	Depth (mbsf)	Abundance	Preservation	*Fursenkoina fusiformis*	*Fursenkoina pontoni*	*Globobulimina auriculata*	*Globobulimina pacifica*	*Globocassidulina subglobosa*	*Gyroidina neosoldanii*	*Gyroidina rothwelli*	*Hanzawaia nitida*	*Hanzawaia bertheloti*	*Lagena* sp.	*Lenticulina calcar*	Miliolid taxa	*Nonionella atlantica*	*Nonionella basispinata*	*Nonionellina labradorica*	*Nonionella miocenica*	*Nonionella stella*	*Oridorsalis umbonatus*	*Planulina ornata*	*Pseudoparrella* sp.	*Pseudoparrella naraensis*	*Quinqueloculina seminula*	*Quinqueloculina angulosa*	*Rosalina vilardeboana*	*Stainforthia fusiformis*	*Suggrunda eckisi*	*Triloculina* sp.	*Trifarina* sp.	*Uvigerina excellens*	*Uvigerina peregrina*	*Uvigerina senticosa*	*Uvigerina* sp.	*Valvulineria araucana*	*Virgulina schreiberriana*	PF/(PF + BF)
334-U1379C-																																						
1H-CC	6.63	H	G		1		2	1					1	1	1	1	2	1						6	2					1			18						0.18
3H-CC	24.45	V	G				1					1				1			5					15				6				6	1	22	2			0.24
5H-CC	36.56	A	G		1		2	1																					2	1		1						0.12
10H-CC	63.50	A	M								2																											0.16
11H-CC	67.65	A	G																	2				2				1	1			15	1					0.09
16H-CC	90.17	A	G								2				3			1		1			2		1	1	3					1		2	1	1		0.39
20X-CC	117.11	A	G	1														1					5									5				1		0.18
30X-CC	218.52	A	G					1																					1				3		1			0.05
39X-CC	304.02	A	M																			1									1	2		1				0.09
50X-CC	408.07	A	G					3	1	2											1		1									1		2	1			0.36
58X-CC	482.33	C	G						2												1				1						1							0.21
68X-CC	575.36	C	G					1						1									2									3						0.02
80X-CC	679.94	C	G						3														5									1						0.05
90X-CC	757.43	C	M																													17						0.00
103X-CC	882.30	F	P																																			0.00
112X-2	937.16	F	P			2			2													9										4						0.13

Table T6. Interstitial water chemistry, Site U1379. (Continued on next two pages.)

Core, section, interval (cm)	Depth (mbsf)	Volume (mL)	Salinity	Alkalinity (mM)	pH	Cl (mM)	SO_4 (mM)		NH_4 (mM)	K (mM)	Mg (mM)	Ca (mM)
							IC	ICP				
334-U1379B-												
1H-1, 70–80	0.70	40	35	2.97	7.90	—	—	—	—	11.46	52.27	10.81
2H-1, 110–120	2.10	50	35	5.74	7.54	—	—	—	—	12.59	54.28	9.89
2H-2, 35–45	2.85	50	35	6.87	7.48	—	—	—	—	11.25	53.52	9.28
2H-2, 110–120	3.60	44	35	8.18	7.52	—	—	—	0.72	10.94	51.82	8.68
2H-3, 35–45	4.35	50	35	9.18	7.57	—	—	—	1.17	10.85	47.37	7.48
2H-3, 110–120	5.10	53	34	10.29	7.79	—	—	—	1.15	10.16	49.63	7.41
2H-4, 35–45	5.85	54	35	11.35	7.58	—	—	—	1.47	9.25	44.19	6.25
2H-4, 110–120	6.60	52	34	12.61	7.59	—	—	—	1.60	10.01	48.69	6.53
2H-5, 88–98	7.88			14.67	7.57	—	—	—	2.16	—	—	—
334-U1379C-												
1H-1, 140–150	1.40	—	—	4.06	7.62	558	26.50	24.06	0.71	10.14	44.31	8.52
1H-2, 140–150	2.90	50	35	6.05	7.58	—	26.95	22.36	1.21	10.04	44.99	7.90
1H-3, 140–150	4.40	50	35	7.63	7.56	—	24.85	19.65	1.85	9.82	43.28	7.11
1H-4, 140–150	5.90	45	35	10.35	7.54	—	15.95	16.67	3.04	10.09	47.78	6.91
1H-5, 50–63	6.50	44	35	11.71	7.49	559	16.60	15.45	3.28	9.67	49.80	6.70
2H-1, 140–150	8.10	50	33	13.28	7.47	—	12.12	13.19	3.80	10.06	50.28	6.19
2H-2, 140–150	9.60	50	33	14.72	7.54	560	9.90	10.17	4.66	10.08	47.54	5.25
2H-3, 140–150	11.10	50	33	15.60	7.55	—	6.21	8.70	4.76	11.48	47.96	4.69
2H-4, 140–150	12.60	40	33	16.48	7.52	—	3.85	6.59	5.42	10.04	46.33	4.19
2H-5, 140–150	14.10	40	33	17.31	7.55	—	4.55	5.12	4.55	9.75	46.36	3.82
2H-6, 36–46	14.56	40	33	17.36	7.58	563	6.58	4.10	5.33	9.84	42.82	3.44
3H-1, 138–150	17.58	50	34	16.82	7.65		5.97	4.34	2.68	8.67	37.32	2.92
3H-2, 138–150	19.08	50	33	17.30	7.73	564	3.14	3.42	2.92	9.28	42.57	3.02
3H-3, 138–150	20.58	48	33	17.22	7.68	—	1.86	3.07	2.88	9.79	46.07	3.24
3H-4, 138–150	22.08	48	33	17.56	7.55	—	ND	2.38	2.79	9.27	42.26	2.89
3H-5, 138–150	23.58	50	33	17.03	7.73	566	1.73	1.71	3.06	9.86	45.97	2.78
3H-6, 39–50	24.09	48	33	16.57	7.73	—	ND	1.56	2.93	9.69	44.12	2.54
4H-2, 138–150	27.08	46	33	15.92	7.67	565	ND	1.19	3.27	9.93	44.47	2.56
4H-4, 92–104	29.62	44	33	16.13	7.78	—	ND	ND	3.22	10.08	44.30	2.58
5H-2, 138–150	33.08	48	33	16.54	7.69	566	ND	ND	—	10.02	44.04	2.44
5H-4, 149–161	36.19	48	32	16.43	7.74	566	ND	ND	3.27	9.94	44.01	2.65
6H-2, 138–150	39.38	48	33	16.62	7.63	567	ND	ND	3.32	9.73	43.13	2.70
6H-4, 138–150	42.38	42	33	17.14	7.63	568	ND	ND	3.67	11.20	42.30	2.96
7H-2, 138–150	45.38	40	33	17.03	7.55	567	ND	ND	3.52	9.82	42.85	3.48
7H-4, 136–148	48.36	50	33	16.36	7.65	566	ND	ND	3.57	9.61	41.23	3.48
8H-2, 138–150	51.98	50	33	16.13	7.61	565	ND	ND	3.67	9.53	41.71	3.67
8H-4, 130–142	54.90	45	33	15.02	7.61	562	ND	ND	3.42	—	—	—
9H-2, 138–150	58.38	48	32	12.50	8.03	561	ND	ND	3.72	9.06	40.16	3.94
9H-4, 128–140	61.28	50	33	9.24	7.80	560	ND	ND	3.50	9.48	38.88	4.05
10H-1, 88–100	62.38	15	35	8.28	7.85	560	ND	ND	3.49	9.28	37.75	4.84
11H-1, 138–150	64.88	45	33	5.61	7.74	—	ND	ND	3.64	8.39	38.36	5.31
11H-3, 78–90	67.28	45	33	4.22	8.30	560	ND	ND	3.39	9.01	35.50	4.69
12H-2, 138–150	70.58	30	32	4.51	7.95	—	ND	1.86	3.66	8.36	36.80	5.14
12H-4, 103–115	73.23	40	32	4.01	7.99	—	ND	—	3.29	—	—	—
13H-2, 138–150	76.58	35	32	5.12	7.96	561	ND	ND	3.48	7.71	37.36	5.03
14H-2, 138–150	81.58	42	32	5.20	8.31	559	ND	ND	3.85	8.22	36.15	4.72
15H-3, 100–112	86.15	34	32	6.45	7.98	560	ND	0.77	3.49	7.57	38.11	5.33
16H-2, 138–150	89.38	35	32	6.95	8.18	—	ND	ND	4.16	7.87	38.14	5.19
17H-1, 76–89	90.96	34	32	7.15	7.94	559	1.46	2.48	3.80	7.41	38.76	5.52
20X-1, 137–150	112.07	28	32	8.29	7.81	—	ND	1.35	5.17	6.81	37.75	6.35
20X-3, 137–150	115.07	15	32	7.45	7.76	558	2.35	1.17	6.68	6.88	37.24	6.63
21X-3, 133–145	124.83	34	32	7.97	7.83	559	1.14	1.6	6.70	7.69	37.28	7.28
22X-3, 137–150	133.52	25	32	7.44	7.93	558	ND	1.48	8.02	6.93	36.38	7.35
22X-6, 138–150	138.03	20	32	6.67	8.07	—	ND	ND	7.93	7.16	34.83	7.08
23X-1, 138–150	—	12	32	—	—	555	—	ND	7.86	7.51	35.92	7.46
24X-3, 133–150	154.23	28	32	7.98	7.65	—	ND	ND	8.37	6.76	37.43	7.92
24X-6, 124–141	158.64	28	32	5.42	8.14	557	ND	ND	9.62	7.97	34.53	6.99
25X-3, 133–150	164.03	20	33	8.93	7.81	556	ND	ND	8.67	6.90	38.81	7.90
25X-5, 128–145	166.98	30	32	—	—	—	—	ND	8.62	6.58	38.62	7.72
26X-3, 133–150	178.13	26	33	—	—	—	ND	1.03	9.06	7.43	38.53	7.40
26X-6, 113–130	178.13	30	33	—	—	556	ND	1.28	8.81	7.86	38.82	7.41
27X-3, 133–150	183.63	35	32	—	—	555	ND	ND	8.72	7.17	39.17	6.93
27X-6, 113–130	187.93	40	34	—	—	—	ND	ND	8.55	9.65	38.08	6.65
28X-3, 133–150	192.32	30	32	10.78	7.79	—	ND	ND	7.94	6.27	39.28	7.13
28X-6, 133–150	196.74	—	—	9.52	7.88	556	ND	ND	6.82	7.39	40.53	7.35
29X-1, 133–150	200.23	8	33	—	—	—	ND	ND	8.41	6.68	38.95	7.50
29X-4, 120–137	204.54	14	33	—	—	558	ND	—	7.68	—	—	—

Table T6 (continued). (Continued on next page.)

Core, section, interval (cm)	Depth (mbsf)	Volume (mL)	Salinity	Alkalinity (mM)	pH	Cl (mM)	SO_4 (mM) IC	SO_4 (mM) ICP	NH_4 (mM)	K (mM)	Mg (mM)	Ca (mM)
30X-2, 133–150	211.53	30	33	9.84	7.77	—	1.45	ND	7.58	6.32	39.33	7.62
30X-5, 123–140	215.43	14	32	9.05	7.97	557	6.87	ND	7.14	6.48	38.49	7.32
31X-2, 133–150	219.33	32	33	8.31	7.89	—	ND	2.99	6.68	6.43	41.97	8.05
31X-5, 133–150	223.83	26	32	6.41	8.04	560	ND	0.77	7.70	6.58	38.18	7.13
32X-2, 133–150	229.13	21	32	6.99	7.98	556	ND	0.84	7.29	6.29	38.62	7.08
32X-6, 133–150	235.13	20	32	5.14	8.08	—	ND	0.54	8.37	6.61	37.13	6.43
33X-5, 122–144	262.48	18	32	—	—	560	ND	0.43	6.77	6.02	38.21	6.49
34X-3, 128–150	250.18	20	32	6.46	7.87	558	ND	0.66	7.16	6.15	37.35	5.82
35X-5, 78–100	262.48	16	32	—	—	556	ND	0.59	7.16	6.65	35.85	5.81
36X-5, 128–150	271.74	18	31	10.13	7.88	558	ND	0.87	7.24	6.54	37.79	6.35
37X-5, 128–150	282.58	22	31	12.05	7.82	557	ND	1.53	7.83	6.53	37.07	6.81
38X-5, 128–150	292.38	22	32	9.33	8.05	556	1.83	1.13	8.54	7.09	34.64	6.33
39X-3, 129–150	299.19	20	32	11.87	7.75	553	2.09	2.3	8.16	6.73	35.77	7.51
40X-4, 100–122	310.20	—	—	—	—	552	2.93	2.54	8.32	7.50	35.27	8.83
41X-4, 128–150	320.28	30	33	11.47	7.69	552	1.72	—	9.14	—	—	—
42X-3, 123–145	328.43	8	33	—	—	550	ND	1.53	9.43	8.70	31.30	8.36
43X-6, 81–107	341.41	18	33	12.44	7.71	551	1.17	0.13	9.92	9.43	30.45	8.62
44X-6, 78–107	350.88	18	33	—	—	555	1.93	1.35	9.43	8.52	30.03	9.27
45X-4, 118–140	358.38	8	32	—	—	551	ND	1.2	9.12	7.78	28.86	9.82
46X-5, 75–100	368.45	16	33	—	—	553	ND	BDL	9.66	9.15	28.14	10.46
47X-5, 133–156	378.03	16	32	10.69	7.78	553	ND	2.12	9.59	9.00	29.84	11.20
48X-6, 63–100	386.36	18	32	10.17	7.91	554	1.19	ND	9.94	7.63	30.30	11.23
49X-6, 75–100	395.85	13	32	—	—	555	3.35	1.64	9.59	8.11	31.29	11.28
50X-5, 104–132	405.14	18	32	6.03	8.03	552	1.73	1.69	9.61	7.60	30.30	9.91
51X-4, 104–129	412.54	—	—	—	—	552	2.59	0.98	8.96	6.87	33.17	10.69
52X-2, 118–150	420.08	25	32	6.33	7.72	553	2.6	3.33	8.27	7.34	33.53	10.57
53X-3, 118–150	430.38	18	32	5.57	7.88	—	2.59	3.57	—	7.07	34.76	10.81
54X-4, 75–107	439.62	18	32	5.54	7.88	552	ND	3.45	7.07	6.58	36.64	12.13
55X-3, 87–119	448.07	18	32	4.91	7.98	553	ND	2.25	7.04	6.72	36.38	13.43
56X-4, 100–132	458.70	36	32	3.73	7.92	555	ND	2.28	6.78	6.86	37.21	15.01
57X-3, 118–150	467.58	18	32	—	—	556	ND	2.02	6.55	6.54	36.18	16.66
58X-4, 90–129	477.50	36	32	3.08	8.03	556	1.63	2.37	5.51	5.86	35.09	17.99
59X-4, 106–138	486.66	12	32	—	—	556	ND	2.04	5.34	5.28	34.00	19.08
60X-4, 118–150	496.38	10	33	—	—	559	ND	2.24	6.00	5.81	32.64	20.13
61X-5, 118–150	507.58	28	32	2.41	8.25	—	ND	0.79	5.55	5.63	31.29	19.05
62X-4, 68–100	514.48	14	32	—	—	557	ND	2.23	5.42	5.87	31.61	19.43
63X-5, 118–150	524.88	15	33	1.95	8.15	557	ND	2.08	5.43	5.30	29.41	17.75
64X-5, 125–150	534.35	18	33	—	—	555	ND	0.76	5.61	5.55	28.35	16.72
65X-6, 78–114	545.08	16	32	—	—	—	ND	1.2	—	5.42	29.53	16.63
67X-6, 70–100	563.80	12	32	2.04	8.25	552	ND	1.53	5.38	5.41	29.58	15.26
68X-4, 88–120	570.38	12	32	—	—	548	ND	2.81	5.12	5.05	31.68	15.35
69X-3, 93–125	578.33	16	33	—	—	546	5.21	0.2	5.30	5.25	29.65	15.81
70X-4, 92–124	589.72	20	32	4.73	8.08	540	ND	2.2	5.52	5.33	28.26	15.42
71X-4, 64–96	598.54	16	32	4.34	7.70	537	—	3.66	4.73	5.38	28.95	15.27
72X-2, 88–120	605.28	14	32	—	—	540	—	1.47	—	5.05	25.76	13.73
73X-5, 116–150	619.56	10	31	—	—	539	—	0.59	—	6.08	23.71	13.29
74X-4, 74–107	626.34	15	32	—	—	—	—	2.58	6.04	6.72	24.12	13.25
75X-4, 86–120	636.37	15	32	—	—	534	—	2.16	—	6.66	21.64	12.24
76X-3, 118–150	645.21	8	31	—	—	—	—	1.92	—	6.60	21.79	12.00
77X-2, 118–150	648.48	7	31	—	—	533	—	2.22	6.02	6.51	21.94	12.28
78X-4, 110–140	656.60	11	30	—	—	535	—	1.83	6.39	6.71	21.93	12.05
79X-4, 70–100	664.98	10	30	—	—	534	—	1.68	6.14	6.55	21.06	11.72
80X-4, 93–125	674.74	10	32	—	—	528	—	1.7	6.22	5.94	21.73	11.70
81X-2, 100–132	682.00	10	31	—	—	524	—	1.59	5.85	6.25	22.10	11.47
82X-3, 70–102	692.60	6	30	—	—	—	—	1.38	—	5.64	22.06	11.25
83X-1, 60–92	699.80	10	30	—	—	—	—	1.58	—	5.52	23.31	11.65
84X-3, 56–88	712.41	8	30	—	—	—	—	0.45	—	5.95	23.72	12.65
85X-1, 77–112	717.17	17	30	—	—	524	—	1.31	5.37	6.43	22.18	12.15
86X-2, 87–119	728.47	—	—	—	—	—	—	—	—	—	—	—
88X-1, 118–150	746.58	—	—	—	—	—	—	—	—	—	—	—
89X-2, 0–40	751.63	—	—	—	—	—	—	1.99	—	5.76	23.52	13.95
91X-4, 50–85	770.31	2	30	—	—	528	—	1.32	—	5.17	21.86	13.83
92X-3, 94–131	778.90	9	30	—	—	—	—	1.45	—	5.55	22.98	14.35
93X-1, 22–50	785.22	1	30	—	—	—	—	—	—	—	—	—
94X-1, 56–91	795.06	2	30	—	—	—	—	4.83	—	5.18	22.42	14.51
95X-3, 118–150	807.48	11	30	—	—	533	—	1.19	—	5.71	22.76	16.63
97X-2, 68–100	824.78	—	—	—	—	—	—	—	—	—	—	—
98X-4, 79–115	837.26	18	29	—	—	534	—	1.89	3.50	5.09	21.62	18.70
99X-2, 118–150	844.18	5	31	—	—	536	—	2.84	—	5.06	21.36	22.08

Table T6 (continued).

Core, section, interval (cm)	Depth (mbsf)	Volume (mL)	Salinity	Alkalinity (mM)	pH	Cl (mM)	SO_4 (mM)		NH_4 (mM)	K (mM)	Mg (mM)	Ca (mM)
							IC	ICP				
100X-2, 56–88	852.66	1	30	—	—	—	—	0.87	—	5.42	19.06	25.01
101X-4, 58–90	865.28	—	—	—	—	—	—	0.56	—	4.86	15.98	27.35
102X-5, 110–140	877.40	3	30	—	—	546	—	3.35	—	4.15	11.97	31.38
103X-2, 34–60	881.24	6	30	—	—	548	—	2.46	—	3.84	12.95	34.55

IC = ion chromatography, ICP = inductively coupled plasma–atomic emission spectroscopy. BDL = below detection limit. — = not measured, ND = not detectable.

Table T7. Gas geochemistry, Site U1379. (Continued on next page.)

Average depth (mbsf)	Sample type	CH_4 (ppmv)	C_2H_4 (ppmv)	C_2H_6 (ppmv)	$C_3H_6 + C_3H_8$ (ppmv)	*iso*-C_4H_{10} (ppmv)	*n*-C_4H_{10} (ppmv)	*iso*-C_5H_{12} (ppmv)	*n*-C_5H_{12} (ppmv)	$CH_4/(C_2H_6 + C_3H_8)$
1.39	NZ	3.70	0.0	0.0	0.0	0.0	0.0	0.0	0.0	ND
2.84	NZ	2.54	0.0	0.0	0.0	0.0	0.0	0.0	0.0	ND
4.39	NZ	3.17	0.0	0.0	1.2	0.6	0.0	0.0	0.0	ND
5.84	NZ	3.21	0.0	0.0	0.0	0.0	0.0	0.0	0.0	ND
6.49	NZ	3.39	0.0	0.0	0.0	0.0	0.0	0.0	0.0	ND
8.09	NZ	2.87	0.0	0.0	0.0	0.0	0.0	0.0	0.0	ND
9.59	NZ	3.19	0.0	0.0	0.0	0.0	0.0	0.0	0.0	ND
11.09	NZ	2.61	0.0	0.0	0.0	0.0	0.0	0.0	0.0	ND
12.59	NZ	2.48	0.0	0.0	0.0	0.0	0.0	0.0	0.0	ND
14.09	NZ	2.59	0.0	0.0	0.0	0.0	0.0	0.0	0.0	ND
14.55	NZ	2.72	0.0	0.0	0.0	0.0	0.0	0.0	0.0	ND
17.57	NZ	4.88	0.0	0.0	0.0	0.0	0.0	0.0	0.0	ND
19.07	NZ	2.64	0.0	0.0	0.0	0.0	0.0	0.0	0.0	ND
20.57	NZ	3.35	0.0	0.0	0.0	0.0	0.0	0.0	0.0	ND
22.07	NZ	6.03	0.0	0.0	0.0	0.0	0.0	0.0	0.5	ND
23.57	NZ	5.98	0.0	0.0	0.0	0.0	0.0	0.0	0.0	ND
24.08	NZ	4.44	0.0	0.0	0.0	0.0	0.0	0.0	0.0	ND
27.04	NZ	3.30	0.0	0.0	0.0	0.0	0.0	0.0	0.0	ND
29.56	NZ	4.60	0.0	0.0	0.0	0.0	0.0	0.0	0.0	ND
39.32	NZ	15.43	0.0	0.0	0.0	0.0	0.0	0.6	0.0	ND
42.32	NZ	1,226.60	0.0	0.0	0.0	0.0	0.0	0.7	0.0	ND
48.29	NZ	3,129.05	0.0	0.0	0.7	0.3	0.0	0.9	0.0	4,771.53
54.83	NZ	4,913.62	0.0	0.6	0.0	0.0	0.0	0.6	0.0	8,232.42
61.21	NZ	4,807.16	0.0	0.6	0.0	0.0	0.0	0.0	0.0	8,225.89
62.31	NZ	5,215.17	0.0	0.6	0.0	0.0	0.0	0.0	0.0	9,012.39
67.21	NZ	13,233.84	0.0	1.3	0.0	0.0	0.0	0.0	0.0	10,289.91
73.16	NZ	12,320.66	0.0	1.5	0.0	0.0	0.0	0.0	0.0	8,392.04
76.51	NZ	13,510.23	0.0	2.2	0.0	0.0	0.0	0.0	0.0	6,167.13
81.51	NZ	11,026.81	0.0	1.6	0.0	0.0	0.0	0.0	0.0	6,926.76
86.08	NZ	2,651.57	0.0	0.6	0.0	0.0	0.0	0.0	0.0	4,687.36
89.31	NZ	12,838.62	0.0	2.2	0.0	0.0	0.0	0.0	0.0	5,957.19
90.89	NZ	3,973.59	0.0	0.6	0.0	0.0	0.0	0.0	0.0	6,234.31
115.01	NZ	7,078.96	0.0	1.6	0.0	0.0	0.0	0.0	0.0	4,451.79
138.02	NZ	1,656.88	0.0	0.7	ND	ND	0.0	0.0	0.0	2,360.25
141.47	NZ	5,168.49	0.0	1.5	ND	ND	0.0	0.0	0.0	3,562.85
158.63	NZ	6,583.04	ND	1.8	1.2	0.7	0.9	1.3	1.9	2,246.98
166.97	NZ	3,778.29	ND	1.5	0.0	0.0	0.0	0.0	0.0	2,471.88
178.12	NZ	5,060.56	ND	1.8	0.0	0.0	0.0	0.0	0.0	2,750.69
187.92	NZ	7,488.91	ND	3.0	0.0	0.0	0.0	0.0	0.0	2,527.02
196.62	NZ	5,395.71	ND	2.2	0.0	0.0	0.0	0.0	0.0	2,438.22
204.51	NZ	11,334.34	ND	3.4	0.4	0.0	0.0	0.0	0.0	2,985.69
215.41	NZ	4,270.85	ND	2.1	0.0	0.0	0.0	0.0	0.0	2,055.10
223.81	NZ	6,368.38	ND	2.8	1.1	0.5	0.8	1.1	1.3	1,630.92
235.11	NZ	7,802.60	ND	3.6	1.8	0.0	0.0	0.0	23.6	1,458.34
341.39	NZ	3,223.09	ND	2.1	1.2	0.0	0.0	0.0	0.0	987.82
350.75	NZ	7,800.17	ND	5.4	3.3	ND	ND	ND	0.0	899.08
358.26	NZ	7,217.43	ND	5.4	4.0	ND	0.4	ND	0.0	763.71
368.43	NZ	6,158.45	ND	4.5	3.3	ND	0.4	ND	0.0	790.02
378.01	NZ	7,600.70	ND	6.4	4.3	ND	ND	ND	ND	708.56
386.71	NZ	4,288.35	ND	3.5	2.9	ND	ND	ND	ND	671.72
395.83	NZ	2,036.47	ND	1.7	1.4	0.0	0.0	0.0	0.0	647.36
405.07	NZ	3,856.66	ND	3.2	2.1	0.3	0.3	0.7	0.0	719.92

Table T7 (continued).

Average depth (mbsf)	Sample type	CH_4 (ppmv)	C_2H_4 (ppmv)	C_2H_6 (ppmv)	$C_3H_6 + C_3H_8$ (ppmv)	*iso*-C_4H_{10} (ppmv)	*n*-C_4H_{10} (ppmv)	*iso*-C_5H_{12} (ppmv)	*n*-C_5H_{12} (ppmv)	$CH_4/(C_2H_6 + C_3H_8)$
412.52	NZ	1,296.66	ND	1.6	1.6	0.4	0.0	1.0	0.0	410.60
420.06	NZ	8,344.84	ND	9.5	10.5	2.3	1.3	6.1	0.7	416.52
430.36	NZ	7,384.96	ND	6.9	6.8	1.2	0.7	3.2	0.3	537.23
439.60	NZ	1,402.40	ND	1.6	1.8	0.3	0.0	0.8	0.0	406.48
448.05	NZ	1,419.54	ND	1.6	1.4	0.0	0.0	0.0	0.0	478.03
458.68	NZ	2,853.04	ND	3.4	1.7	0.4	0.0	0.3	0.0	558.40
467.56	NZ	3,993.23	ND	3.5	1.2	0.0	0.0	0.3	0.0	856.12
480.87	NZ	8,588.63	ND	4.5	0.5	0.0	0.0	0.0	0.0	1,735.58
486.64	NZ	8,781.10	ND	6.8	0.6	0.0	0.0	0.0	0.0	1,197.57
493.68	NZ	4,532.04	ND	2.6	0.0	0.0	0.0	0.0	0.0	1,777.03
507.56	NZ	3,142.06	ND	2.2	1.0	0.5	0.0	0.7	0.0	976.39
514.46	NZ	1,139.08	ND	0.9	0.9	0.4	0.0	1.0	0.0	639.59
525.23	NZ	5,584.21	ND	5.8	6.8	2.3	0.7	3.6	0.0	444.87
545.06	NZ	3,512.26	ND	3.8	5.6	1.6	0.5	1.8	0.0	372.90
554.53	NZ	6,219.53	ND	7.2	10.9	3.2	0.8	3.5	0.0	344.89
563.78	NZ	5,962.68	ND	6.9	8.2	1.7	0.4	1.5	0.0	394.97
573.68	NZ	5,515.73	ND	6.2	8.0	1.4	0.5	1.5	0.0	388.63
578.31	NZ	1,051.66	ND	0.9	0.9	0.0	0.0	0.0	0.0	588.61
589.70	NZ	6,142.59	ND	4.3	2.7	0.0	0.0	0.0	0.0	873.89
598.52	NZ	936.17	ND	2.5	4.3	1.2	0.3	1.7	0.0	136.59
605.26	NZ	4,145.33	ND	6.2	9.2	4.0	0.8	5.4	0.4	270.82
619.54	NZ	3,398.52	ND	6.0	8.5	4.2	0.5	4.3	0.0	233.44
626.32	NZ	5,608.92	ND	8.0	9.2	3.6	0.5	2.0	0.0	326.91
636.30	NZ	2,089.75	ND	4.1	6.2	2.8	0.5	1.6	0.0	202.79
656.58	NZ	4,641.12	ND	7.8	10.2	3.2	3.4	0.3	1.2	258.54
664.96	NZ	5,200.45	ND	7.8	9.5	2.9	0.4	1.1	0.0	300.30
674.72	NZ	5,801.58	ND	9.6	12.4	4.4	0.7	2.5	0.0	263.59
681.98	NZ	7,924.37	ND	11.3	14.5	5.7	2.3	5.0	3.1	307.09
692.58	NZ	4,670.33	ND	8.9	10.4	2.8	0.9	2.0	0.0	241.88
699.78	NZ	2,492.71	ND	3.9	5.3	1.3	0.9	1.4	1.0	273.30
712.39	NZ	3,191.88	ND	2.6	2.7	1.0	0.5	1.2	0.0	596.99
717.15	NZ	1,286.06	ND	2.0	2.8	1.0	0.5	0.6	0.0	265.67
733.27	NZ	10,048.24	ND	10.1	8.2	2.8	0.9	1.7	0.0	548.83
772.14	NZ	7,517.90	ND	7.6	5.7	3.6	0.1	1.5	0.0	567.92
780.25	NZ	5,993.83	ND	5.7	4.6	2.9	0.3	0.9	0.0	584.06
785.53	HS	3,616.59	0.0	3.5	2.9	2.0	0.3	0.8	0.0	566.29
795.04	HS	4,411.44	0.0	4.6	5.7	4.8	0.4	2.2	0.0	427.62
807.46	NZ	1,515.16	ND	1.4	1.3	1.0	0.0	0.4	0.0	559.21
815.13	NZ	4,917.51	ND	6.2	4.7	3.9	0.9	1.1	0.0	451.41
824.76	NZ	1,502.31	ND	3.2	2.9	2.2	0.0	0.5	0.0	245.90
837.24	NZ	1,352.89	ND	1.2	1.3	1.0	0.4	0.6	0.0	554.92
852.64	NZ	3,696.37	ND	4.1	3.1	2.3	0.0	0.8	0.0	513.66
865.26	NZ	5,061.85	ND	5.2	2.9	1.7	0.0	0.6	0.0	625.26
877.38	NZ	7,630.09	ND	14.1	5.4	2.2	ND	0.8	0.0	392.83
890.21	HS	3,708.49	ND	2.3	0.4	0.0	0.0	0.0	0.0	1,363.62
899.40	HS	1,201.20	ND	1.2	0.0	0.0	0.0	0.0	0.0	962.12
929.51	HS	9,629.98	ND	9.0	2.6	1.0	0.0	0.4	0.0	833.90
930.00	HS	3,115.64	ND	3.4	0.8	ND	ND	ND	0.0	742.75
937.72	NZ	1,710.36	ND	0.9	0.4	0.0	0.0	0.2	0.0	1,290.19
944.05	NZ	5,722.62	ND	5.0	0.5	0.0	0.0	0.0	0.0	1,043.38
947.22	NZ	10,634.51	ND	6.8	0.5	0.0	0.0	0.0	0.0	1,456.07

HS = headspace sample, NZ = additional sample taken for onshore analysis (see "Geochemistry"). ND = not detectable.

Table T8. Concentration of carbon and nitrogen, Site U1379. (Continued on next three pages.)

Core, section	Depth (mbsf) Top	Bottom	Average	TC (wt%)	TN (wt%)	TIC (wt%)	TOC (wt%)
334-U1379B-							
2H-1	1.95	1.97	1.96	2.33	0.07	—	—
2H-2	2.70	2.72	2.71	—	—	—	—
2H-2	2.70	2.72	2.71	0.98	0.84	—	—
2H-2	3.45	3.47	3.46	2.59	0.09	—	—
2H-3	4.20	4.22	4.21	—	—	—	—
2H-3	4.20	4.22	4.21	1.37	0.81	0.67	0.70
2H-3	4.95	4.97	4.96	—	—	0.62	—
2H-4	5.70	5.72	5.71	—	—	—	—
2H-4	5.70	5.72	5.71	1.25	0.76	—	1.25
2H-4	6.45	6.47	6.46	—	—	—	—
2H-4	6.45	6.47	6.46	1.21	0.88	—	—
2H-5	7.20	7.22	7.21	2.43	0.11	0.46	1.97
2H-5	7.35	7.37	7.36	—	—	—	—
2H-5	7.35	7.37	7.36	1.45	0.06	0.63	0.82
2H-5	7.73	7.75	7.74	2.69	0.10	—	—
334-U1379C-							
1H-1	1.40	1.42	1.41	1.69	0.04	1.06	0.63
1H-2	2.90	2.92	2.91	—	—	—	—
1H-2	2.90	2.92	2.91	1.28	0.84	0.58	0.70
1H-3	4.40	4.42	4.41	1.30	0.05	—	—
1H-3	4.40	4.42	4.41	1.38	0.68	—	—
1H-4	5.90	5.92	5.91	—	—	—	—
1H-4	5.90	5.92	5.91	1.29	0.81	0.53	0.76
1H-5	6.50	6.52	6.51	1.32	0.06	0.59	0.73
1H-5	6.50	6.52	6.51	1.35	0.82	—	—
2H-1	8.10	8.12	8.11	—	—	—	—
2H-1	8.10	8.12	8.11	1.29	0.96	0.63	0.66
2H-2	9.60	9.62	9.61	1.68	0.87	1.14	0.54
2H-2	9.60	9.62	9.61	1.62	0.05	—	—
2H-3	11.10	11.12	11.11	—	—	—	—
2H-3	11.10	11.12	11.11	1.38	0.95	0.55	0.83
2H-4	12.60	12.62	12.61	—	—	—	—
2H-4	12.60	12.62	12.61	1.27	0.73	0.63	0.64
2H-5	14.10	14.12	14.11	—	—	—	—
2H-5	14.10	14.12	14.11	1.49	0.09	0.75	0.74
2H-6	14.56	14.58	14.57	1.63	0.06	1.06	0.57
2H-6	14.56	14.58	14.57	1.66	0.80	—	—
3H-1	17.58	17.60	17.59	2.90	0.12	1.01	1.89
3H-2	19.08	19.10	19.09	2.62	0.10	—	—
3H-3	20.58	20.60	20.59	3.19	0.18	1.35	1.84
3H-4	22.08	22.10	22.09	2.15	0.08	1.29	0.86
3H-4	22.08	22.10	22.09	2.16	1.11	—	—
3H-5	23.58	23.60	23.59	1.46	0.06	0.67	0.79
3H-5	23.58	23.60	23.59	1.43	0.84	—	—
3H-6	24.09	24.11	24.10	2.66	0.13	0.82	1.84
4H-2	27.08	27.10	27.09	3.06	0.10	1.31	1.75
4H-4	29.62	29.64	29.63	2.64	0.11	0.84	1.80
5H-2	33.08	33.10	33.09	2.74	0.11	0.94	1.80
5H-4	36.19	36.21	36.20	1.65	0.07	0.71	0.94
5H-4	36.19	36.21	36.20	1.47	0.84	—	—
6H-2	39.38	39.40	39.39	2.82	0.14	0.90	1.92
6H-4	42.38	42.40	42.39	—	—	—	—
6H-4	42.38	42.40	42.39	1.62	0.83	0.77	0.85
7H-2	45.38	45.40	45.39	2.80	0.12	0.85	1.95
7H-4	48.36	48.38	48.37	2.95	0.14	0.90	2.05
8H-2	51.98	52.00	51.99	3.28	0.13	1.06	2.22
8H-4	54.90	54.92	54.91	1.69	0.08	0.80	0.89
8H-4	54.90	54.92	54.91	3.14	0.14	0.80	2.34
9H-1	56.49	56.51	56.50	3.03	0.13	—	—
9H-2	58.38	58.40	58.39	3.39	0.15	1.02	2.37
9H-3	59.49	59.51	59.50	—	—	—	—
9H-4	61.28	61.30	61.29	4.55	0.13	—	—
10H-1	62.38	62.40	62.39	7.90	0.09	5.95	1.95
10H-1	62.38	62.40	62.39	6.43	0.07	5.95	0.48
10H-2	62.72	62.74	62.73	—	—	—	—
10H-3	63.26	63.28	63.27	—	—	—	—
10H-3	63.26	63.28	63.27	11.17	0.10	—	—

Table T8 (continued). (Continued on next page.)

Core, section	Depth (mbsf) Top	Bottom	Average	TC (wt%)	TN (wt%)	TIC (wt%)	TOC (wt%)
11H-1	64.88	64.90	64.89	—	—	—	—
11H-1	64.88	64.90	64.89	1.36	0.94	13.88	—
11H-2	65.99	66.01	66.00	—	—	—	—
11H-2	65.99	66.01	66.00	—	—	—	—
11H-2	65.99	66.01	66.00	1.32	0.72	—	—
11H-3	67.28	67.30	67.29	2.97	0.12	0.52	2.45
12H-1	68.49	68.51	68.50	8.99	0.04	—	—
12H-2	70.58	70.60	70.59	2.53	0.11	—	—
12H-3	71.49	71.51	71.50	—	—	—	—
12H-3	71.49	71.51	71.50	1.55	0.08	—	—
12H-4	73.23	73.25	73.24	1.55	0.06	0.51	1.04
12H-4	73.23	73.25	73.24	1.85	0.88	0.51	1.34
13H-1	74.85	74.87	74.86	—	—	—	—
13H-1	74.85	74.87	74.86	1.48	0.89	—	—
13H-2	76.58	76.60	76.59	2.28	0.20	0	2.28
14H-3	82.79	82.81	82.80	1.44	0.07	—	—
15H-1	84.14	84.15	84.145	—	—	—	—
15H-3	86.15	86.17	86.16	1.60	0.07	0.77	0.83
16H-1	87.69	87.71	87.70	1.28	0.91	—	—
16H-2	89.38	89.40	89.39	1.28	0.04	0.83	0.45
16H-3	89.95	89.97	89.96	1.48	0.04	—	—
16H-3	89.95	89.97	89.96	1.53	0.86	—	—
17H-1	90.96	90.98	90.97	1.52	0.04	0.81	0.71
20X-1	112.07	112.09	112.08	1.28	0.09	0.56	0.72
20X-3	115.07	115.09	115.08	0.94	0.06	0.58	0.36
21X-3	124.83	124.85	124.84	1.58	0.09	—	—
22X-6	138.03	138.05	138.04	1.49	0.10	0.33	1.16
23X-1	141.48	141.50	141.49	2.76	0.13	1.48	1.28
24X-3	154.23	154.25	154.24	—	—	—	—
24X-3	154.23	154.25	154.24	1.87	0.10	0.92	0.95
25X-3	164.03	164.05	164.04	6.02	0.09	4.72	1.30
25X-5	166.98	167.00	166.99	2.10	0.10	1.04	1.06
26X-2	171.47	171.49	171.48	—	—	0.89	—
26X-4	174.45	174.47	174.46	1.81	0.09	—	—
26X-5	175.95	175.97	175.96	2.82	0.13	—	—
26X-6	178.13	178.15	178.14	1.95	0.12	1.18	0.77
27X-1	180.29	180.31	180.30	—	—	1.1	—
27X-5	186.29	186.31	186.30	—	—	—	—
27X-5	186.29	186.31	186.30	2.00	0.98	—	—
27X-6	187.93	187.95	187.94	2.05	0.11	1.38	0.67
28X-3	192.32	192.34	192.33	3.04	0.16	1.05	1.99
28X-5	195.30	195.32	195.31	1.95	0.09	—	—
28X-6	196.74	196.76	196.75	2.89	0.13	1.00	1.89
29X-1	200.23	200.25	200.24	—	—	0.94	—
29X-2	201.50	201.52	201.51	—	—	0.99	—
29X-4	204.54	204.56	204.55	1.85	0.10	1.21	0.64
29X-5	205.81	205.83	205.82	—	—	—	—
30X-1	209.49	209.51	209.50	—	—	0.53	—
30X-2	211.53	211.55	211.54	—	—	0.77	—
30X-4	213.99	214.01	214.00	—	—	—	—
30X-4	213.99	214.01	214.00	1.74	0.83	—	—
31X-1	217.19	217.21	217.20	2.96	0.13	—	—
30X-7	217.89	217.91	217.90	2.20	0.13	—	—
31X-2	219.33	219.35	219.34	1.90	0.14	1.01	0.89
31X-3	220.20	220.22	220.21	2.96	0.13	—	—
31X-4	221.70	221.72	221.71	—	—	—	—
31X-4	221.70	221.72	221.71	2.30	0.10	—	—
31X-5	223.83	223.85	223.84	1.80	0.10	1.02	0.78
31X-6	224.70	224.72	224.71	2.61	0.11	—	—
32X-3	230.08	230.10	230.09	2.13	0.09	—	—
32X-4	231.58	231.60	231.59	1.91	0.09	—	—
32X-5	233.08	233.10	233.09	—	—	1.48	—
32X-6	235.13	235.15	235.14	2.38	0.11	1.51	0.87
33X-1	236.89	236.91	236.90	—	—	1.58	—
33X-2	238.39	238.41	238.40	—	—	—	—
33X-3	239.89	239.91	239.90	1.82	0.10	—	—
33X-5	243.32	243.34	243.33	1.64	0.16	0.77	0.87
33X-6	244.50	244.52	244.51	2.77	0.15	—	—
34X-1	246.69	246.71	246.70	1.88	0.10	—	—

Table T8 (continued). (Continued on next page.)

Core, section	Depth (mbsf) Top	Bottom	Average	TC (wt%)	TN (wt%)	TIC (wt%)	TOC (wt%)
34X-3	250.18	250.20	250.19	1.84	0.18	1.07	0.77
35X-5	262.48	262.50	262.49	1.71	0.10	0.65	1.06
36X-5	271.74	271.76	271.75	2.28	0.12	2.08	0.20
37X-5	282.58	282.60	282.59	2.11	0.25	0.54	1.57
38X-5	292.38	292.40	292.39	2.40	0.18	1.15	1.25
39X-3	299.19	299.21	299.20	1.62	0.11	0.72	0.90
40X-4	310.20	310.22	310.21	1.77	0.17	0.54	1.23
41X-4	320.28	320.30	320.29	2.29	0.18	1.07	1.22
42X-3	328.43	328.45	328.44	—	—	0.15	—
43X-1	334.29	334.31	334.30	—	—	—	—
43X-1	334.29	334.31	334.30	1.74	0.18	—	1.74
43X-2	335.79	335.81	335.80	1.93	0.13	—	1.93
43X-3	337.29	337.31	337.30	—	—	0.44	—
43X-4	338.79	338.81	338.80	—	—	—	—
43X-4	338.79	338.81	338.80	2.10	0.16	—	—
43X-6	341.41	341.43	341.42	0.92	0.23	0.24	0.68
43X-7	342.26	342.28	342.27	—	—	—	—
43X-7	342.26	342.28	342.27	0.69	0.13	—	—
44X-4	348.33	348.35	348.34	2.14	0.15	—	—
44X-6	350.88	350.90	350.89	1.95	0.26	1.12	0.83
45X-2	354.92	354.94	354.93	1.23	0.08	—	—
46X-3	365.31	365.33	365.32	—	—	0.28	
46X-5	368.45	368.47	368.46	1.15	0.20	0.44	0.71
46X-6	369.31	369.33	369.32	—	—	—	—
46X-6	369.31	369.33	369.32	1.76	0.15	—	—
47X-2	372.84	372.86	372.85	1.47	0.15	—	—
47X-5	378.03	378.05	378.04	1.88	0.15	0.86	1.02
48X-6	386.36	386.38	386.37	1.65	0.12	0.39	1.26
49X-6	395.85	395.87	395.86	1.73	0.10	0.81	0.92
50X-5	405.14	405.16	405.15	2.69	0.19	1.16	1.53
51X-4	412.54	412.56	412.55	1.83	0.11	0.63	1.20
52X-2	420.08	420.10	420.09	2.37	0.14	1.06	1.31
53X-3	430.38	430.40	430.39	3.17	0.23	1.49	1.68
54X-4	439.62	439.64	439.63	2.40	0.26	0.91	1.49
55X-3	448.07	448.09	448.08	2.06	0.11	1.07	0.99
56X-2	456.12	456.14	456.13	3.39	0.20	—	—
56X-4	458.70	458.72	458.71	2.01	0.13	0.93	1.08
57X-1	464.10	464.12	464.11	—	—	—	—
57X-5	470.10	470.12	470.11	—	—	0.60	—
57X-6	471.60	471.62	471.61	—	—	1.02	—
58X-1	473.05	473.07	473.06	—	—	—	—
58X-1	473.05	473.07	473.06	—	—	—	—
58X-2	474.55	474.57	474.56	—	—	—	—
58X-2	474.55	474.57	474.56	2.54	0.09	—	—
58X-3	476.05	476.07	476.06	—	—	—	—
58X-4	477.50	477.52	477.51	—	—	1.55	—
58X-5	478.64	478.66	478.65	2.04	0.08	—	—
58X-6	480.14	480.16	480.15	1.45	0.08	—	—
59X-1	481.68	481.70	481.69	2.72	0.08	—	—
59X-3	484.68	484.70	484.69	—	—	—	—
59X-3	484.68	484.70	484.69	2.02	0.20	—	—
59X-4	486.66	486.68	486.67	—	—	1.58	—
60X-4	496.38	496.40	496.39	1.49	0.12	0.37	1.12
61X-5	507.58	507.60	507.59	1.90	0.15	0.69	1.21
62X-4	514.48	514.50	514.49	0.97	0.06	0.44	0.53
63X-5	524.88	524.90	524.89	1.75	0.08	1.00	0.75
64X-5	534.35	534.37	534.36	1.89	0.09	1.13	0.76
65X-6	545.08	545.10	545.09	1.67	0.08	0.87	0.80
66X-6	554.16	554.18	554.17	—	—	—	—
66X-6	554.16	554.18	554.17	1.90	0.10	1.02	0.88
67X-6	563.80	563.82	563.81	2.11	0.09	1.11	1.00
68X-4	570.38	570.40	570.39	2.22	0.10	1.16	1.06
69X-3	578.33	578.35	578.34	—	—	0.36	—
70X-4	589.72	589.74	589.73	—	—	0.30	—
70X-4	589.72	589.74	589.73	0.46	0.09	0.25	0.21
71X-4	598.54	598.56	598.55	2.34	0.17	1.09	1.25
72X-2	605.28	605.30	605.29	—	—	—	—
72X-2	605.28	605.30	605.29	1.75	0.11	0.90	0.85
73X-5	619.56	619.58	619.57	1.99	0.11	0.88	1.11

Table T8 (continued).

Core, section	Depth (mbsf) Top	Bottom	Average	TC (wt%)	TN (wt%)	TIC (wt%)	TOC (wt%)
74X-4	626.34	626.36	626.35	1.80	0.10	0.80	1.00
75X-4	636.37	636.39	636.38	1.91	0.11	0.83	1.08
76X-3	645.21	645.23	645.22	—	—	0.98	—
77X-2	648.48	648.50	648.49	1.62	0.09	0.70	0.92
78X-4	656.6	656.62	656.61	1.93	0.11	0.92	1.01
79X-4	664.98	665.00	664.99	2.10	0.11	1.17	0.93
80X-4	674.74	674.76	674.75	2.02	0.10	1.16	0.86
81X-2	682.00	682.02	682.01	—	—	1.51	—
82X-3	692.60	692.62	692.61	2.09	0.12	0.88	1.21
83X-1	699.80	699.82	699.81	—	—	—	—
84X-3	712.41	712.43	712.42	—	—	0.40	—
85X-1	717.17	717.19	717.18	1.67	0.10	6.72	—
86X-2	728.47	728.49	728.48	—	—	—	—
89X-2	751.63	751.65	751.64	0.87	0.06	0.25	0.62
91X-4	770.31	770.33	770.32	0.97	0.07	—	—
92X-3	778.90	778.92	778.91	7.49	0.04	6.81	0.68
93X-1	785.22	785.24	785.23	1.19	0.07	0.19	1.00
94X-1	795.06	795.08	795.07	0.69	0.07	0.15	0.54
95X-3	807.48	807.50	807.49	0.65	0.06	0.06	0.59
97X-2	824.78	824.80	824.79	—	—	0.24	—
97X-2	824.78	824.80	824.79	1.14	0.10	0.15	0.99
98X-4	837.26	837.28	837.27	—	—	0.67	—
98X-4	837.26	837.28	837.27	0.49	0.04	0.38	0.11
99X-2	844.18	844.20	844.19	—	—	0.31	—
99X-2	844.18	844.20	844.19	0.50	0.05	0.20	0.30
100X-2	852.66	852.68	852.67	0.91	0.07	0.28	0.63
101X-4	865.28	865.30	865.29	0.84	0.07	0.29	0.55
102X-5	877.40	877.42	877.41	1.06	0.07	0.36	0.70
103X-2	881.24	881.26	881.25	2.32	0.05	1.53	0.79

TN = total nitrogen, TC = total carbon, TIC = total inorganic carbon, TOC = total organic carbon. — = not measured.

Table T9. Summary of APCT-3 temperature measurements, Hole U1379C.

Core	Depth (mbsf)	BWT (°C)	Start fit (s)	End fit (s)	Time measurement (min)	Equilibrium temperature (°C)	Remark
334-U1379C-							
4H	30.2	23.2	24,698	25,331	10.55	15.8	Good
7H	49.1	22.5	33,220	33,799	9.65	16.6	Good
10H	63.5	23.0	—	—	—	—	Poor
12H	73.7	22.0	3,913	4,613	11.67	17.4	Good
13H	78.7	22.8	5,292	5,961	11.15	17.6	Good
16H	90.2	22.3	9,491	10,231	12.33	18.5	Good

APCT-3 = advanced piston corer temperature tool, BWT = bottom water temperature. — = not measured.